The Energetics and Vortex Structure of Seamounts in Stratified, Rotating Flow

Brad Perfect

A dissertation
submitted in partial fulfillment of the
requirements for the degree of

Doctor of Philosophy

University of Washington

2019

Reading Committee:

James Riley, Chair

Nirnimesh Kumar, Chair

Alberto Aliseda

Program Authorized to Offer Degree:
Mechanical Engineering

University of Washington

Abstract

The Energetics and Vortex
Structure of Seamounts in Stratified,
Rotating Flow

Brad Perfect

Co-Chairs of the Supervisory Committee:
James Riley
Mechanical Engineering

Nirnimesh Kumar
Civil and Environmental Engineering

This dissertation is an analytical and numerical investigation into the longstanding hypothesis that seamounts are the "stirring rods" of the ocean. Specifically, it has been proposed that the eddy motions generated by the interaction of underwater mountains with ocean currents might play a significant role in the broader field of ocean mixing. The energy associated with vertical mixing in the ocean is of critical importance for climate models. The effect of seamounts, however, must be parameterized in climate models due to finite computational resources. There remain open questions about the magnitude and mechanisms of seamount-induced mixing, which are not currently accounted for in climate models. To address this, as well as other questions, a series of numerical simulations of an idealized seamount interacting with a uniform flow are carried out. The effects of density stratification and the Coriolis force are included in the simulations, and a range of values are considered. This set of simulations spans a broad range of Froude and Rossby numbers that might be encountered in the ocean, and forms the basis for the analysis conducted in this dissertation.

The first component to this thesis is tied to the fluid mechanical aspects of the simulations. The problem of rotating, stratified flow past a 3D obstacle is of fundamental interest; the

wake structure had never previously been rigorously investigated for this type of flow. A Von Kármán vortex street is known to be produced, but the 3D structure of the vortices, as well as vertical variations in the Strouhal number, the nondimensional eddy shedding frequency, were unknown. The simulations show that the 3D structure of the vortices is controlled by the Burger number. For a small Burger number, eddies are shed as a vertically-uniform column, with a width defined by the baroclinic deformation radius. The shedding frequency is also vertically-uniform, which results in vortices that appear to locally violate the 2D prediction for the Strouhal number. At large Burger number, the eddies are vertically decoupled. Eddies are shed in accordance with 2D theory based on the local diameter of the mountain. The eddy size is approximately equal to the local seamount diameter, and the shedding frequency is such that the Strouhal number is vertically uniform.

The energetic aspects the simulations are then addressed in two parts. In the first part, the rates at which energy was converted between various forms are calculated for each simulation. The energy components of interest were the mean flow kinetic energy, the eddy kinetic energy, the turbulent kinetic energy, the potential energy, and the dissipated energy. Terms to represent each conversion process between these components are derived and computed for each simulation. It is found that the conversion of mean energy to eddy kinetic energy is a dominant term, which can be parameterized using the Burger number. In the second part, the internal waves generated by the seamount are considered. It is shown that the lee waves are much less energetically significant than the unsteady wake for the simulations that are considered. It is shown that pre-existing topographic wave theory is inadequate to model the internal wave energy flux calculated from the simulations. Therefore, existing theories are extended into the strongly-stratified, strongly-rotating, 3D flow regime. The revised internal wave flux model is able to reproduce the structure and energy flux of the internal waves produced in the simulations.

TABLE OF CONTENTS

LIST OF FIGURES

LIST OF TABLES

GLOSSARY

Symbol	Description
a	Standard deviation of a Gaussian
b	Buoyancy field
B	Ensemble-averaged buoyancy
C_D	Drag coefficient
D	Seamount full-width at half maximum
f	Spatially-uniform Coriolis Parameter
F	Internal wave flux
g	Uniform gravitational acceleration
h	Variable bathymetric height
h_c	Seamount cap height
H	Peak seamount elevation above the ocean floor
i	Imaginary unit
k	Specific turbulent kinetic energy (tke), streamwise wavenumber
K_p	Diapycnal diffusivity
l	Cross-stream length scale, cross-stream wavenumber
L	Total ocean depth
m	Vertical wavenumber
N	Buoyancy frequency (also known as the Brunt-Väisälä frequency)
R_D	First baroclinic Rossby radius of deformation
R_{ij}	Reynolds stress tensor
s_{ij}	Rate-of-strain tensor

t	Time variable
T_{ij}	Eddy component of the Reynolds stress
T	Period of vortex shedding
U	Uniform inflow velocity
U_i	Ensemble-averaged velocity
$\bar{U}_i$	Time-averaged velocity
$\hat{u}_i$	Unsteady eddy velocity
$\bar{u}$	Depth-averaged velocity
u_i'	Turbulent velocity
u	Perturbation x-velocity
v	Perturbation y-velocity
w	Perturbation z-velocity
x	Streamwise coordinate, measured from the domain inlet
y	Cross-stream coordinate, measured from the southern edge of the domain
z	Vertical coordinate, measured from the neutral ocean surface
δ_{ij}	Kronecker Delta
ϵ_{ijk}	Levi-Civita symbol
η	Isopycnal displacement
λ	Nondimensional parameter defined by Ro/Bu
ρ	Fluid density
ρ_0	Boussinesq, or spatially-averaged density
ρ_s	Background vertically-varying density
$\bar{\rho}$	Time-averaged density perturbation
$\hat{\rho}$	Time-dependent density perturbation
ν	Molecular kinematic viscosity
ν_N	Numerical fluid viscosity

τ	Nudging time constant
ϕ	pressure, divided by density, also latitude on the Earth
Φ	Ensemble averaged pressure, divided by density
ψ	Generic field variable for defining boundary conditions
ξ	Vertical vorticity
$\vec{\Omega}$	Earth's rotation vector
ζ	Free surface elevation
$\mathcal{A}$	A surface area through which wave radiation passes
$\mathcal{F}$	Fourier transform
$\mathcal{V}$	Volume of the analysis domain
∇^2	Laplacian operator

ACKNOWLEDGMENTS

My committee has been incredibly supportive, and always willing to talk through technical questions. I would like to specifically acknowledge my co-advisers, Jim Riley and Nirni Kumar. Jim has been a constant source of technical expertise and guidance, but he always made certain that I had complete ownership of the decisions and trajectory of this project. When Nirni came on as first a committee member, and later a co-adviser, he gave me the kick in the rear that I needed to begin wrapping up my analysis and to start publishing. His boundless enthusiasm and energy is infectious. In addition, he has been my much-needed guide though the often opaque world of academia.

I have greatly enjoyed interacting with the tightly-knit Computational Fluids group in my time at UW. Despite our fiercely independent projects, virtually every idea in this dissertation is in some way related to one of our many technical discussions. So, thank you to Brandon Blakeley, Arshiya Chime, Kurt Sansom, Mike Barbour, and Laurel Marsh. In addition, I would like to thank the Environmental Fluid Mechanics group for welcoming in this mechanical engineering interloper.

My labmate, Brandon Blakeley, has been in every facet of my life for the last four years. Whether making coffee in the lab, co-teaching classes, roping up on a glacier, making beer, or enjoying said beer after a long week, he has been a go-to companion and a defining part of my graduate school experience.

There have been many teams, clubs, groups, and climbing partners in my life that have kept me sane outside of the office for these last 6 years. So thank you to

Prof. Brian Polagye for tricking me into going mountaineering; to Trevor Harrison for entertaining my crazy trip ideas; to Jacob Mintz for coming up with crazy trip ideas; and the UW climbing club and ultimate frisbee team for the camaraderie.

Finally, I owe a sincere thank you to Jasmine Isaacson. She has been there through every triumph and setback, offering support through the lows, and celebrating each small victory with me.

From a technical perspective, I was incredibly lucky that my research occurred concurrently with a series of proposals to fund free cluster computing for UW students. This project simply could not have happened without the advanced computational, storage, and networking infrastructure provided by the Hyak supercomputer system and funded by the STF at the University of Washington.

DEDICATION

To my parents, Scott and Julie. Words cannot express my gratitude for everything you've done for me.

Chapter 1
INTRODUCTION AND BACKGROUND

This dissertation numerically investigates fluid flow past a 3D obstacle, for a density-stratified fluid and in a rotating reference frame. These flow conditions are descriptive of ocean flow past an underwater mountain, but also have applications for fundamental fluid mechanics. The structure of this dissertation is as follows. The remainder of this chapter is dedicated to establishing the background and motivation for this project. Chapter 2 describes the development, testing, and use the numerical simulations upon which the remainder of this dissertation is based. Chapters 3-5 separately address three important characteristics of the simulation output: vortex structures in the lee of the obstacle (Chapter 3), the underlying physical mechanisms that extract energy from the background flow (Chapter 4), and the internal gravity waves that the obstacle generates (Chapter 5). Finally, the work is summarized and potential directions for future research are outlined in Chapter 6. Overall, this work develops a detailed understanding of the physical interactions between a mountain and a uniform flow.

1.1 Project Motivation

The climate models that form the basis for forecasting and climate change predictions attempt to address the grand challenge of unifying physical processes with length scales ranging from molecular interactions to the size of the earth (Smyth and Moum, 2008). Even with the advent of rapidly increasing computational power, this challenge will remain intractable for decades. Therefore, processes that occur on length scales smaller than the grid resolution of numerical simulations- of which the state of the art is about 50 kilometers for a global circulation model- must be approximated by model equations rather than explicitly simu-

lated (Chen et al., 2013; Delworth et al., 2016). Many features in the bathymetry, including seamounts, cannot be resolved at that scale. The credibility of a climate model then depends on the ability of the model equations for the small scales to accurately represent the physical processes that occur (Legg et al., 2009; Schiermeier, 2007). While many processes are well-modeled, others are modeled with poor fidelity, or not considered at all. In particular, the physical mechanisms governing ocean mixing at a subgrid scale remain an area of active research. It has been shown that seamounts (underwater mountains) can produce patches of increased mixing (e.g., Toole et al., 1997; Naveira Garabato et al., 2011; Kunze et al., 2012), although the observational nature of these studies leaves many gaps in our understanding of the underlying physics of this phenomenon. This project aims to provide a more comprehensive understanding of how seamounts interact with ocean currents and produce waves, coherent eddy structures, and mixing. Such information could be used to suggest mixing parameterizations for global models that use information about the local bathymetry.

In fluid mechanics, there is a canonical problem pertaining to uniform 2D flow past a circular cylinder (Fage, 1936; Achenbach, 1972). While the hydrodynamic wake of a 2D cylinder has been thoroughly studied, research continues through a variety of extensions to this scenario. For example, the 3D effects of a tilted cylinder in stratified flow have been found to produce novel fluid instabilities (Meunier, 2012). Fundamentally, the problem of flow past a seamount is an extension to flow past a cylinder. The present setup adds the effects of density stratification, a rotating reference frame, and a 3D obstacle. Very few studies have explored this problem, and many open questions remain about the wake structure and turbulence properties.

Motivated by open questions in the ocean mixing community and in the fundamental study of fluid flow past obstacles, we address the following questions pertaining to rotating, stratified flow past an idealized seamount:

1. What form does the wake take? What determines the vortex shedding frequency, and is it vertically-uniform?

2. How much energy does the wake extract from the mean flow? Where does that energy ultimately end up, and what pathways does it take? How can the mixing from the wake be parameterized?

3. How much energy goes into the generation of internal gravity waves? How does it compare to the wake energy, and can the wave energy be predicted from theory?

Ultimately, in answering these questions, we move towards a more comprehensive understanding of the fluid mechanics that govern seamount-current interactions. A direct application of this new understanding is in improving estimates of topographic mixing to be used in global circulation models. Additionally, we touch on interesting areas of fluid mechanics that are actively being researched, such as the properties of rotating, stratified turbulence, and internal wave theory.

1.2 Ocean Mixing

The Earth's oceans can be broadly characterized as an incompressible, density-stratified fluid under the influence of the Coriolis acceleration, which stems from the non-inertial reference frame of the Earth's surface. Density variations are generally produced by differences in temperature and salinity, with colder and/or saltier water corresponding to a higher density. While the density differences are relatively slight (e.g., three parts per thousand is a typical open ocean variation), the tremendous mass of ocean water means that the potential energy associated with density variations is a primary driver in ocean dynamics. In particular, the irreversible mixing produced when ocean water of varying density is allowed to mix on a molecular level is of great importance to oceanographers.

The field of ocean mixing stems from Munk (1966) who, while studying upwelling in the ocean, inferred that a tremendous amount of diapycnal (i.e., across surfaces of constant density) mixing would be required to maintain a steady state ocean from a climatalogical perspective. Open ocean mixing values, however, were found to be approximately an order of magnitude below the theoretical value. Consequently, it was found that the distribution

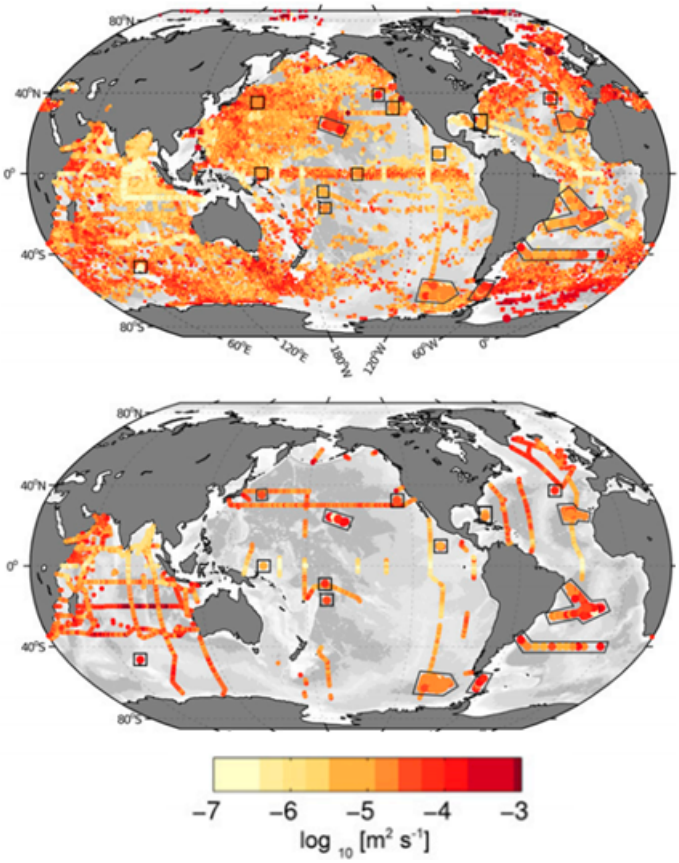

Figure 1.1: Inferred diapycnal diffusivity maps, reproduced from Waterhouse et al. (2014) and Whalen et al. (2012). ©American Meteorological Society. Used with permission.

of mixing in the ocean follows the pareto principle; most of the mixing is caused by localized regions of very intense mixing. In field experiments, mixing values are typically inferred from finescale measurements of the temperature and salinity profiles in a given location (Gregg et al., 2018). Utilizing a fleet of autonomous drifters, Waterhouse et al. (2014) produced a global map of mixing rates, confirming the idea that mixing tended to be highly localized (see Figure 1.1).

A distinction remains between the location of the mixing and its proximate cause. Mixing events may be seasonal and highly localized, so it is important to understand the physical processes that produce them. In many cases, mixing is caused by breaking internal gravity

waves. Internal waves may be generated by many different processes, such as internal tides, interaction with bathymetry, or by baroclinic motions. Furthermore, they may break locally near their point of generation, or propagate for thousands of miles, before eventually breaking on a distant continental slope. Another possible, but often overlooked, source of mixing is the hydrodynamic wakes of seamounts.

1.3 Bathymetry and Seamounts

The primary focus of this dissertation is the impact that seamounts have on diapycnal mixing. Formally, a seamount is defined to be a feature on the sea floor that rises at least 1000m above the surrounding terrain, without breaking the ocean surface. In practice this definition is more opaque, much in the same way as the definition of a terrestrial mountain. Many researchers consider seamounts more contextually (Jordan et al., 1983). A minimum height for a seamount can better be thought of as a height that may be capable of producing internal waves or a hydrodynamic wake, which can change with the local current and stratification profile. Abyssal hills with a typical height scale of 100m may produce significant internal wave flux, and the largest seamounts can exceed 4000m in relief. Poor ocean floor mapping for many years led to a severe underestimate for the prevalence of large seamounts. Whereas some older sources indicated as few as 10,000 seamounts in excess of 1km in height, Wessel et al. (2010) predicts over 100,000 such seamounts using statistical methods. By the same methods, there are speculatively 25 million seamounts with heights of at least 100m. The relatively recent revisions to seamount population estimates are cause to reconsider the combined effect of seamounts on ocean mixing.

There is no standard shape for a seamount, though many large seamounts may resemble Gaussians or long ridges. Many exhibit significant subpeaks and roughness that produce complex flow patterns and sustain diverse ecological communities (Rogers, 1994; Carter et al., 2006). The smallest seamounts may be indistinguishable from the typical bottom roughness in other areas of the ocean. In light of the vast population of seamounts, the interaction of ocean currents with seamounts may have implications for the energetics of the entire

ocean. This hypothesis is further encouraged by observational evidence of intense mixing in the vicinity of large seamounts (Brink, 1990). The local diapycnal diffusivities around seamounts have been observed to be orders of magnitude higher than the basin averages, indicating strong turbulence and mixing, but the mechanisms that produce it are not all well understood (Carter et al., 2006; Kunze, 2003).

1.3.1 Seamounts as Stirring Rods and Wave Generators

In previous ocean mixing literature, seamounts have been primarily treated as sources of internal gravity waves (e.g. Legg et al., 2009). In this scenario, ocean flow that is incident upon the seamount is forced up and over, which generates a propagating perturbation in the density field. These internal gravity waves may break locally and produce mixing, or propagate for vast distances and later break on the continental shelf (Alford et al., 2015; Grisouard and Staquet, 2010; Kunze, 2003; Lamb, 2014). The ability of seamounts to extract energy from the barotropic flow and produce internal waves has been rigorously demonstrated in a variety of scenarios (Nikurashin and Ferrari, 2009; Klymak et al., 2010). The global topography-induced internal wave flux is estimated to be in the range of 200-750 GW, which is of a similar order of magnitude as the input of wind energy into the ocean (Nikurashin and Ferrari, 2011; Wright et al., 2014). Of particular interest for this work is the internal lee wave flux. Lee waves, which are locked to the bathymetry, continuously radiate energy upwards through the water column and are thought to play a significant role in deep ocean mixing (Nikurashin and Ferrari, 2013).

A concurrent, but often overlooked phenomenon is the hydrodynamic wakes of seamounts. The flow that is directed around the seamount can produce eddies and turbulence, which later lead to mixing. We refer to mixing due to the seamount wake as the "stirring rod" hypothesis, which was coined by Munk and Wunsch (1998) but has apparently existed for several decades. By their nature, seamount wakes are difficult to study. Whereas linear wave theory (e.g., Bell, 1975) can provide a first order description of topographic waves, the process of vortex shedding is highly nonlinear and resists analytical treatment. Additionally,

the timescales associated with vortex shedding are much longer than those of internal waves, which is of concern in the field. Internal waves evolve on a timescale of approximately the inverse of the buoyancy frequency (minutes to hours), and are readily measured in the open ocean. Topographic vortex shedding occurs over a period of days to weeks, and tends to occur in deeper water. The challenges associated with taking abyssal measurements over such a long time frame discourage field observations. It was only recently that Chen et al. (2015) presented the first direct evidence of a deep water eddy originating from a seamount. Laboratory experiments (e.g. Hunt and Snyder, 1980; Brighton, 1978) have demonstrated vortex shedding under conditions designed to mimic flow past a mountain, but virtually nothing is known about the energetics of these wakes.

A natural question that arises from these two interpretations of seamounts is how they relate to each other. While it is understood that real seamounts undoubtedly exhibit aspects of both wakes and waves, the internal wave interpretation has enjoyed a preeminent position in the ocean mixing community. Topographic parameterizations of mixing, then, reflect this bias towards an internal wave perspective (e.g., Polzin et al., 1997). It is possible that the mixing contribution of internal waves dominates that of wakes, but this conclusion has been implicitly assumed, rather than determined through research. A secondary goal of this work, in addition to understanding the physical process of seamount-generated mixing, is to critically assess the wave-dominant viewpoint by rigorously investigating both the wake and wave aspects of flow past a seamount.

1.3.2 Seamount Parameters

Dynamically, a seamount may be characterized by its shape, as well as its interaction with the geophysical parameters surrounding it. We define a characteristic height and width for a seamount, H and D, respectively. We also consider a characteristic velocity U, buoyancy

frequency[1] N, and Coriolis parameter[2] f. The effects of stratification and rotation can then be expressed in terms of the Froude (Fr) and Rossby (Ro) numbers, respectively:

$$\mathrm{Fr} \equiv \frac{U}{NH} \qquad \mathrm{Ro} \equiv \frac{U}{fD}. \tag{1.1}$$

These nondimensional parameters are a convenient way to describe the strengths of rotation and stratification, relative to a seamount's size. A discussion of additional parameters of interest is reserved for Section 2.1. The choice of these parameters is in part motivated by Canals et al. (2009), who note the need for a systematic study of hydrodynamic wakes in this parameter space. Figure 1.2 provides a brief overview of literature involving flow past mountains, both in the atmosphere and in the oceans, organized by the range of Rossby and Froude numbers that were considered.

In the limiting case of no rotation and no stratification (large Froude and Rossby numbers), the behavior of classical fluid mechanics is recovered. From there, the addition of rotation encourages the fluid to act in a more two-dimensional manner. The flow gains vertical uniformity. For extremely strong rotation, it can be shown that the flow can not have any variation in the vertical dimension, and thus asymptotically becomes 2D. Flow past a mountain in this case forms Taylor columns, which force the flow to move around the mountain's footprint, even above the summit. Adding stratification to a classical flow has an opposite, yet paradoxically similar effect. Stratification tends to limit vertical motion, and discourages interaction between fluid at different vertical levels. In the extreme case, every vertical level evolves independently, as a 2D fluid. Another aspect of stratification is that it controls whether fluid will predominantly flow over or around a seamount. When $\mathrm{Fr} \ll 1$, the flow is confined to horizontal planes and moves around the mountain. As $\mathrm{Fr} \gg 1$, the flow

[1]The buoyancy frequency describes the degree of density stratification in a fluid. This frequency is obtained by solving the equations of motion for a parcel of fluid that is displaced in the vertical. A more strongly stratified fluid has a higher buoyancy frequency. Typical oceanic values can range from 10^{-4} to $10^{-2}\mathrm{s}^{-1}$

[2]The Coriolis parameter is defined to be $f \equiv 2\Omega \sin\phi$, where $\Omega \equiv 7.2921 \times 10^{-5}\mathrm{rad\ s}^{-1}$ is the Earth's angular velocity and ϕ is the latitude. This parameter enters the equations of motion at geophysical scale and produces a tendency for a flow to turn towards the right in the Northern Hemisphere

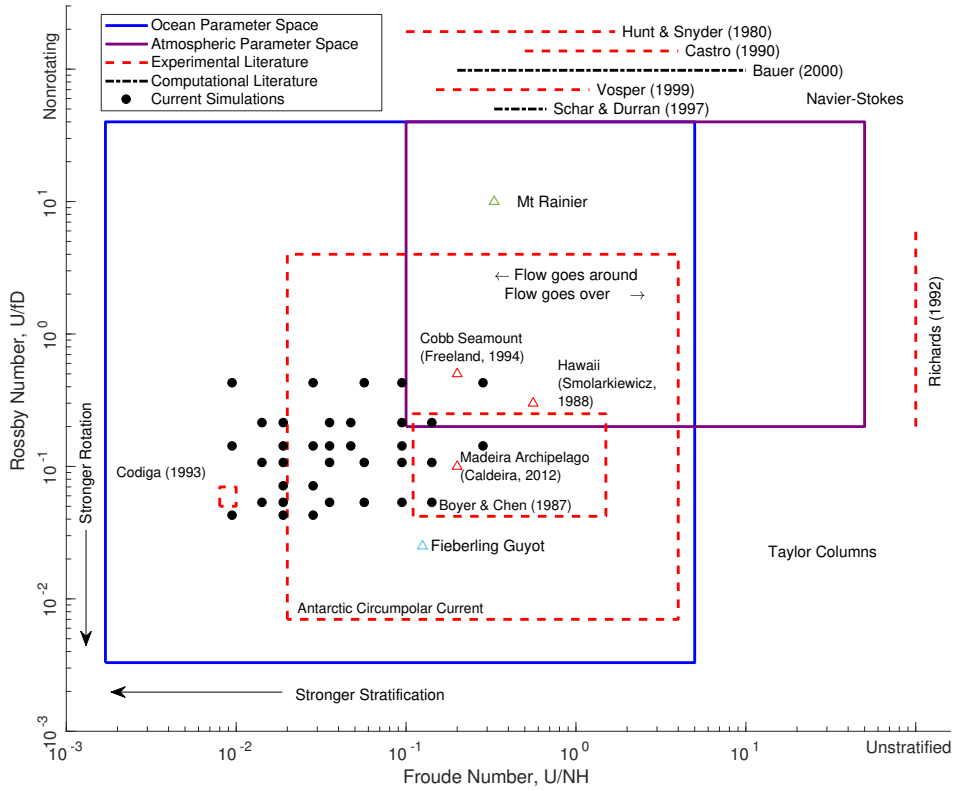

Figure 1.2: The dynamics of flow past a three-dimensional mountain can be plotted in a parameter space defined by the Froude and the Rossby number. The ranges surveyed by several key studies are indicated (Hunt and Snyder, 1980; Castro et al., 1990; Richards et al., 1992; Freeland, 1994; Schär and Durran, 1997; Vosper et al., 1999; Bauer et al., 2000; Caldeira and Sangrà, 2012). Additionally, the parameter spaces that might be observed in the ocean and atmosphere are indicated with blue and purple boxes, respectively. Studies where the mountain dynamics are based on linear theory have not been plotted.

tends to go over an obstacle. This, as will be discussed later in Chapter 5, has substantial implications for the wakes versus waves question introduced in Section 1.3.1.

The parameter space of strong rotation and strong stratification (low Froude and Rossby number) is important for the ocean, but less important in the atmosphere. The length scales of terrestrial mountains tend to produce large (> 1) Rossby and Froude numbers. While the stratification is still very important to the dynamics, atmospheric studies at this scale often neglect the effect of rotation. This can be evidenced by the nonrotating studies at the top

of Figure 1.2. A consequence of the nonrotating approximation for atmospheric studies is that the low Froude and Rossby number regime has been neglected, with very few studies probing this area.

1.3.3 Case Studies of Seamounts

A number of seamounts have been the subject of study through observations and numerical modeling. One such seamount, Fieberling Guyot, serves as an approximate model for the dimensions used in this project. Below, the various relevant studies are organized by the seamount that was studied. These case studies help establish the range of behavior that can be expected from seamount-current interaction, and therefore serve as a starting point for the analysis of an idealized seamount.

Fieberling Guyot

Fieberling Guyot is a large isolated seamount located in the northeastern Pacific ocean, rising 3500m from the sea floor to within 500m of the surface. It was the subject of a detailed set of observations during the Flow over Abrupt Topography initiative in the 1990's (Brink, 1995), and subsequent studies have built upon the impressive dataset that was gathered during the initiative. Numerous scientific studies describe the geology, biology, and fluid dynamics of this mountain, and a large array of sensors have led to a series of detailed data from which many research models have been constructed. Flow patterns around Fieberling have been measured extensively (Roden, 1991; Kunze and Toole, 1997; Toole et al., 1997). Laboratory work that replicated the conditions around Fieberling reproduced trapped wave modes for an oscillating flow (Codiga, 1993). A wide array of numerical models have explored a variety of aspects of the hydrodynamics around Fieberling Guyot, including nutrient residence time in the wake (Coutis and Middleton, 2002), seamount-generated internal tides (Robertson, 2006), and local currents (Beckmann and Haidvogel, 1993, 1997).

Cobb Seamount

Cobb Seamount is a 3000-m seamount rising nearly to the ocean surface. Observations have indicated that local diapycnal diffusivity in the vicinity of the seamount are 1000 times as large as background values, suggesting that local hydrodynamic processes contribute greatly to ocean mixing (Lueck, 1997). Flow around Cobb has been modeled with qualitative success (Freeland, 1994).

Hawaiian Islands

While not technically seamounts, the abrupt ridges that comprise the Hawaiian islands have been a favored location of study, both for oceanic and atmospheric study. The generation mechanism for internal tides at the Hawaiian islands has been successfully modeled (Carter et al., 2008). Models of a small seamount near Hawaii reinforce the notion that in a strongly stratified environment, flow will tend to move around rather than over mountains (Carter et al., 2006).

Maidera Archipelago

In contrast to most of the Fieberling Guyot models, which were created in the 1990's, Maidera has been the subject of more contemporary modeling efforts (e.g., Boutov et al., 2010; Caldeira and Sangrà, 2012). The complex terrain was found to produce a variety of vortex shedding patterns that were modified by the presence of nearby seamounts. Many of the features that have been described numerically for Maidera also appear in the current project. For example, the periodic eddy shedding features prominently in simulations of Maidera, as well as the current project. In the studies of Maidera, different flow patterns were associated with various fluid instabilities.

Flow Past Headlands

Headlands can act like seamount flanks with respect to the generation of vorticity and mixing. Because these features are much more accessible for field studies and figure prominently into nearshore processes, they have been studied in significant detail. Canals et al. (2009) found tilted vortices that are shed from headlands in a combined numerical and observational study. The form drag and associated internal waves and mixing were studied by McCabe et al. (2006). Finally, Callendar et al. (2011) observed vorticity generation associated with the tidal flow past a headland. Together these studies help confirm that flow past a sloped boundary leads to increased diapycnal mixing, and also serve as additional observational confirmation that vortex shedding can figure prominently into the flow effects.

1.4 The Idealized Mountain

While studies of realistic mountains are useful for reproducing or explaining specific phenomena, idealized studies are better suited for probing the underlying mechanisms that are at play in the general case. The studies described in Sec. 1.3.3 demonstrate some of the effects that topography can have and identify signatures of several instabilities. It is not clear, however, which effects are specific to that field site, and which are caused by the more general problem of rotating, stratified flow past topography. Therefore, the objective here is to study an idealized seamount, which eliminates the effects of unique bathymetry and density/current profiles.

For this study, we consider an axisymmetric Gaussian seamount (see Fig. 1.3), whose dimensions were based off of Brink's observations of Fieberling Guyot (Brink, 1995). The seamount rises above a flat bottom and is topographically smooth (though some roughness is modeled in the form of bottom drag). To within a reasonable degree, this setup approximates a large, isolated seamount. However, as noted by Raja (2018), Caldeira and Sangrà (2012), and Zhang et al. (2017), seamounts often occur in chains and influence each other to a significant degree. Additionally, many other seamounts take the form of long ridges that

can begin to behave as 2D obstacles (St. Laurent and Garrett, 2002; Llewellyn Smith and Young, 2003). These cases are explicitly not considered here. Rather, we only consider an axisymmetric, isolated seamount; the ocean is known to contain seamounts of this type, and there are enough unanswered questions that this is a reasonable case to study.

The current profile is chosen to be uniform, and the density profiles is assumed to be linear (i.e., the buoyancy frequency is vertically-uniform). In a realistic ocean, surface effects mean that the current and buoyancy frequency both reach a maximum magnitude near the surface. Effects at depth can vary based on location, but typically both velocity and buoyancy frequency decrease approximately logarithmically. For example, a typical realistic density profile is presented in Figure 1.4. Many of the studies in Section 1.3.3 focus on near-surface processes, where variability in the buoyancy frequency is most important. In the abyss, however, vertical variations become less important. It is also in this region where one finds the largest uncertainties in flow velocity, buoyancy frequency, and diapycnal mixing. The idealized setup then best represents an isolated, axisymmetric seamount located on the abyssal plain. In general, this is a good first step towards understanding the general dyanamics of flow past seamounts.

1.4.1 Previous Idealized Mountain Studies

The idealized mountain described above has been studied in some detail, particularly in the weakly stratified and nonrotating regime (i.e., the top center of Figure 1.2.) In the laboratory, flow past an idealized mountain is recreated by towing a model mountain through a stratified fluid (Hunt and Snyder, 1980). These types of studies are well-suited for measuring drag, as well as visualizing flow patterns (Vosper et al., 1999). In practice, the restrictions of salt solubility, combined with physical requirements such as having a mountain larger than the Ekman layer thickness mean that it is very difficult to conduct laboratory experiments with $\mathrm{Fr} < 0.15$. Near this limit, however, vortex shedding is clearly seen in laboratory studies (Brighton, 1978). These results are in stark contrast to the steady flow patterns predicted by linear analytical treatments (Drazin, 1961; Sheppard, 1956).

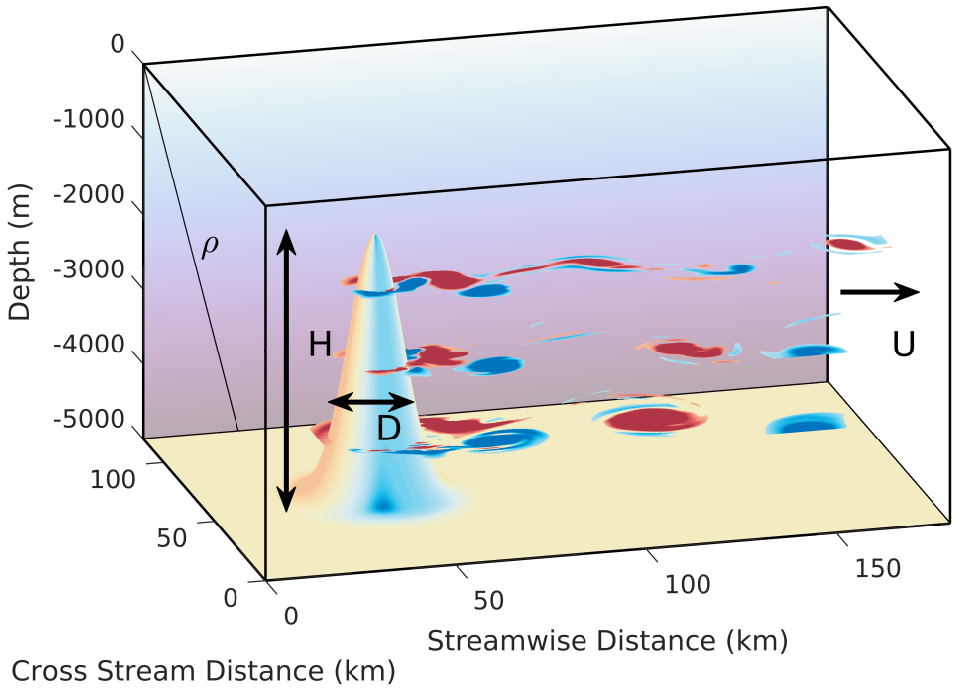

Figure 1.3: Schematic of the idealized seamount. The seamount is assumed to be an axisymmetric Gaussian with characteristic height H and width D. A uniform velocity U and buoyancy frequency N are incident upon the seamount. An f-plane Coriolis parameter f is also present.

Numerically, idealized mountains have been a favored area of study in atmospheric science. Moderate Froude number, nonrotating simulations have focused on the formation of vorticity in mountain wakes (Schär and Smith, 1993a,b; Schär and Durran, 1997; Smolarkiewicz and Rotunno, 1989). Epifanio (2003) investigates the formation of lee vortices in this regime. Bauer et al. (2000) performed a systematic study of flow past an idealized mountain, as a function of the Froude number and the mountain aspect ratio, finding distinct flow regimes.

A common thread of the above studies is that the effect of rotation is neglected. Because fluid motion in the atmosphere is much faster than in the ocean, the Rossby number ($\frac{U}{fD}$) of terrestrial mountains is much larger, indicating that the effect of rotation is much less important for the dynamics. In fact, most atmospheric applications with length scales on

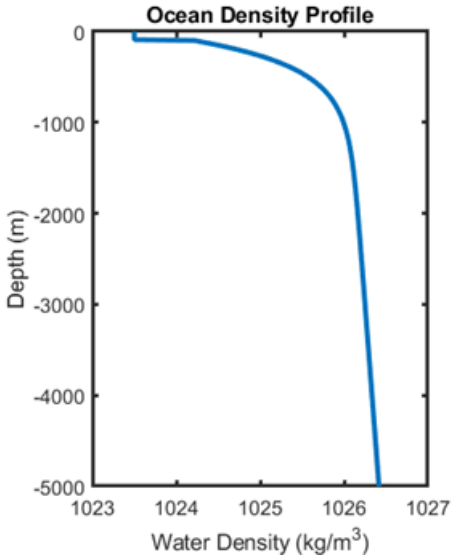

Figure 1.4: A typical vertical density distribution for the ocean.

the order of mountains neglect the effect of rotation entirely. To contrast, large seamounts are associated with both small Froude and Rossby numbers, corresponding to the strongly stratified, strongly rotating regime (bottom left in Figure 1.2. There has been some idealized modeling in this area, but the geometries were restricted to cylindrical obstacles (Dong et al., 2007). Concurrently to this work, Srinivasan et al. (2019) also modeled idealized seamounts, though the focus was on bottom boundary layer processes, rather than mixing. Recent work by Raja (2018) described experimental studies of a seamount in rotating, stratified flow, but the experiments were limited and gave only a cursory treatment of the seamount wakes.

The goal of this work, then, is to extend previous studies of idealized mountains into the strongly rotating and strongly stratified flow regime. This is a parameter space that is prohibitively difficult to study in the laboratory, and impractical to observe in the field. We therefore approach this problem with numerical simulation, which is the subject of the next chapter.

Chapter 2
COMPUTATIONAL MODEL FORMULATION

The analysis in this dissertation is conducted for the results of a series of numerical simulations. This chapter includes a full description of the numerical model, as well as its development and methods used. The specifics, however, are reserved for the end of the chapter. A more general description is provided in Sections 2.1 and 2.2, which is intended to orient the reader without interest in model-specific details for the remainder of this dissertation. The sections that follow contain the details of the model.

2.1 Model Description

The goal of this computational model is to provide the simplest possible representation of a seamount while still capturing the essential dynamics. Previous studies have demonstrated that it is possible to accurately simulate flow in the vicinity of a seamount (e.g. Brink, 1995; Caldeira and Sangrà, 2012; Robertson, 2006), but the complexities of a realistic model tend to obfuscate the underlying physical processes. We then build upon the successes of realistic models and apply several key simplifications in order to study the essences of these processes.

1. The seamount can be described by an axisymmetric Gaussian, rising above a flat bottom. The seamount elevation above the ocean floor, h, is given by,

$$h(x,y) = He^{-\frac{8\ln 2}{D^2}\left(x^2+y^2\right)}, \tag{2.1}$$

   where the seamount has height H and full width at half maximum (FWHM) D. The numerical factor relates the FWHM to the standard deviation. Alternately, for a standard deviation a, the seamount height is given by,

$$h(x,y) = He^{-\frac{x^2+y^2}{a^2}}. \tag{2.2}$$

2. The Boussinesq approximation is invoked. The density $\rho(x, y, z, t)$ may be treated as a spatially-uniform value ρ_0, except in treating the buoyant force.

3. The hydrostatic approximation is invoked. The dynamic pressure due to fluid velocity is assumed to be zero. This assumption greatly reduces the computational complexity.

4. The background density stratification profile is linear, and horizontally uniform. That is, $\rho_s(z)$, the background vertical variation in density, is linear and independent of horizontal position. Therefore, the gradient of the density field is uniform everywhere, and the buoyancy frequency,
$$N \equiv \sqrt{-\frac{g}{\rho_0}\frac{\partial \rho}{\partial z}}, \tag{2.3}$$
is constant.

5. Density stratification is achieved by considering variations in temperature, and a linear equation of state relates the density to the temperature.

6. The Coriolis parameter is modeled using an f-plane approximation. That is, slight variations in the Coriolis parameter due to changes in latitude are ignored. Consequently, the Coriolis parameter is spatially uniform.

7. The turbulence in the simulation is modeled with a Reynolds-Averaged Navier-Stokes (RANS) closure model.

8. The seamount is subjected to a uniform flow, U. This flow is maintained using a geostrophic balance; the ocean surface is tilted in such a way that the large scale effects of the Coriolis acceleration are negated.

These simplifications allow the dynamics in the model to be determined by a relatively small set of parameters:

- N, the spatially uniform buoyancy frequency

- f, the spatially uniform Coriolis parameter
- U, the incident fluid velocity
- H, the seamount height
- D, the seamount FWHM
- L, the water depth.

With use of the Buckingham Π theorem, we may further reduce this parameter set to:

- The Froude number, $\mathrm{Fr} \equiv \frac{U}{NH}$, which measures the strength of stratification relative to the seamount's height.
- The Rossby number, $\mathrm{Ro} \equiv \frac{U}{fD}$, which measures the importance of the Coriolis parameter with respect to the seamount dynamics.
- The depth ratio, $\frac{H}{L}$.
- The seamount aspect ratio, $\frac{H}{D}$.

The Froude and Rossby numbers, as explained in Figure 1.2 are important controlling parameters for the seamount problem. The depth ratio, however, can have a significant impact on the vertical extent of the seamount wake, as shown by Boyer and Chen (1987) and Srinivasan et al. (2019). For the present study, we maintain the depth ratio at a constant value of 0.6, which tends to prevent the formation of Taylor columns and other structures that span the entire water column depth. Vortex structures are then confined to the region downstream of the seamount, and do not rise above the seamount summit. Finally, the seamount aspect ratio is known to impact internal wave dynamics, especially at low Froude number (Balmforth et al., 2002). The mechanisms of wake generation may also be sensitive to the aspect ratio (e.g. Srinivasan et al., 2019). We maintain a constant aspect ratio for this

study, which is based on the aspect ratio of Fieberling Guyot (discussed in Section 1.3.3). Variations in the aspect ratio and depth ratio are worthy of study, but they are beyond the scope of this dissertation. This study explores how variations in the Froude and Rossby numbers impact the mechanics of an idealized seamount.

The Reynolds number ($\mathrm{Re} \equiv \frac{UD}{\nu_N}$) is relevant in the sense that the simulation contains the effect of an explicit viscosity, ν_N. In the manner that the Reynolds number is defined, it impacts the scale of the flow structures that may develop in the simulations. Because ν_N is related to the numerical methods of the simulation, Re has more to do with the simulation accuracy than the dynamical properties of the seamount. The Reynolds number based on the molecular viscosity is very large ($O(10^9)$), and the dynamics of the problem are insensitive to changes in the physical Reynolds number in this range. With respect to the Reynolds number based on the explicit viscosity, Dong et al. (2007) find that above $\mathrm{Re} \approx 1500$, the essential dynamics for flow past an island are accurately captured. For the present study, $\mathrm{Re} \approx 2000$. Assuming that a similar Reynolds number limitation is applicable for the case of a seamount, we are free to discard it as a controlling parameter for the present study.

The idealized seamount is simulated using the Regional Ocean Modeling System (ROMS) framework (Shchepetkin, 2003; Shchepetkin and McWilliams, 2005). ROMS is a community code that is typically used for simulating sections of the ocean with a length scale on the order of 1000-10,000 km, but has also been used for high-resolution simulations in smaller domains (e.g. Boutov et al., 2010; Dong and McWilliams, 2007). ROMS solves the hydrostatic primitive equations over the simulation domain and computes field variables, such as the fluid velocity, density, and turbulent kinetic energy.

The simulation domain (see Figure 2.1) is a rectangular prism, measuring 180 km in the zonal direction, 120 km in the meridional direction, and 5 km in depth. A 3500-m Gaussian seamount, as defined by Equation 2.1, extends from the domain bottom The standard deviation of the Gaussian is 10 km, which corresponds to a FWHM of 23,550 m. The peak is located 45 km from the western boundary[1] (the inlet) and 60 km from the northern and

[1]Domain sides are referred to using the cardinal directions. The domain is assumed to have dynamics

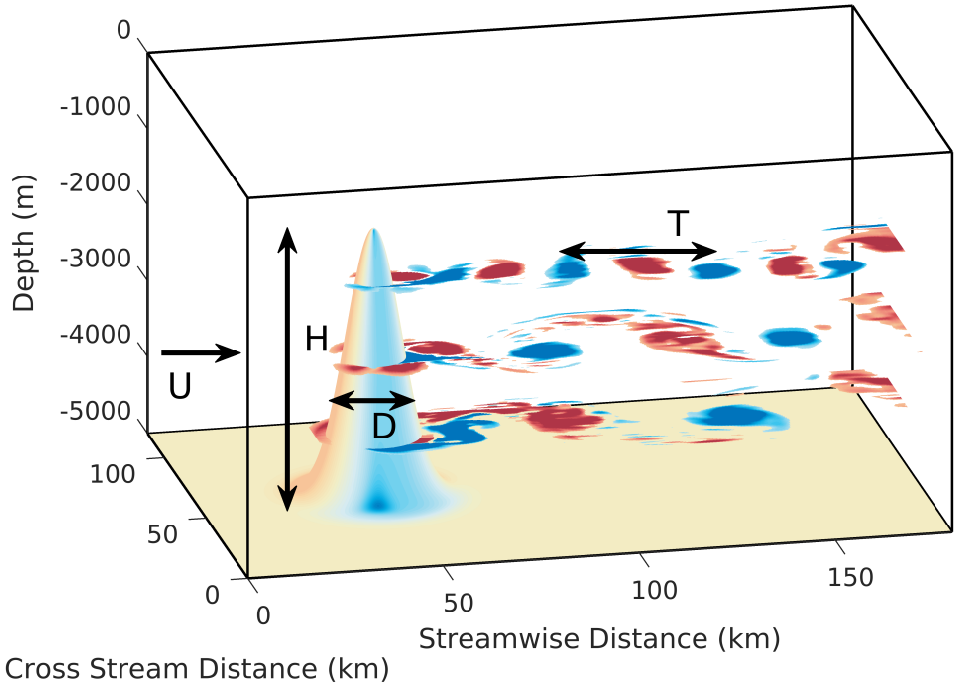

Figure 2.1: Schematic of the computational domain and inputs. A uniform velocity U and buoyancy frequency N are incident upon a mountain with characteristic height H and FWHM D. Vortices are shed with period T. An f-plane Coriolis parameter f is also present.

southern boundaries. The domain is discretized into a horizontal grid with $\frac{1}{3}$-km sides, and a variable vertical grid consisting of 80 levels. The overall grid measures $540 \times 360 \times 80$ cells.

The inflow velocity, U, is assigned a value of 0.1ms^{-1}. An unperturbed flow would then take approximately 21 days to pass completely through the domain. Each simulation is allowed to spin up for 60 days, and then run for an additional 80 days. Because the seamount dimensions and inflow velocity are fixed, the Froude and Rossby number are altered by manipulating N and f, respectively. These variables are independently set for each simulation, producing a variety of simulations spanning a range of Froude and Rossby number.

---

that are consistent with the northern hemisphere. In the southern hemisphere, the sense of the rotational terms would be reversed.

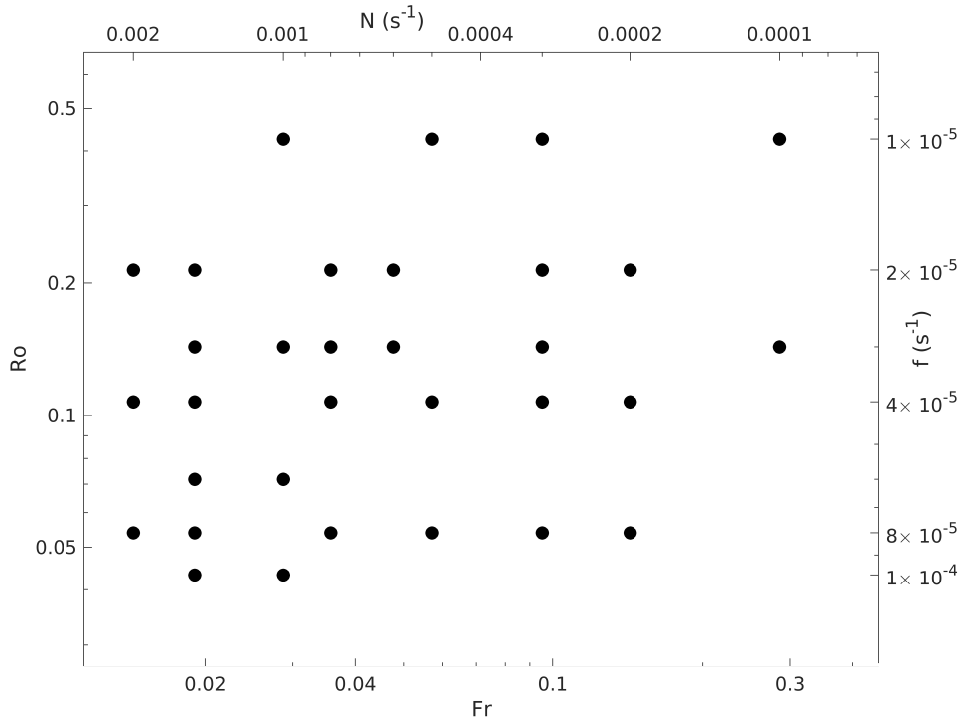

Figure 2.2: All of the simulations that were performed are plotted as dots. The double axes indicate the values of f and N that were used, as well as the equivalent Froude and Rossby numbers. Note the log-log scale.

2.2 Simulations Conducted

A substantial number of simulations were conducted, including sensitivity studies to validate the model performance. The set of 35 simulations that are used later for data analysis are presented in Figure 2.2 and Table 2.1.

Simulations were run using the Mox cluster, which is the University of Washington's primary high performance computing framework[2]. Each simulation required approximately 1500 CPU-hours to conduct and postprocess, producing approximately 100 GB of postprocessed output. For a typical simulation, the seamount produced vortex shedding, visualized in Figure 2.1. It was found that at large Froude and Rossby number, the wake tended to

[2]See the acknowledgements section at the beginning of this document for further infomation about Mox.

lose coherence and no longer produce discernible vortices. This limit served as the upper bound on Fr and Ro. The lower bound for the Rossby number was set by difficulties in maintaining model stability, and the Froude number lower bound was set by oceanographic considerations, as well as the limits of the vertical resolution. At very strong stratification, the vertical displacements would not be resolved by the vertical grid, and the simulations would not produce meaningful results.

f	N	Fr	Ro	Modified $k-\epsilon$ turbulence?
1×10^{-5}	1×10^{-4}	0.2857	0.4246	
1×10^{-5}	3×10^{-4}	0.0952	0.4246	
1×10^{-5}	5×10^{-4}	0.0571	0.4246	
1×10^{-5}	10×10^{-4}	0.0286	0.4246	
1×10^{-5}	30×10^{-4}	0.0095	0.4246	
2×10^{-5}	2×10^{-4}	0.1429	0.2123	✓
2×10^{-5}	3×10^{-4}	0.0952	0.2123	✓
2×10^{-5}	6×10^{-4}	0.0476	0.2123	✓
2×10^{-5}	8×10^{-4}	0.0357	0.2123	✓
2×10^{-5}	15×10^{-4}	0.0190	0.2123	✓
2×10^{-5}	20×10^{-4}	0.0143	0.2123	✓
3×10^{-5}	1×10^{-4}	0.2857	0.1415	
3×10^{-5}	3×10^{-4}	0.0952	0.1415	
3×10^{-5}	6×10^{-4}	0.0476	0.1415	
3×10^{-5}	8×10^{-4}	0.0357	0.1415	
3×10^{-5}	10×10^{-4}	0.0286	0.1415	
3×10^{-5}	15×10^{-4}	0.0190	0.1415	
3×10^{-5}	30×10^{-4}	0.0095	0.1415	
4×10^{-5}	2×10^{-4}	0.1429	0.1062	✓
4×10^{-5}	3×10^{-4}	0.0952	0.1062	✓

4×10^{-5}	5×10^{-4}	0.0571	0.1062	✓
4×10^{-5}	8×10^{-4}	0.0357	0.1062	✓
4×10^{-5}	15×10^{-4}	0.0190	0.1062	✓
4×10^{-5}	20×10^{-4}	0.0143	0.1062	✓
6×10^{-5}	10×10^{-4}	0.0286	0.0708	
6×10^{-5}	15×10^{-4}	0.0190	0.0708	
8×10^{-5}	2×10^{-4}	0.1429	0.0531	✓
8×10^{-5}	3×10^{-4}	0.0952	0.0531	✓
8×10^{-5}	5×10^{-4}	0.0571	0.0531	✓
8×10^{-5}	8×10^{-4}	0.0357	0.0531	✓
8×10^{-5}	15×10^{-4}	0.0190	0.0531	✓
8×10^{-5}	20×10^{-4}	0.0143	0.0531	✓
1×10^{-4}	10×10^{-4}	0.0286	0.0425	
1×10^{-4}	15×10^{-4}	0.0190	0.0425	
1×10^{-4}	30×10^{-4}	0.0095	0.0425	

Table 2.1: List of all simulations performed. The rightmost column indicates whether the simulation was run with a modified form of the $k - \epsilon$ turbulence model that is appropriate for energy analysis. Only these simulations are treated in Chapters 4 and 5.

2.3 Description of ROMS

ROMS (Regional Ocean Modeling System) is a 3D solver for the primitive equations, intended for use in simulating submesoscale oceanic motions. The primitive equations are a coupled set of nonlinear partial differential equations that describe the evolution of a fluid under

the Boussinesq[3] and hydrostatic[4] approximations. ROMS achieves turbulence closure using a variety of Reynolds-Averaged Navier-Stokes (RANS) formulations, which are discussed in Section 2.8. A complete description of ROMS is available in a manual, available as Hedstrom (2016). Because this is an evolving community code, many different versions exist. The model used for this dissertation is referred to as the "Rutgers" branch, Version 3.7, and is available at `www.myroms.org`. The details of the core solver are published as Shchepetkin (2003) and Shchepetkin and McWilliams (2005).

The equation set that is solved by ROMS is as follows:

$$\frac{\partial u}{\partial t} + \vec{u} \cdot \nabla u - fv = -\frac{\partial \phi}{\partial x} - \frac{\partial}{\partial z}\left(\overline{u'w'} - \nu \frac{\partial u}{\partial z}\right) + \mathcal{D}_u \tag{2.4}$$

$$\frac{\partial v}{\partial t} + \vec{v} \cdot \nabla v + fu = -\frac{\partial \phi}{\partial y} - \frac{\partial}{\partial z}\left(\overline{v'w'} - \nu \frac{\partial v}{\partial z}\right) + \mathcal{D}_v \tag{2.5}$$

$$\frac{\partial \phi}{\partial z} = \frac{-\rho g}{\rho_0} \tag{2.6}$$

$$\frac{\partial u}{\partial x} + \frac{\partial v}{\partial y} + \frac{\partial w}{\partial z} = 0 \tag{2.7}$$

$$\frac{\partial T}{\partial t} + \vec{u} \cdot \nabla T = -\frac{\partial}{\partial z}\left(\overline{T'w'} - \nu_\theta \frac{\partial T}{\partial z}\right) + \mathcal{D}_T \tag{2.8}$$

These equations account for evolution equations for u, v, and ϕ, the incompressibility condition, and an evolution equation for temperature. The density is determined by an equation of state (see Eq. 2.11.) $\mathcal{D}$ indicates the effect of modeled diffusion and dissipation; the exact models for these terms can vary, but those used for the present study are indicated in Table 2.3. The Reynolds stresses and turbulent temperature flux are also modeled (see Section 2.8.)

While originally ROMS was designed to perform refined runs on regional sections of a global circulation model, it has also been used for modeling smaller domains such as a river

[3]The Boussinesq approximation ignores variations in density, except when considering buoyant forces. This assumption introduces an error on the order of the ratio of the overall density variation to the average density. In the ocean, this error usually does not exceed 0.3%.

[4]The hydrostatic approximation asserts that the pressure at a location is only the hydrostatic pressure at that point. The dynamic pressure is thus neglected. This assumption dramatically reduces computation time, but comes with limitations, which are described in Section 2.10.

outlet (MacCready and Giddings, 2016), and performing idealized simulations (e.g. Dong et al., 2007; Boutov et al., 2010; Caldeira and Sangrà, 2012; Perfect et al., 2018). As long as the required resolution and dynamics do not violate any of the assumptions in the model formulation, these nonstandard uses can be considered to be faithful simulations. In an idealized configuration such as this study, the bathymetry, initial conditions, and boundary conditions can be specified mathematically.

2.4 Domain and Initialization Files

In the configuration used for this study, ROMS expects three input files, and outputs three different results files. All of the I/O is conducted using the NetCDF[5] file format. The input files are:

- The computational grid (ocean_grd.nc)
- The initial conditions (ocean_ini.nc)
- The boundary conditions (ocean_bry.nc)

The output files are:

- The history file (ocean_his.nc)
- The time-averaged file (ocean_avg.nc)
- The checkpoint file (ocean_rst.nc)

The grid, initial, and boundary files are written with a python script and stored as arrays in the NetCDF file format. The grid describes a symmetric Gaussian with height 3500m and characteristic length 10km (see Figure 2.1). The domain is 120km in the cross stream direction and 180km in the streamwise direction. The depth is 5000m, with 80 resolved vertical levels. The horizontal mesh spacing is 333 m.

[5]see `www.unidata.ucar.edu/software/netcdf/`

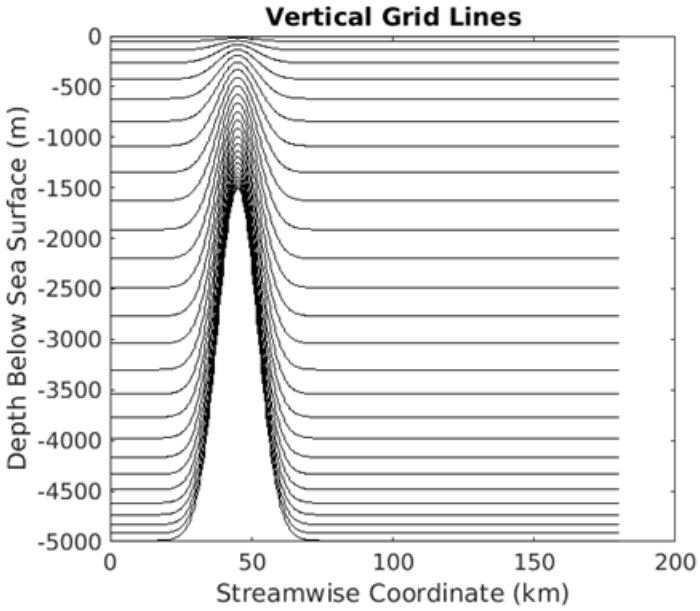

Figure 2.3: Demonstration of the sigma coordinates used in the present model. The water column is discretized by a constant number of vertical levels, independent of the local ocean depth.

ROMS uses terrain following (sigma) coordinates, and a vertical grid stretching function. As shown in Figure 2.3, this coordinate system indexes fractional sections of the water column, regardless of the local water column depth. This formulation is known to create a fictitious pressure gradient force where there exists significant slope between two grid points at the same vertical level, but steps are taken to mitigate this as much as possible (Shchepetkin, 2003). The vertical grid stretching function is typically used to produce a higher vertical resolution near the surface of the ocean though, for this model, we are more interested in processes that happen in the bottom and middle of the water column. For this model, then, the stretching function is specified as Vertical Transformation 2, Vertical Stretching 4[6], with parameters $\theta_b = 3$ and $\theta_s = 0.65$. These settings correspond to minimal surface refinement, and maximum resolution in the mid-domain and at the bottom boundary.

[6]This algorithm is attributed to Shchepetkin in 2010, but is unpublished outside of the ROMS source code.

These choices are in line with the project goals of looking at open ocean interaction with topography.

The initial and boundary conditions prescribe a uniform flow in geostrophic balance, with constant buoyancy frequency. An f-plane Coriolis parameter is used. The geostrophic balance is achieved by using the free surface field, ζ, which is defined to be,

$$\zeta(x, y) = \frac{fyU}{g}. \tag{2.9}$$

This tilted free surface balances the Coriolis acceleration and maintains a uniform eastward flow. The initial conditions code can also be configured to accept a vertically-varying velocity field. In this case, the background density field must be set with a thermal wind balance:

$$\rho(x, y, z) = \rho_0 + \frac{\rho_0}{g} \int_{y_0}^{y} f \frac{\partial u}{\partial z} dy - \frac{N^2 \rho_0 z}{g}. \tag{2.10}$$

Care must be taken when considering a vertically-varying velocity, because strong vertical shear, in conjunction with weak stratification, can result in an unstable density profile. In addition, this procedure threatens to invalidate the concept of a spatially-uniform buoyancy frequency. While this is inevitable in a real ocean, introducing a spatially-varying buoyancy frequency in the simulations significantly complicates the set of parameters that are being investigated. For this reason, the simulations in this study maintain a uniform velocity, and therefore a uniform buoyancy frequency.

2.5 Boundary Conditions

For a 3D simulation, ROMS expects boundary conditions for each of the four cardinal directions. The free surface is solved for by the model, and the bottom boundary is treated with a bottom stress condition, to be discussed in Section 2.9. At each horizontal boundary, the following variables must be specified: depth averaged velocity[7] $(\bar{u}, \bar{v})$, 3D velocity (u, v), sea surface height (ζ), turbulent kinetic energy (k), and any tracers that are used (e.g., temperature, salt, dye). For the present model, the only tracer considered is temperature (T); the

[7]in ROMS, the exact terminology used is "ubar," which is referred to as the depth-averaged momentum

fluid temperature is an active tracer that prescribes the fluid density with the equation of state:

$$\rho = \rho_0 - \frac{1.7 \times 10^{-4}}{^\circ\mathrm{C}} \rho_0 \left(T - 10^\circ\mathrm{C}\right), \tag{2.11}$$

where T is the fluid temperature.

The model boundary conditions for each of the required quantities are given in Table 2.2. The meanings of these specifications are described below:

Variable	North	South	East	West
Free Surface	Che	Che	Che	Che
$\bar{u}$	Shc	Shc	Shc	Shc
$\bar{v}$	Shc	Shc	Shc	Shc
u	RadNud	RadNud	RadNud	RadNud
v	RadNud	RadNud	RadNud	RadNud
T	RadNud	RadNud	RadNud	RadNud
k	Gra	Gra	Gra	Gra

Table 2.2: Boundary conditions for the present study

- Che, or Chapman Explicit, forces all free surface perturbations to leave the domain at the shallow water speed:

  $$\frac{\partial \zeta}{\partial t} = \pm\sqrt{gL}\frac{\partial \zeta}{\partial x} \tag{2.12}$$

  It is adapted from the Chapman Implicit condition, and altered to be less dissipative and reflective.

- Shc, or Shchepetkin, "radiates deviations from exterior values at the speed of the external gravity waves." For a depth-averaged velocity, $\bar{u}$ and a specified exterior velocity, $\bar{u}^{\mathrm{ext}}$,

  $$\bar{u} = \bar{u}^{\mathrm{ext}} - \sqrt{\frac{g}{D}}(\zeta - \zeta^{\mathrm{ext}}). \tag{2.13}$$

It is adapted from the Flather condition, in order to run with a staggered mesh.

- Gra, or Gradient, enforces a Neumann boundary condition:

$$\frac{\partial \psi}{\partial x} = 0, \tag{2.14}$$

for a generic field variable, ψ.

- RadNud, or Radiation with Nudging, is a variation on an open boundary condition. For horizontal wave speeds c_x and c_y, and a generic field variable ψ,

$$\frac{\partial \psi}{\partial t} + c_x \frac{\partial \psi}{\partial x} + c_y \frac{\partial \psi}{\partial y} = -\frac{1}{\tau}(\psi - \psi^{\text{ext}}). \tag{2.15}$$

In the above expression, τ is a forcing timescale that assumes one of two user-specified values, depending on the signs of c_x and c_y. In this model, the outflow timescale is 1 day and the inflow timescale is 0.1 days. Physically, the radiation with nudging condition acts as a restoring force that causes the flow to more closely resemble the chosen flow specification.

2.6 Model Configuration

ROMS is based in Fortran, and exists as an amalgamation of Fortran files. The settings for any particular model are specified using C preprocessing; only the portions of Fortran files that are relevant for that model are selected by the preprocessor and then compiled. Therefore, the physics settings for a given simulation can be specified in terms of the C preprocessing flags that are passed to the compiler. Table 2.3 lists the flags that were used for the present simulations, along with a brief description of the purpose of each flag. This combination of flags can be used to recreate the model settings used in this study.

2.7 Timestepping

ROMS solves for both the 3D (baroclinic) mode and the 2D (barotropic) mode. Because the barotropic mode has a faster timescale, its timestep is much smaller than that of the

baroclinic mode. In its present configuration, the model uses a baroclinic timestep of 20s, and contains 30 barotropic steps per baroclinic step. These timesteps correspond to a Courant number of approximately 0.25. Timestepping guidelines exist for ROMS (e.g., the Courant number should be limited to below 0.85), but for a given simulation, it is impossible to determine an 'ideal' timestep a priori (Hedstrom, 2016). In general, the timestep should be as large as possible while still remaining numerically stable. This limits the dissipative effects of a finite difference code. We find that in determining model stability, the Coriolis parameter is active dynamically, and serves as the most restrictive variable for determining a maximum timestep. Therefore, the largest stable timestep for the cases with the strongest rotation was used across all simulations. In maintaining consistency between model runs, the most restrictive timestep for any one model was used for all of the runs.

The models were run in two segments. In the initialization run, the model was run out to approximately 60 days in order for the flow to develop. Then, the last checkpoint file was used as the initial condition for a new run of approximately 80 days. The residence time of the unperturbed flow in the domain was approximately 21 days.

2.8 Turbulence Model

ROMS relies on turbulent viscosity modeling to achieve turbulence closure. Scaling arguments dictate that the horizontal Reynolds stresses are insignificant due to the very small horizontal gradients of turbulence quantities, especially when compared to the corresponding vertical gradients, and so they are neglected in ROMS. The Reynolds stresses and temperature fluxes associated with a vertical velocity are modeled via one of two schemes: Large-McWilliams-Doney (LMD) (Large et al., 1994), and Generic Length Scale (GLS) (Umlauf and Burchard, 2003; Warner et al., 2005). LMD is a one-equation model that unites a series of laboratory and observational results into an empirical model for the turbulent viscosity. The GLS model, proposed by Umlauf and Burchard (2003), and implemented by Warner et al. (2005), may be tuned to act as any two-equation closure model. For this model, the GLS scheme is tuned to act as a $k - \epsilon$ model. The diapycnal mixing has a slight depen-

dence on the turbulence model used; Robertson (2006) compares several ROMS simulations of Fieberling Guyot using a variety of turbulence models.

The default behavior of the $k-\epsilon$ model is to enforce a minimum value for the turbulent kinetic energy (tke), k, of $7.6 \times 10^{-6} \frac{\mathrm{m}^2}{\mathrm{s}^2}$. This value produces unrealistic mixing values for high-resolution models, and so the minimum k is reduced to $10^{-10} \frac{\mathrm{m}^2}{\mathrm{s}^2}$. With this modification, the minimum TKE in the domain is reduced by approximately 4 orders of magnitude, and the background mixing is reduced such that the effects of eddy processes can be resolved.

2.9 Bottom Stress

The bottom of the domain in ROMS is treated with a bottom stress condition. Bottom stress is an integral component to modeling topographic wakes; it is responsible for the majority of the vorticity generation and controls much of the tke that is generated in the flow. The oceanographic community simultaneously recognizes three separate bottom stress treatments. The bottom boundary layer velocity profile may be assumed to be linear, quadratic, or logarithmic. Recent arguments suggest that a quadratic boundary profile may be more suited, especially to deep oceans (Arbic and Scott, 2008). A more recent discussion of bottom drag is presented by Warner and MacCready (2014). The quadratic drag coefficient is set to 2×10^{-3}, though sensitivity studies have also been performed.

2.10 On the Practical Limitations of a Hydrostatic Model

Marshall et al. (1997) describe two commonly encountered limitations to the primitive equations: the advective timescale must be much less than the buoyancy period, and the horizontal Coriolis term must be small compared to the horizontal advection of momentum. These are formalized as:

$$\left(\frac{U}{D^* N}\right)^2 \ll 1 \tag{2.16}$$

$$\frac{f h_c \cos\phi}{U} \ll 1, \tag{2.17}$$

where D^* is a horizontal length scale, ϕ is the latitude on the Earth, and h_c is an appropriate scale for the vertical motion.

The validity of these approximations will be evaluated over the expected parameter range for an oceanic seamount. For the limitation in Eq. 2.16, the most important factor is the buoyancy frequency. In the ocean, N can vary from 3×10^{-3} rad/s in the pycnocline down to essentially zero in the mixed boundary layers at the top and bottom. King et al. (2012) report abyssal values as low as 2×10^{-4} rad/s that seem to be above the mixed layer at the bottom. Ocean currents may be arbitrarily small and reach maximum speeds of up to 2.5 m/s. However, abyssal flows generally do not exceed several centimeters per second.

In strongly stratified flow past an obstacle, vertical motion typically only occurs for a height scale of approximately $h_c = \frac{U}{N}$. For a Gaussian with a FWHM of D, the horizontal length scale D^* is approximately $D\sqrt{\mathrm{Fr}}$ [8]. Substituting this into 2.16, we obtain,

$$\frac{U}{D^* N} \approx \frac{U\sqrt{NH}}{DN\sqrt{U}} = \sqrt{\frac{U}{NH}}\frac{H}{D} = \sqrt{\mathrm{Fr}}\frac{H}{D}. \tag{2.18}$$

Therefore, Eq. 2.16 reduces to the requirement that the product of the Froude number and the seamount aspect ratio be small. For the simulations conducted in this study, both the aspect ratio and Froude number do not exceed $O(0.1)$, and so

$$\left(\frac{U}{D^* N}\right)^2 \approx O(10^{-4}). \tag{2.19}$$

In the ocean, we may calculate a minimum value of the topographic length scale that satisfies the hydrostatic requirement. In a worst-case abyssal flow (fastest possible flow and lowest possible buoyancy frequency),

$$(D^*)^2 \gg \left(\frac{U}{N}\right)^2 = \left(\frac{0.1\mathrm{m/s}}{2 \times 10^{-4}\mathrm{s}^{-1}}\right)^2 = (500\mathrm{m})^2 \tag{2.20}$$

Exceeding the minimum characteristic length scale by an order of magnitude ensures that Eq. 2.16 is satisfied by two orders of magnitude due to the square nature of the equation.

[8] See Equations 5.7-5.9 for a more thorough discussion of this scaling.

A seamount with a length scale of 5 km and an average slope of 4 degrees (considered to be fairly steep) would have a height of 350 m. Therefore, we expect that most seamounts will satisfy this restriction.

For the limitation in Eq. 2.17, Ω has a constant value of 7.29×10^{-5} rad/s, and $\cos\phi$ has an upper bound of 1, but is typically approximated as $\frac{1}{2}$ for mid-latitude waters, so the requirement reduces to

$$\frac{h_c}{U} \approx \frac{1}{N} \ll 13718 \approx 10000. \tag{2.21}$$

Here we have made the assumption that h_c can be approximated as $\frac{U}{N}$. In terms of a seamount, this restriction can be summarized as a lower bound on the buoyancy frequency,

$$N \gg 10^{-4}\mathrm{s}^{-1}. \tag{2.22}$$

For the simulations conducted, the lowest buoyancy frequency is $2 \times 10^{-4}\mathrm{s}^{-1}$, which may push the limits of this assumption, but the largest buoyancy frequencies considered clearly satisfy it. In the abyssal ocean, very low buoyancy frequencies have been measured; there are undoubtedly seamounts that violate Eq. 2.17.

The more general condition from which Eq. 2.17 was derived is,

$$\frac{Du}{Dt} \gg 2\Omega w \cos\phi \approx 7.29 \times 10^{-5} w. \tag{2.23}$$

The most likely location where this condition would possibly be violated is where the flow is forced over the seamount, giving the flow a vertical velocity. The upper bound on w can be assumed to be constrained by the slope of the seamount, such that with our 4-degree seamount, $w \approx 0.07u$ and

$$\frac{\partial u}{\partial \vec{x}} \gg 4.4 \times 10^{-6}. \tag{2.24}$$

Some basic scaling indicates that this limit is low enough that turbulent fluctuations in velocity should dominate the vertical term.

Overall, it is reasonable to conclude that the use of a hydrostatic model is justified for this study.

2.11 Model Validation and Convergence Testing

Previous studies have simulated real and idealized seamounts in a variety of flow conditions. Several realistic simulations have achieved a good qualitative match to the flow fields observed around real seamounts (Beckmann and Haidvogel, 1997; Robertson, 2006; Caldeira and Sangrà, 2012). Because it is not practical to obtain observations from a real seamount, to a certain extent we rely on the validation efforts of previous modelers. In particular, Dong et al. (2007) and Dong and McWilliams (2007) describe a ROMS model for idealized flow past an island, and then subsequent realistic modeling for islands in the Southern California Bight. This pair of papers instills confidence that the ROMS models used for the idealized island can be extended to accurately reproduce observed flow patterns for real islands. As an initial validation, the results from Dong et al. (2007) were reproduced using the same model that is used for the present study. This initial work was then used as a starting point for adapting the study to look at seamounts. While the simulation results presented here cannot be directly validated, we have a reasonable degree of confidence that validation by Dong and McWilliams (2007) can be extended to the present study.

In order to ensure that the model results were robust to changes in various model parameters, convergence tests were conducted, as detailed below.

2.11.1 Grid Spacing

The grid spacing was originally set to one horizontal grid point per kilometer in both horizontal directions. On subsequent tests, the number of grid points per kilometer was incremented by one, until the wake pattern was not affected by increased grid resolution. It was determined that a grid spacing of 3 grid points per kilometer was sufficient to capture the relevant wake structure. A similar method was used to select the proper number of vertical levels, ultimately settling on 80.

2.11.2 Bottom Drag

The quadratic bottom drag coefficient was varied geometrically from 5×10^{-4} to 8×10^{-3}, about the central value of 2×10^{-3}, which is a community-accepted value for regional ocean models (Arbic and Scott, 2008). Full simulations were run for each of these three values, and then the Strouhal number[9] was calculated for each vertical level, along with some basic energetics parameters. As will be explored in Chapter 3, the Strouhal number is a convenient parameter for describing the bulk character of the flow, and it is used here to investigate bottom drag sensitivity. We find that the Strouhal number generally decreases as the bottom drag is increased, which is consistent with previous studies of flow past a cylinder (Ahlborn et al., 2002), although the wake structure is not qualitatively altered (see Figure 2.4). The energetic effect of increasing the bottom drag is strongly dependent on depth. Above the bottom boundary layer, changing the bottom drag does very little (the bottom drag is applied across the whole bottom, including the seamount). In the lowest 500m of the domain, the increased bottom drag necessarily increases the energy conversion into eddy and turbulent kinetic energy, as well as mixing. This is to be expected because the increased bottom drag coefficient must result in increased bottom stress, which must be reflected in the hydrodynamics.

2.11.3 Explicit Viscosity

The model equations include an explicit kinematic viscosity term, ν_N. While Dong et al. (2007) reports being able to rely on numerical viscosity alone to achieve model stability, the present simulations were unstable without explicit viscosity. Viscosity may be specified as either a Laplacian viscosity, or a hyperlaplacian formulation. Model runs were conducted with both, but it was determined that a Laplacian viscosity of $1 \frac{\mathrm{m}^2}{s}$ provided the best balance of model stability and highly-resolved eddy structures. The Reynolds number of the present

[9]The Strouhal number is a dimensionless frequency associated with eddy shedding. It is defined as $\frac{D}{UT}$, where T is the period of vortex shedding. See also, Section 3.1.

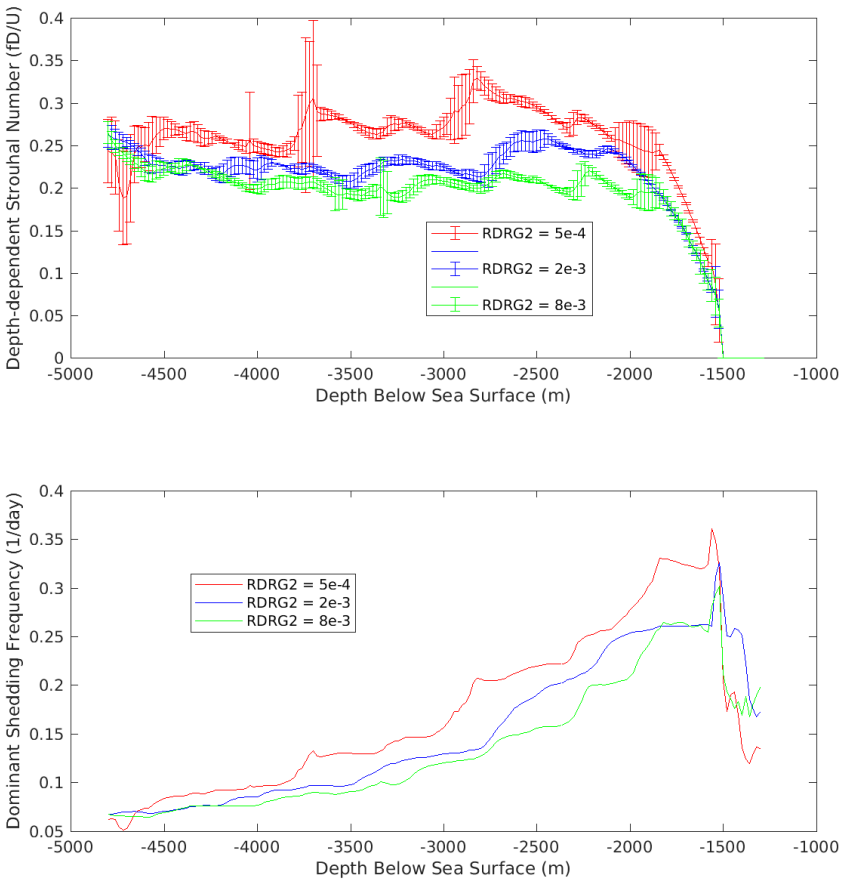

Figure 2.4: Several key parameters are plotted for three values of the bottom drag coefficient.

simulations, based on $\frac{UD}{\nu_T}$, is approximately 2000. In the systematic viscosity convergence studies performed by Dong et al. (2007), this Reynolds number produced results that were nearly indistinguishable from the zero-viscosity model. Consequently, we are able to resolve many of the finescale eddy structures that drive mixing.

2.12 Postprocessing

The model outputs are in sigma coordinates. In order to compute mixing and energy conversion values from the data, it is necessary to interpolate the output files to a Cartesian grid. The vertical data are interpolated to a uniformly-spaced 50-m vertical grid. Thus, the size of the analysis domain is 540 by 360 by 100 grid cells.

Option	Description
UV_ADV	Compute nonlinear advection terms
UV_COR	Compute Coriolis force
UV_QDRAG	Model bottom drag with a quadratic drag coefficient
UV_VIS2	Compute horizontal viscosity using an explicit Laplacian viscosity
MIX_S_UV	Harmonic mixing along lines of const density
SPLINES_VDIFF	Construct splines to obtain vertical diffusion
SPLINES_VVISC	Construct splines to obtain vertical viscosity
TS_U3HADVECTION	3rd order upstream horizontal advection of tracers
TS_C4VADVECTION	4th order centered vertical advection of tracers
DJ_GRADPS	Compute pressure gradients using splines density Jacobian
TS_DIF2	2nd order diffusion of tracers
MIX_S_TS	Tracers are mixed along surfaces of constant S
SOLVE3D	Solve for baroclinic modes in addition to barotropic modes
ANA_*FLUX	All surface and bottom fluxes are analytically set to zero
GLS_MIXING	Use the Generic Length Scale turbulence closure scheme
N2S2_HORAVG	Horizontal smoothing of buoyancy/shear
K_C4ADVECTION	4th order centered advection of k
KANTHA_CLAYSON	Activate Kantha and Clayson stability function

Table 2.3: C Preprocessing flags that were used in the ROMS model for this study.

Chapter 3

VORTEX STRUCTURES

The patterns in vorticity that manifest in seamount wakes will be analyzed in this chapter. In addition, the mechanisms that are responsible for creating different vortex regimes will also be discussed. This work has been published in *Geophysical Research Letters* as Perfect et al. (2018).

3.1 Vorticity Analysis

The output from the simulations described in Figure 2.2 is organized as 4D arrays (3 spatial dimensions, and time) for each variable of interest. The best suited quantity for flow visualization is the relative vorticity, ξ (referred to hereafter as the vorticity[1]). In general, the vorticity, $\vec{\omega}$, is defined as the cross product of the velocity ($\nabla \times \vec{u}$). ROMS outputs only the vertical component of the vorticity, and so this is the quantity that will be used for this the analysis in this chapter. For notational simplicity, then, we define

$$\xi \equiv \frac{\partial v}{\partial x} - \frac{\partial u}{\partial y}. \tag{3.1}$$

The vorticity, as seen in figures 5.3 and 2.1, is useful for identifying eddy structures. Cyclonic and anticyclonic eddies will show up as regions of significant positive and negative vorticity, respectively. To a certain extent, isosurfaces in the vorticity, as shown in Figure 3.1, are useful for identifying the locations of eddies. However, it is challenging to automatically identify and track eddies in space and time. Vortex tilting and breakdown due to flow instabilities and turbulence tend to resist automated vortex tracking. Srinivasan et al. (2019) reports

[1]The potential vorticity (PV) is another quantity of importance, but it is less useful for flow visualization and the present investigation into vortex structures. The PV will be explicitly mentioned as such, but the relative vorticity will be shortened to the vorticity.

some success employing a vortex tracking algorithm for a similar seamount wake project, but such a process is not used for this work.

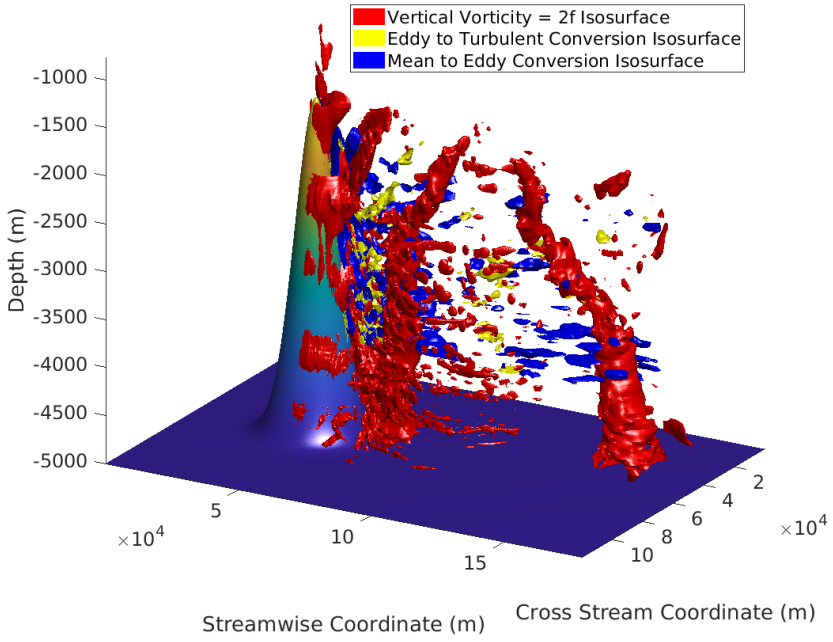

Figure 3.1: A typical vorticity isosurface.

Instead, we consider time series in the vorticity field. As an eddy advects past a point, a signature in the time series of the vorticity at that point marks the passage of the eddy (see Figure 3.2a). The frequency of the peaks in the vorticity can be used to obtain an important quantity for flow past an obstacle– the Strouhal number,

$$\mathrm{St} \equiv \frac{D(z)}{UT}, \tag{3.2}$$

where $D(z)$ is the local, vertically-varying seamount diameter, U is the ambient flow speed, and T is the period associated with the vorticity peaks. For a broad range of Reynolds numbers, flow past a circular cylinder tends to produce vortex shedding with $0.2 \leq \mathrm{St} \leq 0.25$

Achenbach (1972). With the Strouhal number, then, we can evaluate the extent to which flow past a seamount conforms to the expectations for flow past a cylinder.

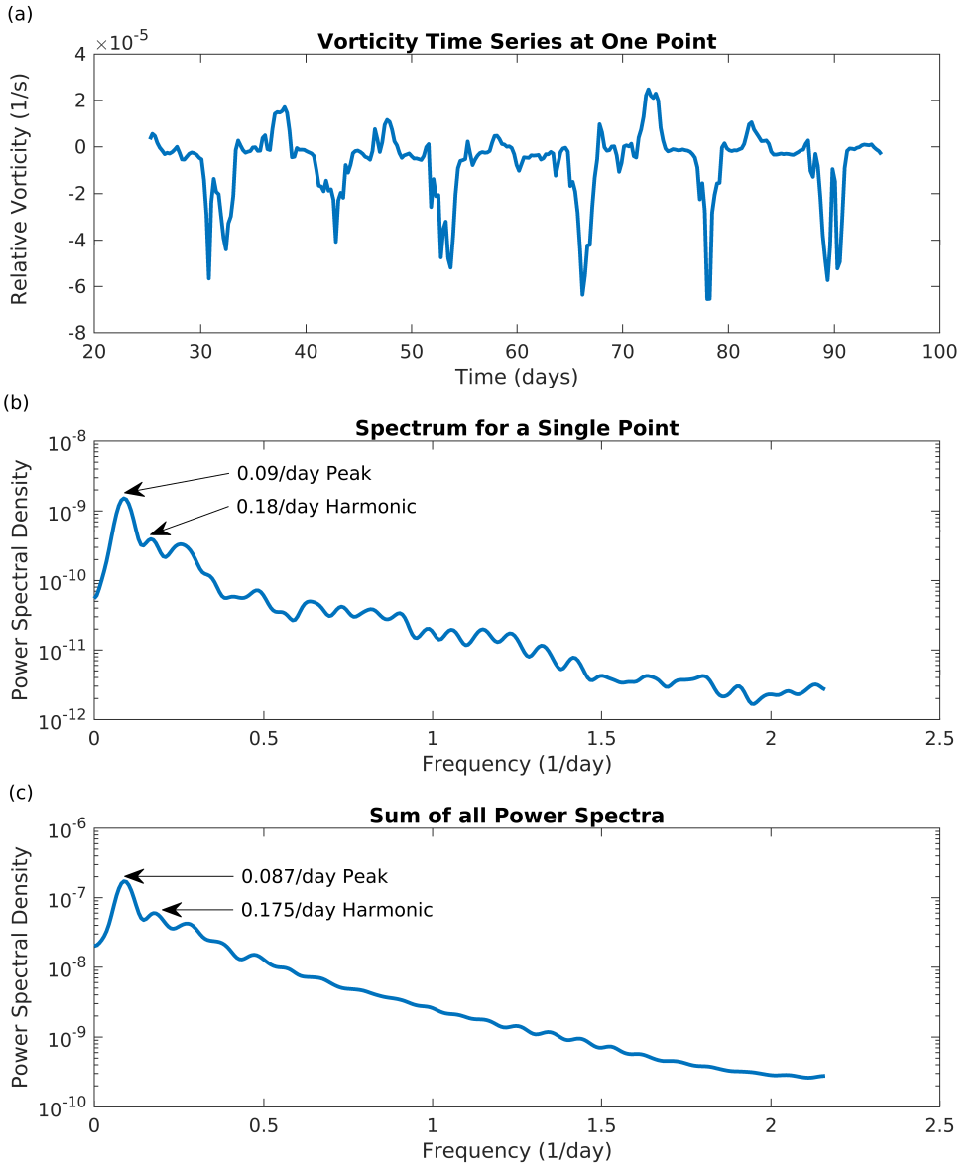

Figure 3.2: (a) The relative vorticity time history for a typical point, (b) The power spectrum of the plot in (a), (c) The summation of all power spectra for an ensemble of test points located at the same depth.

The eddies, under the influence of planetary vorticity and the effects of nearby eddies,

tend to take a meandering course, and so it is not possible to reliably measure the passage of eddies with a single point. Therefore, an ensemble of points is used, arranged in a 3D grid in the lee of the seamount. A horizontal slice of the ensemble is shown in Figure 3.3. The power spectral density (PSD) of the time series for each point is estimated using the periodogram; a typical PSD function is shown in Figure 3.2b. The base frequency for this case of 0.09 day^{-1} is shown, along with a harmonic. In some cases, the power associated with the harmonic exceeds that of the actual frequency. This is a consequence of vortices existing as discrete units; the time history of vorticity tends to contain sharp peaks, separated by a duty cycle of essentially zero vorticity. When transformed into frequency space, this pattern manifests as strong harmonics. The PSD functions are summed together for each vertical level, producing an overall PSD function for each vertical level in the domain. A typical summed PSD is shown in Figure 3.2c. The peak of 0.087 day^{-1} is obtained. We compute the Strouhal number using this peak in the summed PSD function. Once again, it is possible for harmonics to be stronger than the base frequency; visual confirmation was a vital tool in corroborating the results of this analysis. To visually confirm the spectral analysis, a movie of the vorticity for a horizontal surface was played, and the eddies were counted manually.

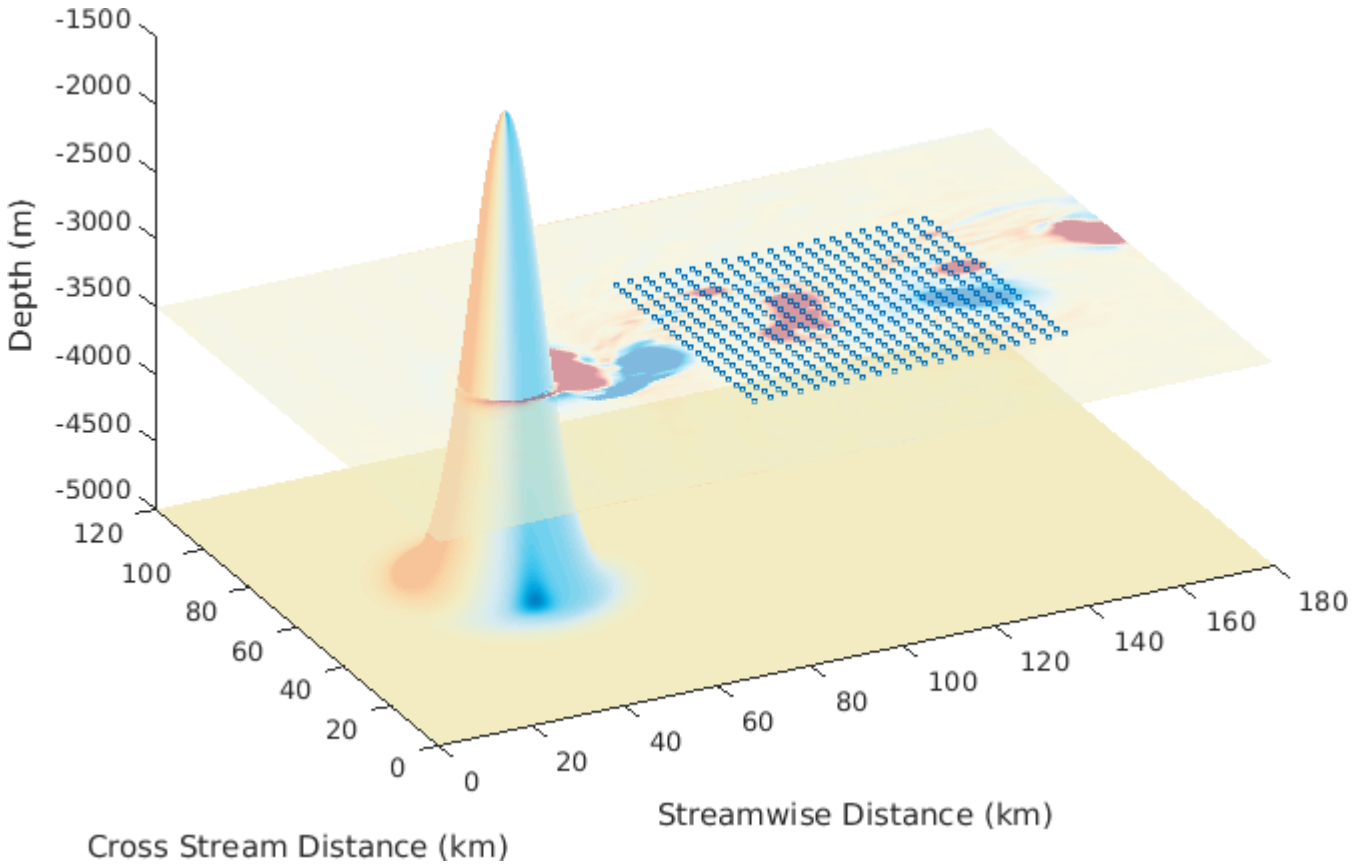

Figure 3.3: The horizontal ensemble of points used to compute the Strouhal number are indicated as blue circles.

Figure 3.4 demonstrates some of the patterns in the eddies, shedding frequency, and Strouhal number that can emerge. On the right hand side of the figure, images of the vorticity are shown at four different depths. Changes in the local diameter of the seamount, $D(z)$ are clearly evident as the white circle changes size between images. The frequency of eddy shedding, shown in the blue line for this particular case, decreases with depth. However, because the Strouhal number also depends on the local seamount diameter, shown as the red line in Fig. 3.4, the Strouhal number is approximately the same across the entire depth. This analysis is leveraged in the next section to classify the different types of vortex structures.

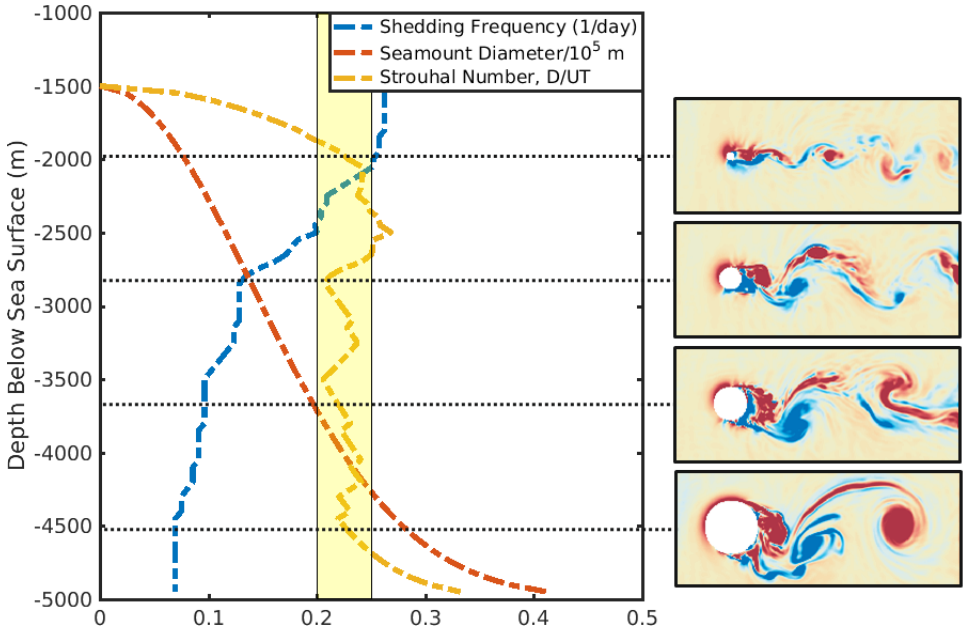

Figure 3.4: A graphical representation of vertical variation in the shedding frequency and Strouhal number. The shedding frequency and Strouhal number are plotted in blue and orange, respectively. A red line in the shape of the seamount is also plotted, along with snapshots of the vorticity at different vertical levels to the right of the main plot.

3.2 Vertical Vortex Structure

When subjected to uniform flow, the seamount produces a hydrodynamic wake. In most cases, the wake takes the form of coherent vortices, as illustrated in Figure 3.5. In the limiting case of large Fr and large Ro (i.e., tending towards nonrotating, unstratified flow), the wake exhibits 3-D turbulence, which prevents the formation of coherent vertically-oriented vortices (Barkley and Henderson, 1996). This type of wake structure will not be discussed, in favor of the larger vortex structures that form in rotating, stratified flow. While the wake structure may bear some resemblance to previous stratified wake studies (e.g., Lilly, 1983; Billant and Chomaz, 2001; Spedding, 1997), the additional effect of rotation produces a fundamentally different scaling behavior, which is discussed in Section 3.3.

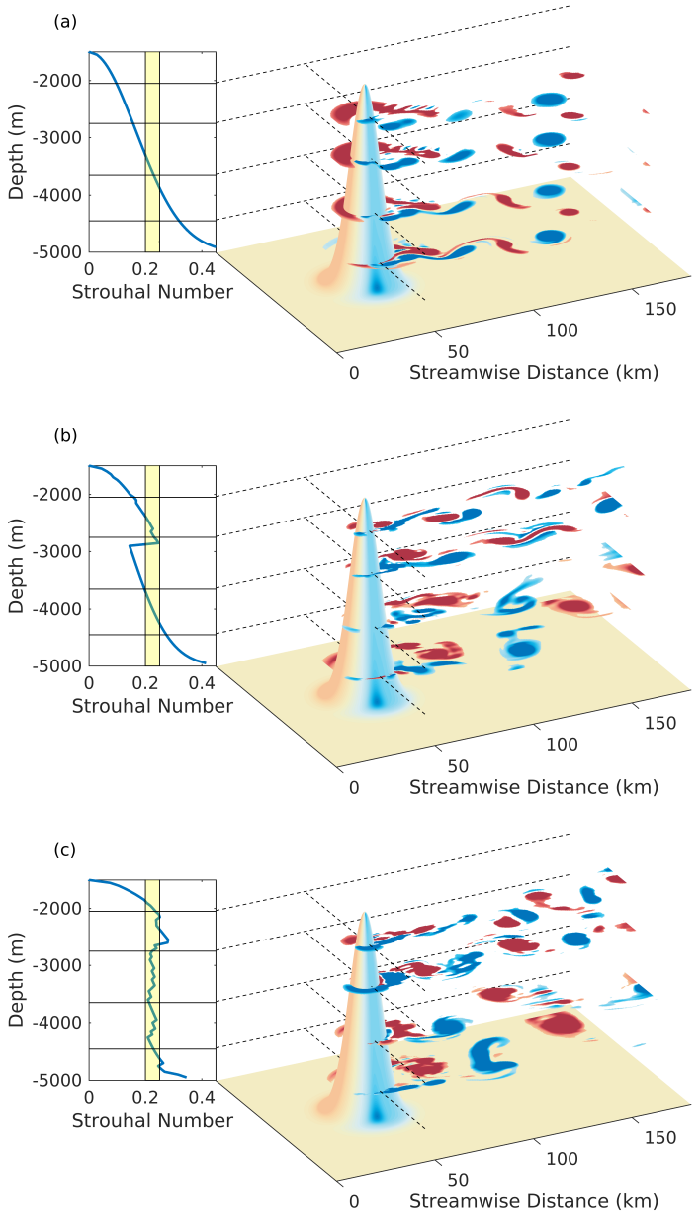

Figure 3.5: Results from three simulations are presented, which exhibit typical cases of the shedding regimes that were produced. Horizontal slices of the vertical vorticity are overlaid on the topography. In the top case (Ro = 0.14, Fr = 0.095), vortices are vertically-aligned. The middle case (Ro = 0.14, Fr = 0.048) is a transitional regime, characterized by two regions of uniform shedding, separated by an interface where the shedding frequency changes abruptly. In the bottom case (Ro = 0.42, Fr = 0.029), vortices are fully decoupled. The vertically-varying Strouhal numbers are indicated to the left, with a typical Strouhal number for high-Re flow highlighted.

The vertical structure of the vortices may be categorized into two regimes, separated by a small transitional regime. The first regime, shown in the top plot of Figure 3.5 and characterized by weak stratification and strong rotation, exhibits vortex lines that are vertical or slightly tilted, extending from the bottom boundary layer up to the level of the seamount summit. Vortices are shed in a vertically-uniform manner, resulting in a uniform shedding frequency at all elevations of the seamount. The Strouhal number, based on the local seamount diameter, therefore varies significantly over the height of the seamount. The vortex lines produced by this shedding are not Taylor columns, because they do not necessarily extend beyond the seamount summit, with the distinction of being controlled by the ratio of seamount height to water depth (Boyer and Chen, 1987). These structures are qualitatively consistent with the vertically-uniform eddies seen in laboratory experiments by Hunt and Snyder (1980) and Castro et al. (1990). However, as we will demonstrate, rotation is necessary to produce coupled shedding in our simulations, whereas these experiments only considered stratification. The observed coupled vortex structures may be due to one of several influences in the experiments. We note that both studies used seamounts with an aspect ratio near unity, and were conducted at low Reynolds number, and for relatively short periods of time. All of these were due to practical considerations for the experiments, but may explain why the eddies were vertically aligned.

In the second regime, characterized by strong stratification and weak rotation, vortices become decoupled in the vertical direction (see Figure 3.5c). That is, rather than each vortex shedding as a vertical unit, each seamount elevation sheds vortices independently. The shedding frequency varies strongly with depth, with the bottom of the seamount shedding at roughly an 8-day period, and the seamount summit shedding at 3-4 day intervals. Vortex lines may have significant vertical extent, but as suggested by Canals et al. (2009), the sloping seamount flank causes them to become strongly tilted with successive shedding periods, ultimately breaking down.

Because of the strong vortex tilting and temporal variability, we are not able to reliably obtain a vertical scale for the eddies in the decoupled regime. It is clear from the coupled

regime, however, that the vertical scaling of $\frac{U}{N}$ suggested by Lilly (1983) and Billant and Chomaz (2001) for purely stratified systems does not apply here; the vortices spanning the entire height of the mountain exceed this scale. In general, the presence of rotation encourages taller vortices. Srinivasan et al. (2019) utilizes vortex tracking algorithms for a similar set of simulations and finds that vortices have a vertical to horizontal aspect ratio of $\sqrt{\frac{f}{N}}$, in contrast to the quasigeostrophic result of $\frac{f}{N}$ (Otheguy et al., 2006; Dritschel and De La Torre Juárez, 1996). In the coupled regime, our results match the quasigeostrophic scaling, but we are unable to obtain an aspect ratio for the decoupled regime.

The bottom plot of Figure 3.5 gives insight into the distribution of shedding frequency; the vertical decoupling of eddies works to preserve a relatively constant Strouhal number. This Strouhal number matches the behavior observed for high-Reynolds number flow past a circular cylinder (Zdravkovich, 1997). Therefore, averaged over the length of the simulation, each vertical level acts somewhat independently, almost as a two-dimensional plane. The type of vortex shedding produced in this regime has not been reported in literature, although Figure 1.2 suggests that this may be due to the regime lying outside of the parameter space that has previously been investigated.

A transitional regime, indicated by Figure 3.5b, separates the two shedding behaviors. Rather than varying continuously, the shedding frequency exhibits a small, finite number of jumps, separated by regions of uniformity. In the following section, we will discuss the mechanisms responsible for the transition from a vertically-varying to a vertically uniform Strouhal number.

3.3 Discussion

Vertically decoupled vortices have not been reported for stratified flow past three-dimensional obstacles. The parameter range in which this behavior exists is relatively unexplored, and difficult to achieve in a laboratory setting, both in terms of the stratification (Vosper et al., 1999) and the rotation (Raja, 2018). Experiments in the stratified and rotating regime have typically been limited to a small, finite number of inertial periods, corresponding to few

Strouhal periods (Codiga, 1993). This may not be a long enough time for the vortex tilting to produce truly decoupled vortices, as startup effects in the simulations often produced several shedding periods of vertically uniform shedding before the vortices began to decouple. We speculate that these reasons, along with low Reynolds number effects, may be the reason that stratified flow past mountains has tended to produce coupled vortices in a laboratory setting (e.g., Hunt and Snyder, 1980; Brighton, 1978).

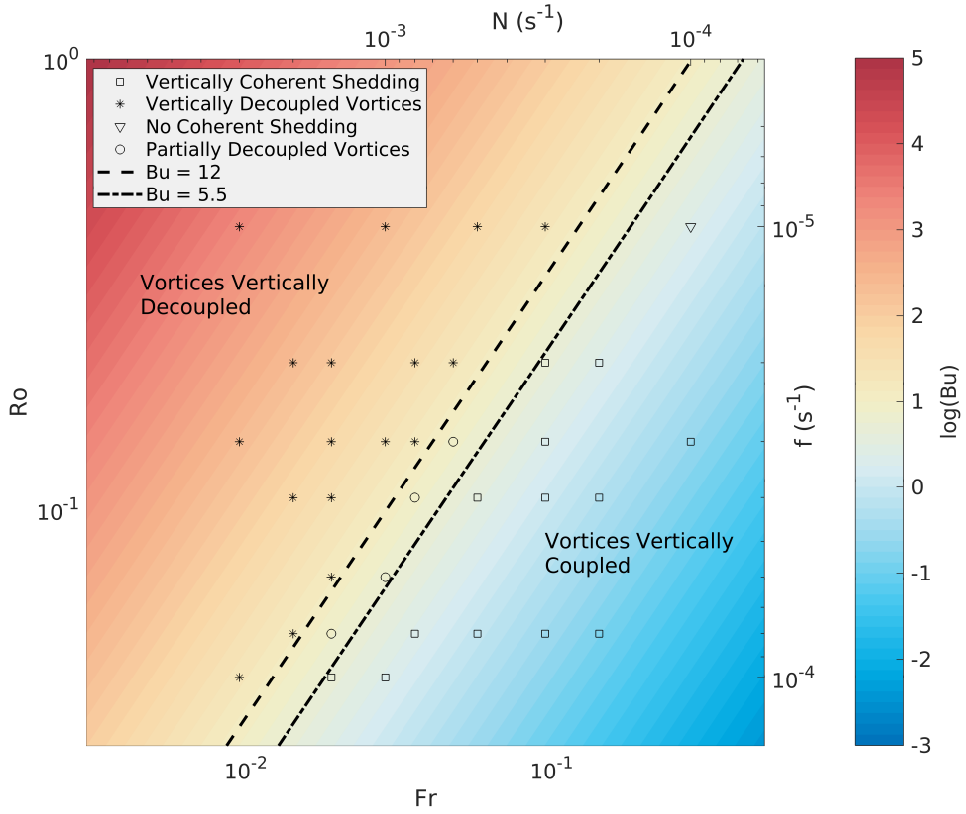

Figure 3.6: A summary of the simulations, with the regime of vortex shedding indicated as follows: vertically uniform shedding is indicated by squares, vertically decoupled shedding is indicated by stars, and the transitional regime is indicated by circles. The triangle symbol (top right) is a case where coherent vortices never formed. The interface between uniform and decoupled shedding is indicated by lines of constant Burger number.

The 35 simulations that were carried out have been plotted in the rotation-stratification parameter space in Figure 3.6. The decoupled shedding regime is characterized by weak

rotation and strong stratification (high Ro and low Fr), and the coupled shedding regime exists where rotation is strong and stratification is weak (low Ro and high Fr). A proposed mechanism to predict vertically decoupled vortices is in terms of a critical Burger number, where the Burger number is defined by $\mathrm{Bu} \equiv \left(\frac{\mathrm{Ro}}{\mathrm{Fr}}\right)^2$ The transitional regime appears to lie in the range,

$$5.5 < \mathrm{Bu}_{\mathrm{crit}} < 12. \tag{3.3}$$

The Burger number is understood to have dynamical importance in distinguishing barotropic and baroclinic dynamics, where a larger Burger number is associated with barotropic flow (e.g., stronger stratification discourages the perturbation of isopycnals) (Boutov et al., 2010). Another interpretation of this finding is that the Burger number scales as

$$\mathrm{Bu} \propto \left(\frac{R_d}{D}\right)^2, \tag{3.4}$$

where R_d is the first baroclinic Rossby radius of deformation, defined as $R_d \equiv \frac{NH}{\pi f}$ (Gill, 1982). Here H is the water depth for a uniformly stratified ocean. Dritschel and De La Torre Juárez (1996) suggest that the appropriate vertical length scale is the vertical extent of the eddies, which would mean that the controlling parameter would be

$$\left(\frac{R_d}{D}\frac{H}{L}\right)^2, \tag{3.5}$$

where H is the total seamount height and L is the total ocean depth. For the simulations conducted here, $\frac{H_{\mathrm{seamount}}}{H_{\mathrm{depth}}}$ is held constant and it is of order 1, so we are not able to distinguish between the cases described by Eq. 3.4 and Eq. 3.5. However, our convergence tests suggest that Eq. 3.5 is the appropriate scaling, in line with Dritschel and De La Torre Juárez (1996). The critical Burger number is achieved when R_d surpasses the horizontal length scale of the seamount. If the horizontal length scale is taken to be $D/2$ to correspond to the deformation radius, then the critical Burger number is predicted to be

$$\mathrm{Bu}_{\mathrm{crit}} = \left(\frac{\pi}{2}\right)^2 \approx 2.5. \tag{3.6}$$

The critical Burger number predicted from Equation 3.6 is somewhat smaller than the transitional Burger number identified in Equation 3.3 from the simulations conducted here, but

it is likely influenced by a number of factors. The predicted $\mathrm{Bu}_{\mathrm{crit}}$ is based on Gill's definition of R_D, and its comparison to the seamount radius (which is related to the vortex radius); other analyses have compared R_D to the vortex diameter (Dritschel et al., 1999) and used a definition for R_D that differs by a factor of π (Stegner and Dritschel, 2000; Dong et al., 2007). The predicted critical Burger number is therefore sensitive to different interpretations of R_D and the choice of horizontal length scale. Secondary effects include the Gaussian shape of the seamount and the influence of the bottom boundary layer. Higher mode baroclinic Rossby numbers may also play a role in the transition process, but the transition onset appears to be dictated by the first mode. The Burger number associated with the n^{th} baroclinic Rossby radius scales as n^2, and so leading order influence of the second mode would imply a wider range of critical Burger number than is observed. Dritschel et al. (1999), in a numerical study of idealized vortices in rotating, stratified flow, report a shift in vortex dynamics at around $\mathrm{Bu} = 4$. The vortices were found to be subject to the "tall column instability" at large Bu, causing the breakdown of 2-D dynamics.

Previous studies have shown that the horizontal extent of eddies in stratified rotating flow scales with the minimum of R_d and D, and that behavior is also observed in the present study (Stegner and Dritschel, 2000; Dong et al., 2007). When $R_d < D$, the eddies are driven by a geostrophic balance and the dynamics are characterized by baroclinic flow (Boutov et al., 2010). Conversely, when $D < R_d$, the eddies lose geostrophic balance and behave in a manner more consistent with a classical barotropic wake. The horizontal extent of the eddies now scales with the local diameter of the seamount, and the shedding frequency is characterized by a constant Strouhal number. This effect is demonstrated in Figure 3.7.

3.4 Conclusions

We have documented a novel vortex shedding regime for rotating, stratified flow past a seamount using a ROMS model. In this regime, coherent vortices form and advect in a manner such that the different vertical levels do not affect one another. The transition from geostrophic, vertically-coupled coherent vortices to an ageostrophic, uncoupled regime

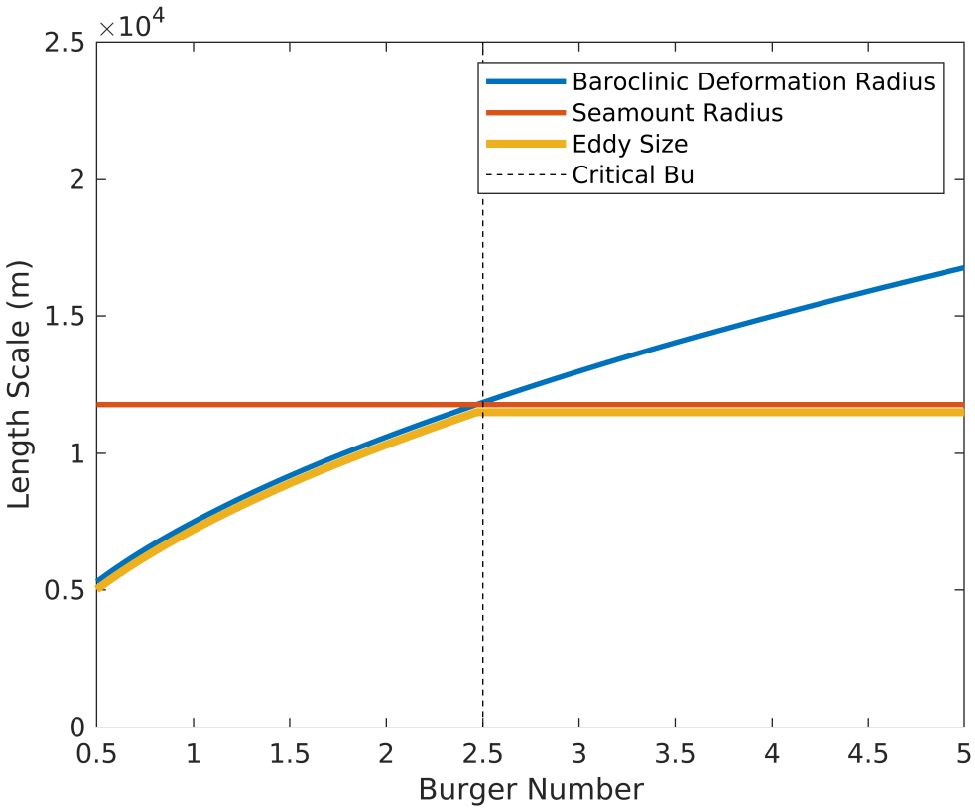

Figure 3.7: At low Burger number (RHS of the plot), $\frac{D}{2} > R_D$, and the vortices are coupled. Consequently, the eddies scale with R_D. At large Burger number, R_D becomes large, and the vortices decouple. Their horizontal length scale is approximately that of the seamount.

is well-predicted by a critical Burger number. The physical interpretation of this finding is that when the baroclinic deformation radius exceeds the horizontal extent of the seamount, the flow tends to become barotropic, which permits a more classical 2-D wake structure to form. Once the eddies are not constrained by rotational effects, the shedding frequency adjusts to produce a constant Strouhal number at all depths.

The vertically decoupled shedding regime may have important implications for the energetics of seamount interaction with currents, because the visually remarkable transition is accompanied by changes in the vortex size and vertical strain. Furthermore, Dong et al. (2007) and Stegner and Dritschel (2000) suggest that an important transition in the 2-D

stability and energetics of nearly geostrophic vortices is associated with $\frac{\mathrm{Bu}}{\mathrm{Ro}}$, rather than Bu. A detailed energy analysis of the vertically decoupled vortex shedding mode may provide insight into the relative energetic importance of the decoupling versus the loss of 2-D stability.

Chapter 4

WAKE ENERGETICS

The energetic aspects of seamount wakes are discussed in this chapter. There exists a gulf in understanding between the physical processes that can occur in the wake and the overall energetic impact of seamounts. We work towards bridging this gap by analyzing the energetic aspects of the simulations described in Chapter 2. The kinetic energy within the domain is decomposed into the mean kinetic energy, unsteady eddy energy, and turbulent kinetic energy; evolution equations are derived for each. Within the evolution equations, energy exchange terms arise, which relate the various forms of kinetic energy, the potential energy, and the viscous dissipation. Key exchange terms, such as the rate at which the mean flow is converted into eddy energy, are compared across the Froude-Rossby parameter space. It is shown that the conversion terms associated with mesoscale motions are a function of the Burger number, which is consistent with a quasigeostrophic flow regime. Conversely, conversion terms associated with turbulent processes scale with the product of the Froude and Rossby number. The amount of energy extracted from the mean flow suggests that wake effects may be significant for the parameter range and model assumptions studied. These results suggest that some seamounts may indeed function as "stirring rods."

In Section 4.2, we derive a formalism in order to separately describe the energetics associated with the mean flow, the unsteady eddy-scale flow, and the subgridscale modeled turbulence. The resulting equations yield a set of energy exchange terms that represent important physical processes within the flow. This framework is then applied in Sections 4.3.1 and 4.3.2, which separately describe the various energy reservoirs, and the rate of energy transfer between them. We identify the terms that determine the leading-order dynamics within the domain, and analyze their behavior within the Froude-Rossby parameter space in

Section 4.4. Implications for ocean mixing are discussed in Section 4.5, followed by concluding remarks. The work discussed in this chapter is also available as Perfect et al. (2019a).

4.1 Background

Recently, there has been increased scientific interest in the eddy kinetic energy that islands and seamounts might extract from the barotropic flow (Gula et al., 2016; Dong et al., 2018). While the research interest is relatively recent, the hypothesis that seamounts might function as "stirring rods" has been around for decades (Munk and Wunsch, 1998). A natural question, then, is whether the flux of energy into the seamount wake is energetically significant compared to the flux into the internal gravity waves, and how that might change due to the Coriolis acceleration and ocean stratification. In order to effectively answer this question it is necessary to develop a framework to understand the energetics of the seamount wake.

The suggestion that seamounts might serve as stirring rods is strengthened by the recent observations of abyssal seamount-generated eddies (Chen et al., 2015). Additionally, field studies aimed at mapping diapycnal diffusivity note enhanced mixing associated with topography and sloping boundaries (e.g., Toole et al., 1997; Naveira Garabato et al., 2011; Kunze et al., 2012). Brighton (1978) and Vosper et al. (1999) report vigorous vortex shedding for 3D obstacles in strongly stratified flow in a laboratory, a result with obvious parallels to a large seamount in an ocean current. These two studies also served as experimental confirmation that when the obstacle's height significantly exceeds the vertical length scale set by the stratification (i.e., $\frac{U}{N}$, where U and N are the ambient current speed and buoyancy frequency, respectively), the flow predominantly moves around rather than over, and is mostly confined to horizontal planes (e.g., Riley et al., 1976). It is this tendency for the flow to contour around the obstacle that is responsible for the flow separation that enables eddy generation. A shortcoming of all of these studies is that they lacked a Coriolis acceleration, which is a critical aspect of the seamount wake problem. It is possible to model flow past a seamount with stratification and rotation using a rotating table (e.g., Boyer and Chen, 1987; Codiga, 1993), but experiments become increasingly difficult to conduct as the stratification

and rotation increase. A state-of-the-art 10-m rotating table was recently used to evaluate the internal waves produced by an isolated seamount in an unprecedented parameter space of low Froude and Rossby number (Raja, 2018). Vortex shedding was also observed, but only treated qualitatively because the focus of the study was on internal wave generation.

Numerical modeling offers an opportunity for a more quantitative investigation into seamount wakes; regional models have proven to be effective methods of reproducing observed flow patterns near real topography (Beckmann and Haidvogel, 1997; Coutis and Middleton, 2002; Dong and McWilliams, 2007; Boutov et al., 2010). Traditionally, these models have been used within the context of understanding the hydrodynamics of a specific site, but they have the potential to offer more insight into the underlying physics when used with idealized settings. Idealized regional models for flow past a mountain have been popular within the atmospheric sciences community, though typically the effect of stratification is much weaker than in the ocean and the Coriolis acceleration is usually neglected (e.g., Smolarkiewicz and Rotunno, 1989; Schär and Smith, 1993a; Schär and Durran, 1997; Epifanio and Rotunno, 2005). Notably, Bauer et al. (2000) performed a series of idealized simulations, much in the same way as the present paper, except the parameters of interest were the Froude number and the aspect ratio of the mountain. More recently, Perfect et al. (2018) performed a series of simulations of an idealized seamount for a variety of stratification and rotation conditions. These simulations demonstrate that the seamount wake pattern exhibits different regimes, depending on the Froude and Rossby number. A similar set of wake regimes can be seen in simulations by Srinivasan et al. (2019). While Srinivasan et al. (2019) explores a similar Froude number regime, the Rossby number is held constant and the seamount is much less steep and shorter relative to the bottom boundary layer height compared to the present simulations.

In order to relate the simulations described in Chapter 2 back to the broader question of whether seamounts can act as stirring rods, we perform an energy analysis on a subset of the simulation results. Because it is imperative to have identical turbulence models across the simulations here, only the 18 simulations noted in Figure 4.1 are used. The relative positions

of these simulations in the Fr-Ro parameter space with respect to the shedding regimes are also noted. MacCready et al. (2009) demonstrate how simulation output, along with a set of energy equations, can be used to trace the conversion of energy between different forms. For the present analysis, we closely follow the methodology of Kang and Curchitser (2015), which partitions the kinetic and potential energy into mean and eddy components and computes conversion terms between them. We extend Kang's treatment to include a turbulent scale in addition to the mean and eddy components. This extension allows for energy pathways to be traced from the barotropic inflow to mixing and dissipation, which are vital quantities when discussing the role of seamounts in a global energy balance. Of particular importance is how oceanography-relevant terms such as the diapycnal flux, the rate of eddy generation, and the internal wave flux might be parameterized.

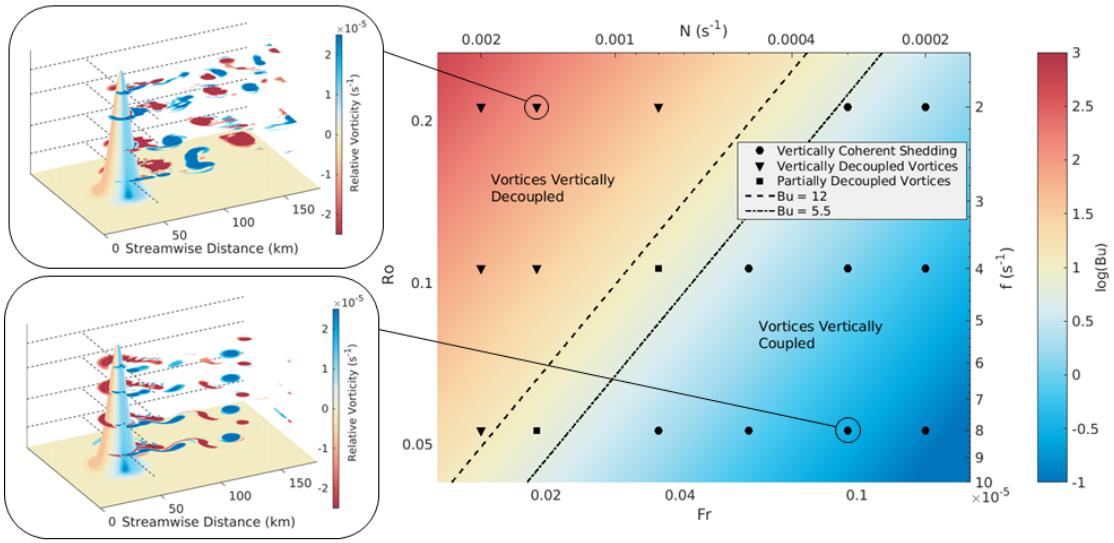

Figure 4.1: Different shedding regimes are observed, determined by the Burger number of the associated simulation. At sufficiently high Bu, vortices become vertically incoherent, resulting in the "decoupled" shedding regime (top left). Vertically coherent vortex shedding (bottom right) is characteristic of wakes in other vortex shedding literature.

4.2 *Equations of Motion*

The present simulations have a uniform inflow of kinetic energy, which is then transformed, by interaction with the bathymetry, into eddies, internal waves, turbulence, and related potential energy. In order to trace the pathways between these forms of energy, we derive a set of energy equations that include exchange terms between each other. These relationships are presented schematically in Figure 4.2.

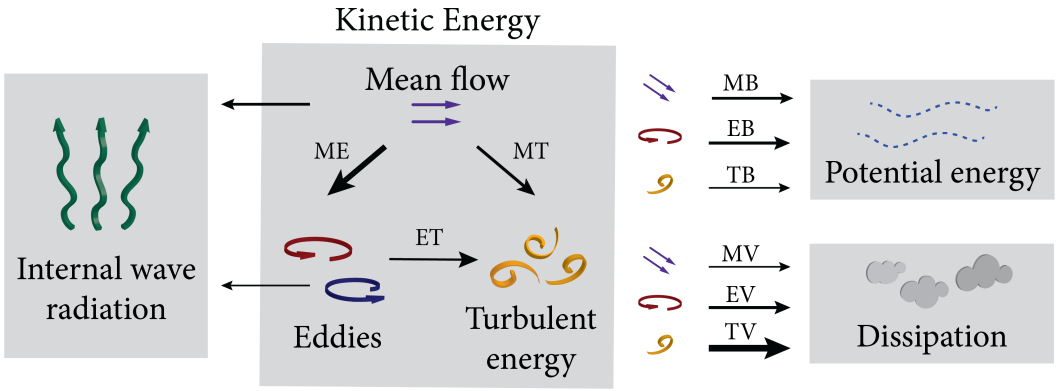

Figure 4.2: Qualitative view of the different energy transfer terms. The mean, eddy, and turbulent kinetic energy each have exchange terms with each other. Meanwhile, each scale of kinetic energy interacts with potential energy and dissipation. The mean flow can produce steady lee waves that radiate out of the domain, and the unsteady wake may also produce internal wave radiation.

The unsteady RANS structure of ROMS suggests that a 3-tiered velocity decomposition (mean, eddy, and turbulent) would well-represent the physical processes of a seamount wake (see Phillips (1966) or Hussain and Reynolds (1970) for a previous 3-tiered decomposition.) The model output can be easily decomposed into a time mean and a fluctuating eddy component, as in Kang et al. (2016). However, the unresolved turbulent motion still interacts with the resolved motions in a meaningful way that is also distinct from the eddy

component. Therefore, we also include an evolution equation for the turbulent fluctuations, which yields exchange terms that may be calculated from ROMS output, even though the turbulent scale is not directly resolved in the simulations. The mathematical structure of the following section could also be applied to another scenario of interest– the case where tides are included. A phase average over the tidal period could be used in place of the time average. The output from the equations of motion could then be partitioned into the unsteady phase-averaged ocean currents, the wake eddying motions occurring within each tidal phase, and the turbulence. Such simulations and analyses are possible, but require significantly more computational resources and analysis. Because of the relevance of the problem with a steady, non-tidal flow, the more complex tidal problem is left for future work.

4.2.1 Definition of Velocity Decomposition

Consider a 3-part variable decomposition, constructed from two separate averaging operations: $\langle(\cdot)\rangle$, the traditional ensemble, Reynolds, or probability average used in turbulence modeling, which in this case can be considered to be a time average over a time on the order of the numerical time-step, and $\bar{(\cdot)}$, a time average over a time much greater than that of the large-scale unsteady motions. The use of two distinct averages originates from Hussain and Reynolds (1970), which utilized a phase average and a time average for wave disturbances in turbulent shear flows. Though mathematically equivalent, the treatment that follows is designed to explore the exchange between the different scales of the flow– the mean flow, the unsteady flow that is resolved by the grid, and the subgrid-scale modeled turbulence. Consequently, the equations of motion can be written for field variables at three timescales: the mean flow, the eddy scale, and the turbulent scale.

In the context of modeled flow past a seamount, take u_i to be the total velocity of the flow, $U_i = \langle u_i \rangle$ to represent the Reynolds-averaged velocity, that is, the output of the ROMS code which includes a RANS model, and u_i' to represent the turbulent velocity that is averaged out by the Reynolds averaging. Then $u_i = U_i + u_i'$. U_i may be further decomposed into a time average over many Strouhal periods, $\bar{U}_i$, and the unsteady eddy scale motion, $\hat{u}_i$, such

that $U_i = \bar{U}_i + \hat{u}_i$. The motion at these three scales must sum to the total velocity, u_i, so

$$u_i = U_i + u_i' = \bar{U}_i + \hat{u}_i + u_i' \,. \tag{4.1}$$

The same decomposition holds for all field variables, including the reduced pressure, $\phi = \frac{p}{\rho_0}$ and the buoyancy $b = g\frac{\rho - \rho_0}{\rho_0}$ (where ρ_0 is the fixed Boussinesq density):

$$\begin{aligned} b &= B + b' = \bar{B} + \hat{b} + b' \\ \phi &= \Phi + \phi' = \bar{\Phi} + \hat{\phi} + \phi' \end{aligned} \tag{4.2}$$

4.2.2 Derivation of the Momentum Equations

Here we develop the equations for $\bar{U}_i$, $\hat{u}_i$, and u_i', which will be used to derive the energy equations for the time-averaged flow, for the unsteady wake, and for the turbulence. We start with the Navier-Stokes equations subject to the Boussinesq approximation for a rotating, stratified fluid, represented as:

$$\frac{\partial u_i}{\partial t} + u_j \frac{\partial u_i}{\partial x_j} = -\frac{\partial \phi}{\partial x_i} + 2\nu \frac{\partial s_{ij}}{\partial x_j} - 2\epsilon_{ijk}\Omega_j u_k - b\,\delta_{i3}, \tag{4.3}$$

where $2\boldsymbol{\Omega} \times \mathbf{U} = 2\epsilon_{kij}\Omega_j u_k$ is the Coriolis force. The rotation vector, $\boldsymbol{\Omega}$, can vary in general, but for this application we assume that $2\boldsymbol{\Omega} = f\hat{\mathbf{z}}$, where f is the constant planetary vorticity. We have also defined the strain rate $s_{ij} \equiv \frac{1}{2}\left(\frac{\partial u_i}{\partial x_j} + \frac{\partial u_j}{\partial x_i}\right)$.

The equation for U_i can be obtained by Reynolds-averaging Eq. 4.3, giving:

$$\frac{\partial U_i}{\partial t} + U_j \frac{\partial U_i}{\partial x_j} = -\frac{\partial \Phi}{\partial x_i} + 2\nu \frac{\partial S_{ij}}{\partial x_j} - 2\epsilon_{ijk}\Omega_j U_k - B\delta_{i3} - \frac{\partial R_{ij}}{\partial x_j}, \tag{4.4}$$

where $R_{ij} = \langle u_i' u_j' \rangle$ is the Reynolds stress. Next, writing Eq. 4.3 using the Reynolds decomposition $u_i = U_i + u_i'$, and then subtracting Eq. 4.4 from the result gives the equation for u_i':

$$\frac{\partial u_i'}{\partial t} + \underbrace{U_j \frac{\partial u_i'}{\partial x_j}}_{5,6} = -\frac{\partial}{\partial x_j}\left(\phi'\delta_{ij} + \underbrace{u_i' u_j'}_{7} - 2\nu s_{ij}' - R_{ij}\right) - \underbrace{u_j' \frac{\partial U_i}{\partial x_j}}_{8,9} - 2\epsilon_{ijk}\Omega_j u_k' - b'\delta_{i3} \tag{4.5}$$

The equation for $\bar{U}_i$ can be obtained by time-averaging Eq. 4.4, giving:

$$\underbrace{\frac{\partial \bar{U}_i}{\partial t}}_{=0} + \underbrace{\bar{U}_j \frac{\partial \bar{U}_i}{\partial x_j}}_{1} = -\frac{\partial}{\partial x_j}\left(\bar{\Phi}\delta_{ij} - 2\nu\bar{S}_{ij} + \bar{R}_{ij} + \bar{T}_{ij}\right) - 2\epsilon_{ijk}\Omega_j\bar{U}_k - \bar{B}\delta_{i3} \tag{4.6}$$

Here it has been convenient to define the eddy component of the Reynolds stress as $T_{ij} = \hat{u}_i\hat{u}_j$, and then decompose both R_{ij} and T_{ij} in terms of time-averaging as:

$$R_{ij} = \bar{R}_{ij} + \hat{R}_{ij} \qquad T_{ij} = \bar{T}_{ij} + \hat{T}_{ij} \tag{4.7}$$

Finally, writing Eq. 4.4 in terms of the decomposition $U_i = \bar{U}_i + \hat{u}_i$, and then subtracting Eq. 4.6 gives the equation for $\hat{u}_i$:

$$\frac{\partial \hat{u}_i}{\partial t} + \underbrace{\bar{U}_j \frac{\partial \hat{u}_i}{\partial x_j}}_{2} = -\frac{\partial}{\partial x_j}\left(\underbrace{\hat{u}_i\hat{u}_j}_{3} + \hat{\phi}\delta_{ij} - 2\nu\hat{s}_{ij} + \hat{R}_{ij} - \bar{T}_{ij}\right) - \underbrace{\hat{u}_j \frac{\partial \bar{U}_i}{\partial x_j}}_{4} - 2\epsilon_{ijk}\Omega_j\hat{u}_k - \hat{b}\delta_{i3} \tag{4.8}$$

Note that the original Equation 4.3 can be recovered by summing the above three equations. The decompositions in b, ϕ, s_{ij}, and the time and rotation terms are recovered trivially. The nine advective acceleration terms originating from the triple decomposition have been indicated with underbrace numbering and, when summed together, they are equal to the original advection term $u_j\frac{\partial u_i}{\partial x_j}$. The Reynolds stress terms cancel, using Equation 4.7. Therefore, this trio of equations represents the momentum equation, decomposed into equations for the three components of motion that we are considering.

4.2.3 Derivation of the Energy Equations

To obtain the energy equations for these three components of the motion, we multiply the equation in $\bar{U}_i$ with $\bar{U}_i$, the equation in $\hat{u}_i$ with $\hat{u}_i$, and the equation in u_i' with u_i'. Then, to obtain the overall energy exchanges, the equations are volume-integrated and time-averaged, producing a balance between surface flux terms and volumetric energy conversion terms. These conservation equations are as follows:

Mean flow kinetic energy (MKE):

$$\int_{\mathcal{S}}\left(\frac{1}{2}\bar{U}_j\bar{U}_i^2+\bar{\Phi}\bar{U}_j-2\nu\bar{U}_i\bar{S}_{ij}+\bar{U}_i\bar{R}_{ij}+\bar{U}_i\bar{T}_{ij}\right)n_j d\mathcal{S}=\int_{\mathcal{V}}\left\{\underbrace{\bar{R}_{ij}\frac{\partial\bar{U}_i}{\partial x_j}}_{-MT}+\underbrace{\bar{T}_{ij}\frac{\partial\bar{U}_i}{\partial x_j}}_{-ME}-\underbrace{2\nu\bar{S}_{ij}\bar{S}_{ij}}_{MV}-\underbrace{\bar{B}\bar{U}_3}_{MB}\right\}d\mathcal{V}. \tag{4.9}$$

Eddy flow kinetic energy (EKE):

$$\int_{\mathcal{S}}\left(\frac{1}{2}\overline{U_j\hat{u}_i^2}+\overline{\hat{\phi}\hat{u}_j}-2\nu\overline{\hat{u}_i\hat{s}_{ij}}+\overline{\hat{u}_i\hat{R}_{ij}}\right)n_j d\mathcal{S}=\int_{\mathcal{V}}\left\{\underbrace{-\bar{T}_{ij}\frac{\partial\bar{U}_i}{\partial x_j}}_{-ME}+\underbrace{\overline{\hat{R}_{ij}\frac{\partial\hat{u}_i}{\partial x_j}}}_{-ET}-\underbrace{2\nu\overline{\hat{s}_{ij}\hat{s}_{ij}}}_{EV}-\underbrace{\overline{\hat{b}\hat{u}_3}}_{EB}\right\}d\mathcal{V}\,. \tag{4.10}$$

Turbulent kinetic energy (TKE):

$$\int_{\mathcal{S}}\left(\overline{U_j k}+\overline{\langle\phi' u_j'\rangle}-2\nu\overline{\langle u_i' s_{ij}'\rangle}+\frac{1}{2}\overline{\langle u_j' u_i'^2\rangle}\right)n_j d\mathcal{S}=\int_{\mathcal{V}}\left\{\underbrace{-\bar{R}_{ij}\frac{\partial\bar{U}_i}{\partial x_j}}_{-MT}-\underbrace{\overline{\hat{R}_{ij}\frac{\partial\hat{u}_i}{\partial x_j}}}_{-ET}-\underbrace{2\nu\overline{\langle s_{ij}' s_{ij}'\rangle}}_{TV}-\underbrace{\overline{\langle b' u_3'\rangle}}_{TB}\right\}d\mathcal{V}\,. \tag{4.11}$$

Here the turbulent kinetic energy per unit mass is: $k=\frac{1}{2}\langle u_i^2\rangle$. The divergence theorem has been used to evaluate all terms on the left-hand sides. In addition, each of the velocities is taken to be incompressible, and, finally, the viscous terms are evaluated as (see Kundu et al., 2004),

$$2\nu u_i'\frac{\partial s_{ij}'}{\partial x_j}=2\nu\frac{\partial(u_i' s_{ij}')}{\partial x_j}-2\nu s_{ij}' s_{ij}'\,. \tag{4.12}$$

In the right hand side of Equations 4.9-4.11, every term represents either viscous dissipation, buoyant exchange with potential energy, or an exchange with one of the other energy components. Each term is labeled according to the forms of energy that are being exchanged: M is MKE, E is EKE, T is TKE, V is viscous dissipation, and B is potential energy (buoyancy). "MB," for example, describes the rate of energy conversion from the mean flow into potential energy. ME, MT, and ET each appear twice in the above equations; because they represent exchange processes among the different scales of kinetic energy, they appear as

conjugate pairs that do not alter the total kinetic energy. All of the labeled terms are active throughout the domain, and their role is sketched in Figure 4.2. The left hand side terms are accounted as energy fluxes through and rates of work at the domain boundaries. The first term on the left-hand side of each of the above equations pertains to the advective flux of kinetic energy at the scale of interest. The second term pertains to pressure work and internal wave radiation. The third term is the viscous work being done at the boundary of the domain. The fourth term in Eq. 4.11 is flow of turbulent kinetic energy through the domain surfaces due to the turbulence. The remaining left hand side terms do not have well-established physical interpretations.

4.3 Results

The decompositions defined by Equations 4.1 and 4.2 are applied to the field variables in the output of the 18 simulations outlined in Fig. 4.1. Then, the energy conversion terms in Equations 4.9-4.11 are computed. In order to mitigate any spurious boundary effects, the volume over which the conversion terms are analyzed sits fully within the horizontal boundaries of the computational domain. The outer 10km (30 cells) of the sides (North and South in the model), 13.3 km (40 cells) of the inlet, and 33.3 km (100 cells) of the outlet are excluded. The seamount itself, as well as any upstream effects of the seamount are included in the analysis domain. Below we present the time-averaged, volume-integrated energy reservoir and energy conversion results for the array of simulations outlined in Figure 4.1.

4.3.1 Reservoir Term Evaluation

Neglecting thermal energy produced by dissipation, the energy within the domain exists as either kinetic or potential energy. The kinetic energy may be further partitioned using Equations 4.9-4.11 into the mean kinetic energy (MKE), eddy kinetic energy (EKE), and turbulent kinetic energy (TKE). The potential energy quantity of interest is the available potential energy (APE); this quantity is not decomposed like the kinetic energy, but treated

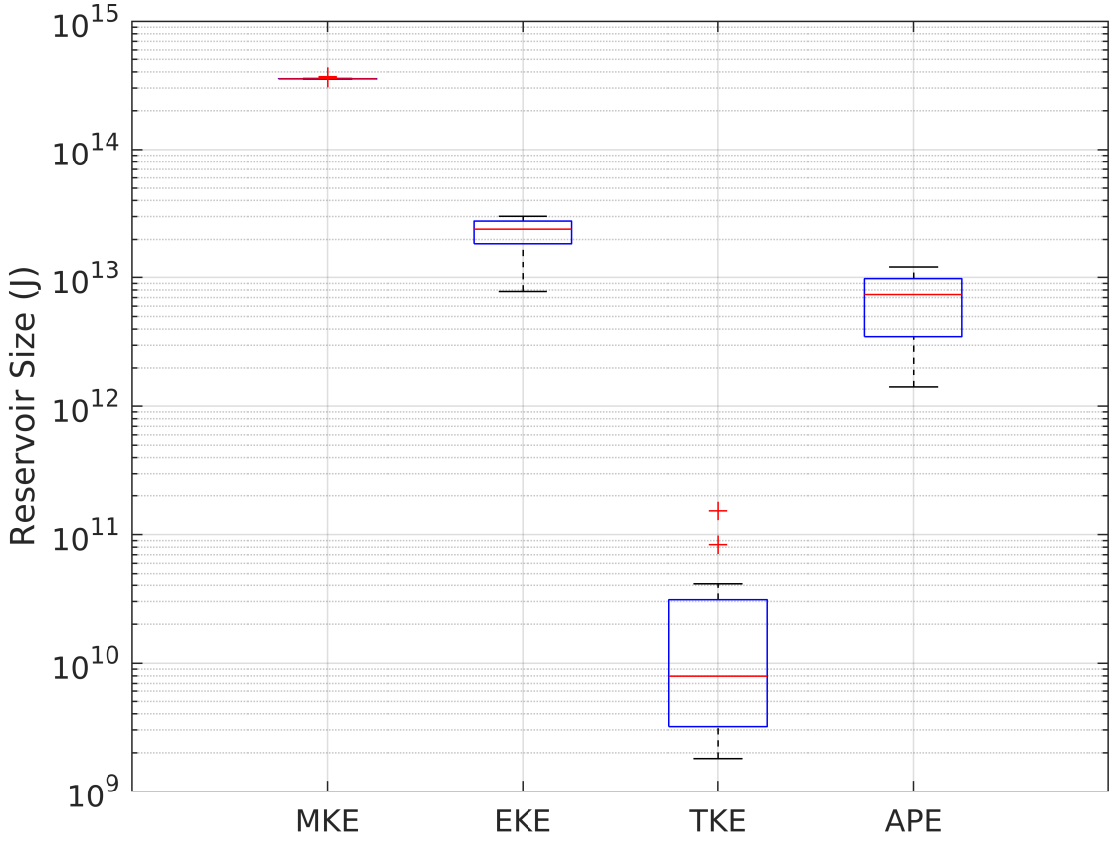

Figure 4.3: Energy reservoirs are divided into mean kinetic energy, eddy kinetic energy, turbulent kinetic energy, and available potential energy. Each quantity is represented as a boxplot of the results of the 18 simulations.

as a single value. The kinetic energies are computed as volume-integrated time series:

$$\mathrm{MKE}(t) = \int_{\mathcal{V}} \rho_0 \frac{1}{2} \bar{U}_i(\vec{x},t)\bar{U}_i(\vec{x},t)d\mathcal{V} \tag{4.13}$$

$$\mathrm{EKE}(t) = \int_{\mathcal{V}} \rho_0 \frac{1}{2} \hat{u}_i(\vec{x},t)\hat{u}_i(\vec{x},t)d\mathcal{V} \tag{4.14}$$

$$\mathrm{TKE}(t) = \int_{\mathcal{V}} \rho_0 (k(\vec{x},t))d\mathcal{V}. \tag{4.15}$$

Because the specific turbulent kinetic energy (k) is directly output from ROMS, we integrate this quantity directly rather than from the turbulent velocities, which are not computed.

The APE is computed via the sorting method established by Winters et al. (1995). It should be noted that, because the analysis domain contains an inflow and outflow, the time series for the APE does not evolve as for a closed system. Fluctuations in APE may be due to baroclinic processes and irreversible mixing, but also boundary fluxes.

Each time series for an energy reservoir tends to oscillate about a mean, which is reported as a bulk value for each simulation. In figure 4.3 the range of bulk reservoir values over all simulations are compiled in the form of a boxplot for each energy reservoir. Each boxplot, then, contains a dataset of 18 time-averaged reservoir values. The middle two quartiles of the data fall within the box, whose central line is the median, and the non-outlier extremes are indicated by the bars above and below the box. Outliers are displayed as individual red markers. Because the majority of the flow within the domain is unperturbed by the seamount, most of the energy exists as MKE, and there is very little inter-simulation variability for this reservoir. The EKE and APE contain similar amounts of energy, approaching 10% of the MKE, with the EKE containing slightly more. The TKE is several orders of magnitude below; the energy-containing submesoscale motions are largely resolved by the simulation, and thus do not need to be modeled with the turbulence. We note that there is approximately a decade of variability in the APE and EKE between simulations, and the TKE contains nearly two decades of variability. These inter-simulation differences will be discussed in detail in Section 4.4.1.

4.3.2 Conversion Term Evaluation

The volumetric terms labeled in Equations 4.9-4.11 represent rates of conversion between different forms of energy– the exchange terms (ME, MT, ET) transmit energy between the scales of motion, the buoyancy terms (MB, EB, TB) represent the rate of production of potential energy through buoyancy, and the viscous terms (MV, EV, TV) represent the rate of viscous losses and turbulent dissipation. While the viscous terms all describe losses within the context of the numerical model, it should be noted that MV and EV physically represent the effect of an eddy viscosity, ν_N. These terms, in a physical system, would appear as sources

for the turbulence rather than as viscous losses. Each of the conversion terms describe above exhibits complex spatial and temporal patterns, which might be related to the emergence of various fluid instabilities (as studied by Dong et al., 2007; Srinivasan et al., 2019), but such a treatment is beyond the scope of this work. For the current study, we restrict our analysis to the volume-integrated, time-averaged conversion terms, and assess the aggregate spatial distribution between the bottom boundary layer (BBL) and the free stream. The intent here is to relate the bulk energetic quantities of interest to the underlying control parameters and establish useful relationships for future parameterization. It is necessary to separate out the BBL because for many terms (e.g., TV, in agreement with MacCready et al. (2009)) nearly all of the conversion is concentrated in the BBL, and these processes are not significantly affected by the presence of the seamount. Each of the terms are therefore split into two components: the BBL contribution, which is defined to be the bottom 100m of the domain, and the free stream contribution, comprising the remainder of the domain.

A summary of the conversion terms is presented in Figure 4.4. Each boxplot represents the distribution of the time-averaged conversion for all simulations, as was done with Fig. 4.3. Each panel contains the volumetric conversion terms that appear in the MKE (Fig. 4.4a), EKE (Fig. 4.4b), and TKE (Fig. 4.4c) equations. Terms are presumed to be net sinks in their respective kinetic energy equation. Terms that act as sources of energy are indicated with a negative on the abscissa label. The exchange terms each appear twice, once as a source, and again as a sink in the conjugate scale of motion. The dominant term in both the mean and eddy equations is ME, representing the massive energy transfer from the mean flow into unsteady vortices. The TKE equation is dominated by the BBL partition of TV, which is numerically consistent with the formulation of MacCready et al. (2009), which finds that TV $\approx \rho_0 C_D |u|^3$. The eddy losses to viscosity and buoyancy (EV and EB) are both significant terms, which will also be discussed in greater detail in Section 4.4.2.

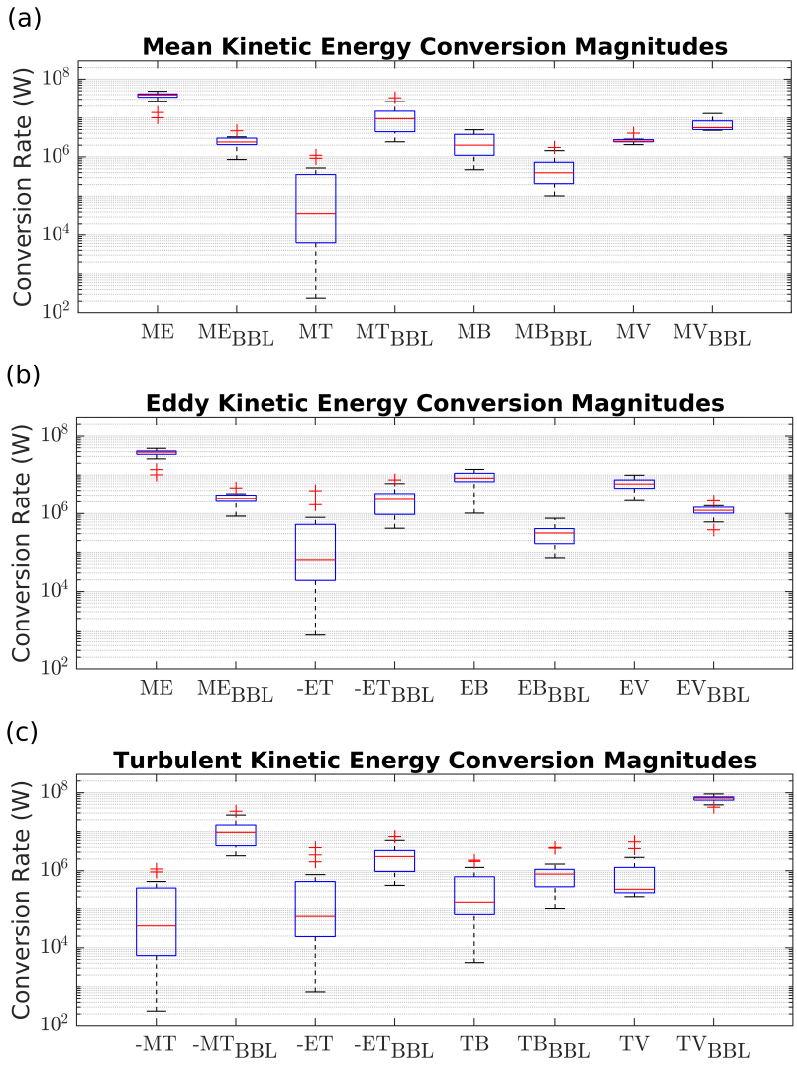

Figure 4.4: The magnitudes of the various energy conversion terms are presented as box-plots of the average values from the 18 simulations. Each conversion term is split into the component that occurs in the boundary layer, and the free stream component.

4.4 Energetics Scaling

It is desirable to evaluate how the energetics terms discussed in the previous section depend on rotation and stratification. Of particular importance, in addition to the reservoir terms, are the most significant pathways by which energy is removed from the mean flow (ME and MT), and removed from the eddy motions (EV and EB). These terms govern the leading-order behavior that describes the stirring and mixing that takes place in the lee of the seamount. While this analysis cannot prescribe a universal parameterization, it can suggest how the effects of rotation and stratification might enter such a parameterization.

4.4.1 Reservoir Term Scaling

The energy reservoirs for each simulation are plotted in Figure 4.5. Symbols represent the time mean of that reservoir for a particular simulation, and the errorbars denote the associated standard deviation of the time series. The different symbols/colors indicate groupings of simulations with the same Coriolis parameter. The EKE data, given in Figure 4.5a, approximately collapse when plotted against the Burger number, $\left(\frac{NH}{fD}\right)^2$. The two strongest stratification cases, for $f = 8 \times 10^{-5}$ s^{-1}, appear to be outliers; otherwise, the EKE grows with Bu until it saturates near $\mathrm{Bu}_{\mathrm{crit}}$ and then remains at a constant maximum value. Here $\mathrm{Bu}_{\mathrm{crit}}$ refers to the Burger number at which the vortex regime shifts from couple to decoupled shedding (see 3.3.) This behavior is due to the eddy size scaling observed by Perfect et al. (2018) and Srinivasan et al. (2019); below $\mathrm{Bu}_{\mathrm{crit}}$, the eddies generally do not exceed R_d, the baroclinic deformation radius, which scales with $\frac{N}{f} \propto \sqrt{\mathrm{Bu}}$. However, above $\mathrm{Bu}_{\mathrm{crit}}$, the eddy length scale is determined by the seamount size, which manifests as an upper bound on eddy size, limiting the growth of EKE for $\mathrm{Bu} > \mathrm{Bu}_{\mathrm{crit}}$. The dashed line indicates a $\mathrm{Bu}^{1/2}$ scaling, which matches well with the data.

Figure 4.5b plots the APE versus the Burger number. Again, the data approximately collapse, in this instance forming a peak near $\mathrm{Bu}_{\mathrm{crit}}$. In its linearized form, the APE scales as the square of the product of the buoyancy frequency and the isopycnal displacement.

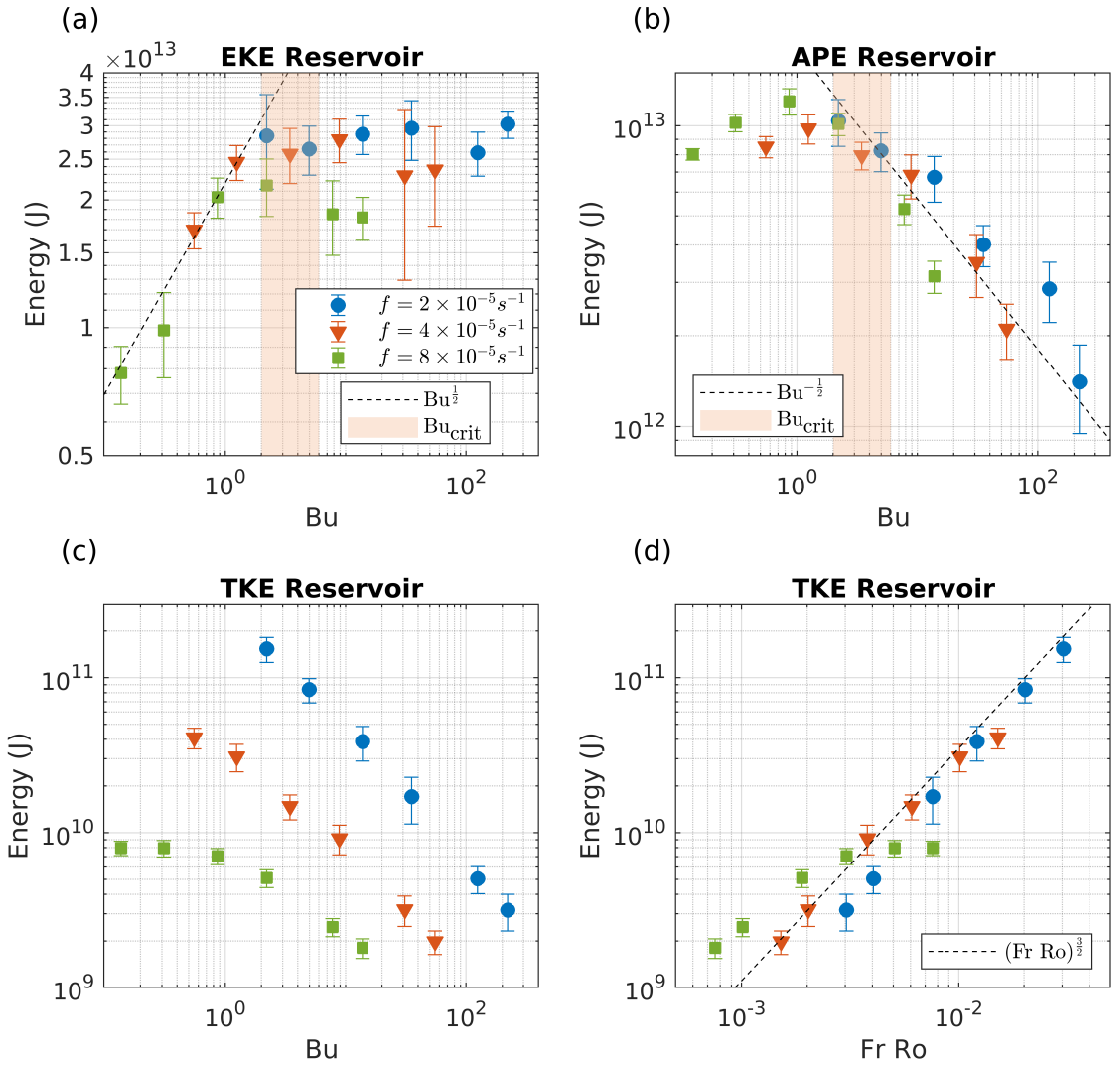

Figure 4.5: Suggested scalings for the EKE (a), APE (b), and TKE (c-d). Each marker corresponds to the time mean of a single simulation, with error bars indicating the standard deviation of the time series. Shaded regions indicate a range for the critical Burger number and dashed lines offer possible scaling relationships as indicated in the legends.

The isopycnal displacement is governed by both the rotation and the stratification; at very high stratification the isopycnal displacement is suppressed. With strong rotation, vertically coherent eddies appear to limit the growth of displacements. We find that the critical Burger number provides the optimum balance between rotation-dominant and stratification-dominant systems; the point where vortices decouple (see Figure 4.1) corresponds to the maximum APE. The falloff in APE at high-Bu scales approximately as $\mathrm{Bu}^{-1/2}$, or equivalently, $\frac{f}{N}$.

The TKE, in contrast with the EKE and APE, scales poorly with Bu, as demonstrated in Fig. 4.5c). When plotted against Fr Ro as in Fig. 4.5d, however, the three lines at various rotation values collapse. The collapsed data suggest that the TKE reservoir scales like $(\mathrm{Fr\ Ro})^{\frac{3}{2}}$. This relationship seems to be robust across most of the parameter space, except possibly for very low Burger number. Unlike the EKE and APE, the TKE scaling does not change significantly near $\mathrm{Bu}_{\mathrm{crit}}$. This result is consistent with the well-known result that both rotation and stratification act to suppress 3D turbulence (Praud et al., 2006). The TKE is therefore approximately independent of the eddy structure, and appears to have no memory of the geometry of the seamount. Rather, the TKE is determined by the more fundamental properties of geophysical turbulence. An alternate interpretation of the Fr Ro scaling is possible if the Froude number is redefined in terms of a bulk Richardson number, $\mathrm{Ri} = (N/(U/H))^2$. Consider $\frac{U}{H}$ to be a measure of the bulk shear caused by the seamount. Then,

$$\mathrm{Fr} = \frac{U/H}{N} = \mathrm{Ri}^{-\frac{1}{2}}, \tag{4.16}$$

and

$$\mathrm{Fr\ Ro} = \mathrm{Fr}^2 \frac{\mathrm{Ro}}{\mathrm{Fr}} = \mathrm{Ri}^{-1}\mathrm{Bu}^{\frac{1}{2}}. \tag{4.17}$$

This relationship establishes a Burger number dependence for the TKE, but also indicates that the TKE depends on the inverse Richardson number. With increased stratification, the bulk Richardson number is increased, which reduces turbulence generated from flow shear.

4.4.2 Conversion Term Scaling

All of the conversion terms in Figure 4.4 are plotted in Figures 4.6-4.9. Figures 4.6 and 4.8 scale all conversion terms versus the Burger number for the free stream and bottom boundary layer components, respectively. In Figures 4.7 and 4.9, the conversion terms are plotted against suggested scalings, which were determined by trial and error. When no adequate scaling is found, the Burger number is used as a placeholder. These scalings, and the indication of whether the free stream or BBL component dominates, are indicated in Table 4.1.

All Scalings

Figures 4.6-4.9 provide information about the scaling for all of the conversion terms. In Figure 4.6, all of the conversion terms, excluding the bottom boundary layer component, are plotted versus the Burger number. Fig. 4.7 presents the same data, but the x-axes reflect the best fit scaling from Table 4.1. Figures 4.8 and 4.9 present the Burger number scaling, and the best fit scaling for the bottom boundary layer components of the conversion terms.

Physical Interpretations of Significant Conversion Terms

The pathways that describe how the mean flow is converted into unsteady and turbulent motions, ME and MT, are plotted in Figure 4.10. The shape and scaling for the ME conversion term (Fig. 4.10a) is nearly identical to that of the EKE scaling in Fig. 4.5a. The primary source of the EKE is the ME conversion term, and so it is not surprising that we obtain a similar relationship. Again, an apparent limit on this conversion term is imposed by $\mathrm{Bu}_{\mathrm{crit}}$, which corresponds to the arrest in the increase of the horizontal eddy scale.

The MT term (Fig. 4.10b) shares many of its characteristics with the TKE reservoir (Fig. 4.5d). The curves for both terms collapse when plotted against the product of the Froude and Rossby number. The suggested scaling line, however, is steeper for the MT conversion ($(\mathrm{Fr}\,\mathrm{Ro})^2$) than for the TKE reservoir ($(\mathrm{Fr}\,\mathrm{Ro})^{\frac{3}{2}}$). We attribute this difference to the fact

	Free Stream	Bottom Boundary Layer	Dominant Term
ME	Bu	Bu	Free
MT	Ro Fr	Ro Fr	BBL
ET	-	-	Balanced
MV	Fr^2 Ro	Fr^2 Ro	Balanced
EV	Fr Ro	Bu	Free
TV	Fr Ro^2	-	BBL
MB	Fr^2 Ro	Bu	Balanced
EB	Bu	Bu	Free
TB	Fr Ro^2	Fr Ro^2	Free
MKE	Bu		
EKE	Bu		
TKE	Fr Ro		
ζ^2	Bu		

Table 4.1: Suggested conversion term scalings.

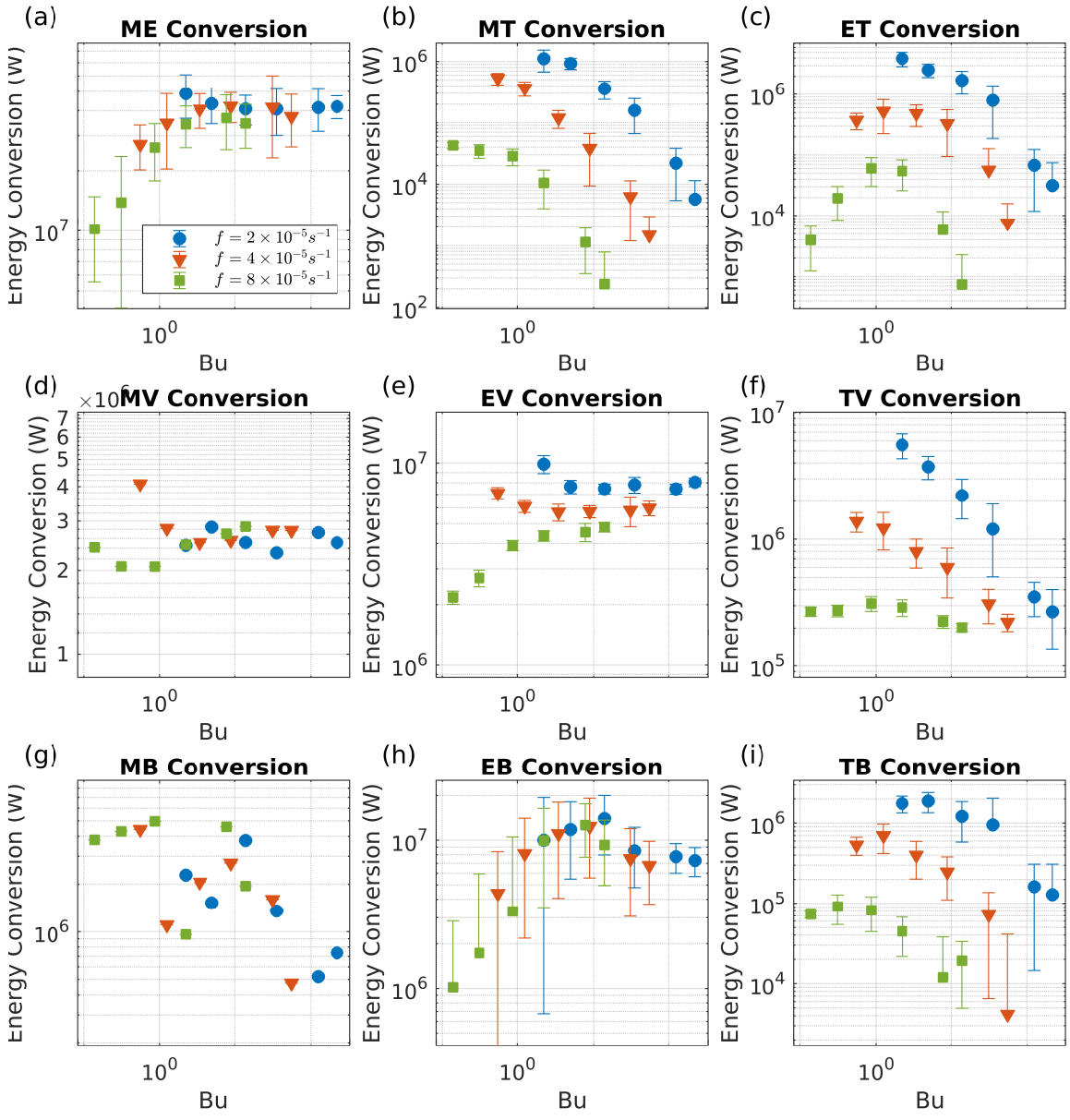

Figure 4.6: All free stream conversion term values are plotted against the Burger number.

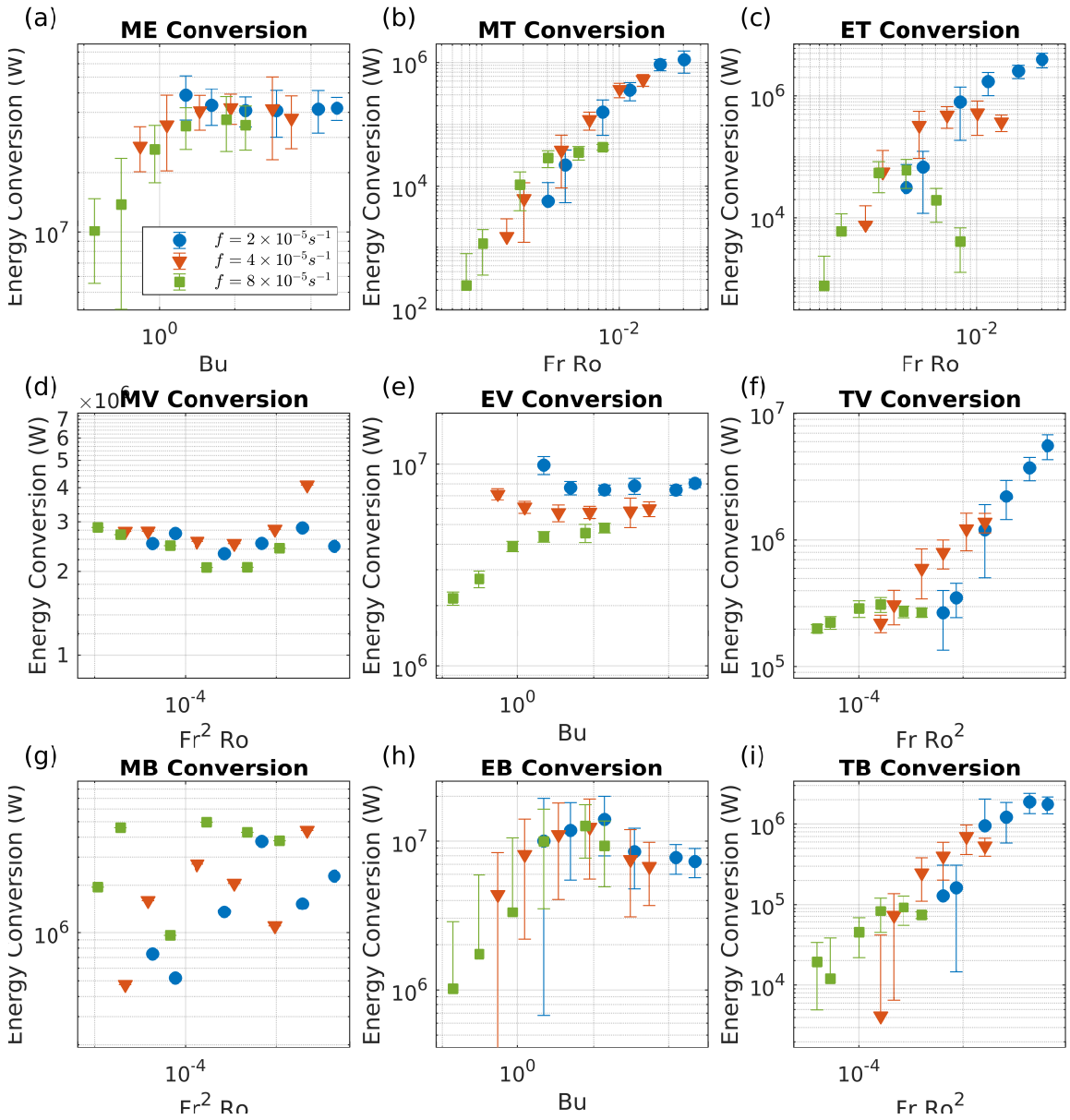

Figure 4.7: All free stream conversion term values are plotted against the most appropriate nondimensional scaling quantity. If no good scaling was found, the Burger number is used as a placeholder.

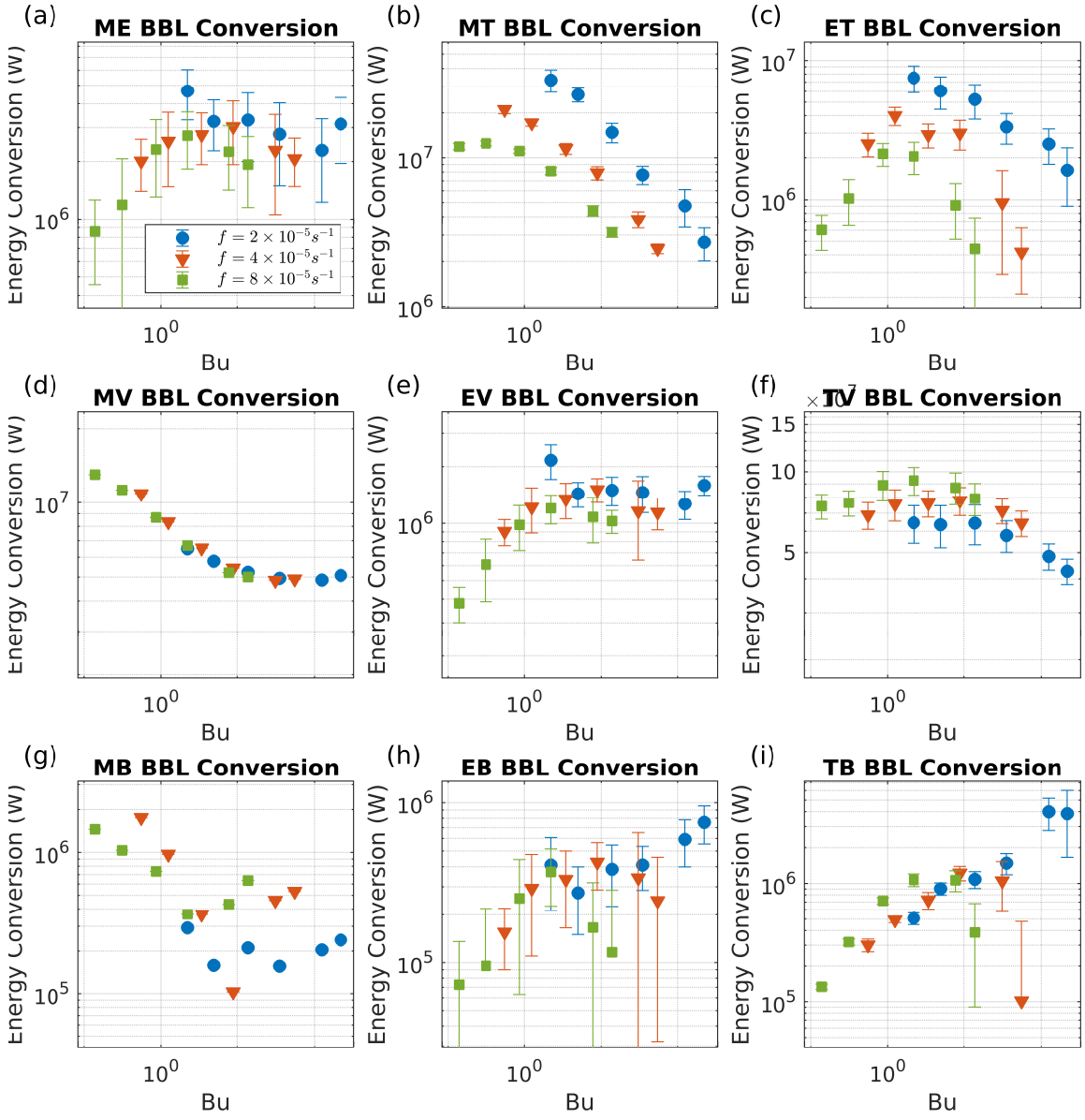

Figure 4.8: All bottom boundary layer conversion term values are plotted against the Burger number.

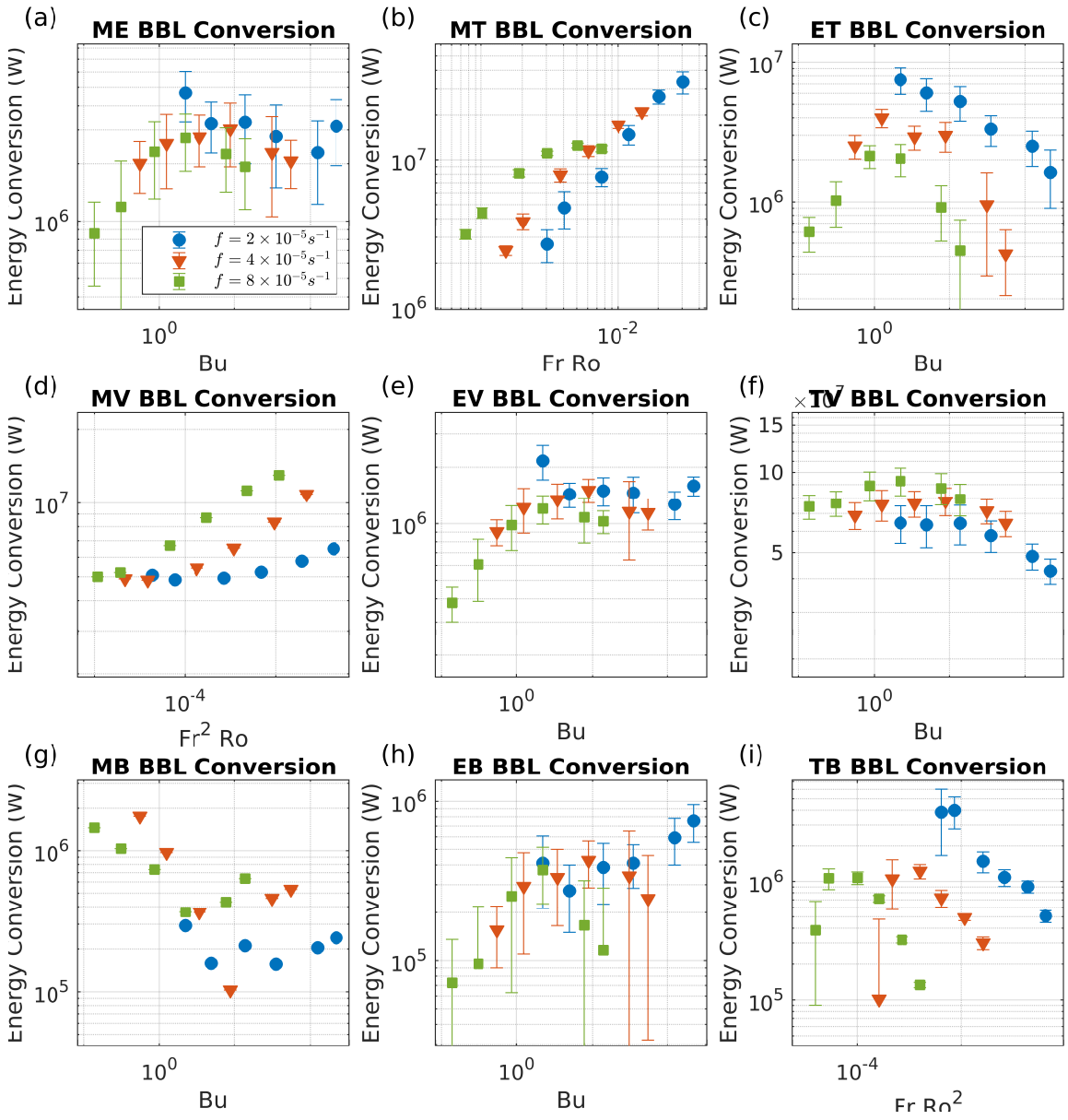

Figure 4.9: All bottom boundary layer conversion term values are plotted against the most appropriate nondimensional scaling quantity. If no good scaling was found, the Burger number is used as a placeholder.

that the TKE equation contains several terms of leading order importance (see Fig. 4.4) and encompasses the effects of a variety of physical processes. MT, however, is driven purely by shear in the mean flow. The nature of the scaling for MT suggests that the primary driver for this term has no memory of the large-scale wake structure, and instead depends on the properties of rotating, stratified turbulence.

The largest sinks in the eddy kinetic energy equation are the losses to viscosity (EV) and buoyancy (EB). EV (see Figure 4.11a) exhibits small error bars, indicating that the EV contains very little temporal variation. The time mean values largely fall in a narrow band around 5×10^6 W; only three data points fall more than 40% away from this value. In general, stronger rotation always produces a lower conversion value, but the dependence on stratification is much more complex, especially for low-Bu. No nondimensional scaling was found that could sufficiently collapse the data, and so the Burger number is used as the ordinate. We attribute the lack of a viable scaling to the wide range of physical processes that contribute to this term. The horizontal gradients that contribute to the EV conversion are active both near to the seamount, where a large local Rossby number contributes to centrifugal instability (e.g., Srinivasan et al., 2019), and in the farfield wake, where eddies may decay by instability or directly by viscosity. Furthermore, the viscosity in ROMS, which is a combination of numerical viscosity and a nominal explicit viscosity that acts as a turbulent viscosity, necessarily models subgrid-scale dynamics. The effect of this term, then, is likely influenced by the modeled viscosity, which is different from the real viscosity in an oceanographic context.

The buoyancy term, EB (Figure 4.11b), contains significantly more temporal variability than the EV term, as indicated by the large error bars. This term may also be referred to as the baroclinic conversion term in the sense of eddy energy being generated via instability from the potential energy reservoir (Dong et al., 2007). However, we find, that over the domain, the EB term is positive, representing a net production of potential energy from the EKE reservoir. This term includes all effects of unsteady vertical advection of a density anomaly, encompassing eddy motions as well as internal waves that may or may not leave

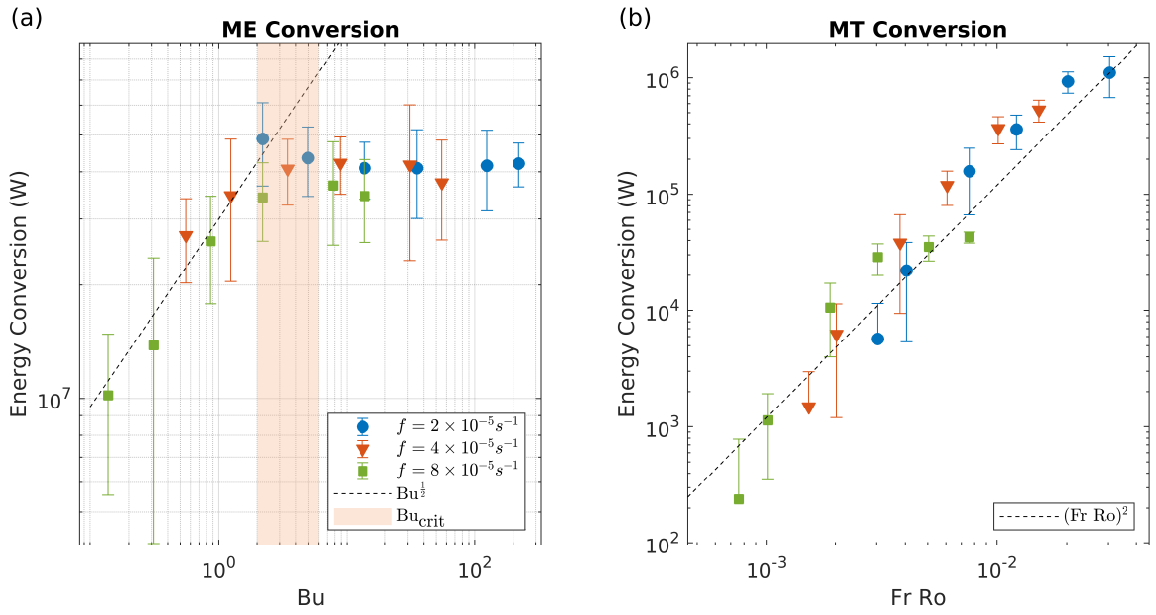

Figure 4.10: Scaling for a) the mean to eddy energy conversion, and b) the mean to turbulent energy conversion.

the analysis domain. The generation of buoyancy tends to happen in bursts, resulting in significant uncertainty in the time series. However, there appears to be a broad peak in the EB conversion that encompasses $\mathrm{Bu}_{\mathrm{crit}}$. The chaotic regime associated with the initiation of eddy decoupling forms conditions that are particularly amenable to the generation of potential energy.

4.5 Discussion

4.5.1 Quasigeostrophy

The prevalence of Burger number scalings for quantities such as the EKE, ME conversion, and EB conversion suggests that the eddy processes can be parameterized, at least partially, by the Burger number. It follows that the Burger number should enter into the leading-order dynamics that govern flow past a seamount. We find that this hypothesis can be satisfied if the flow past the seamount can be considered to be approximately quasigeostrophic (QG).

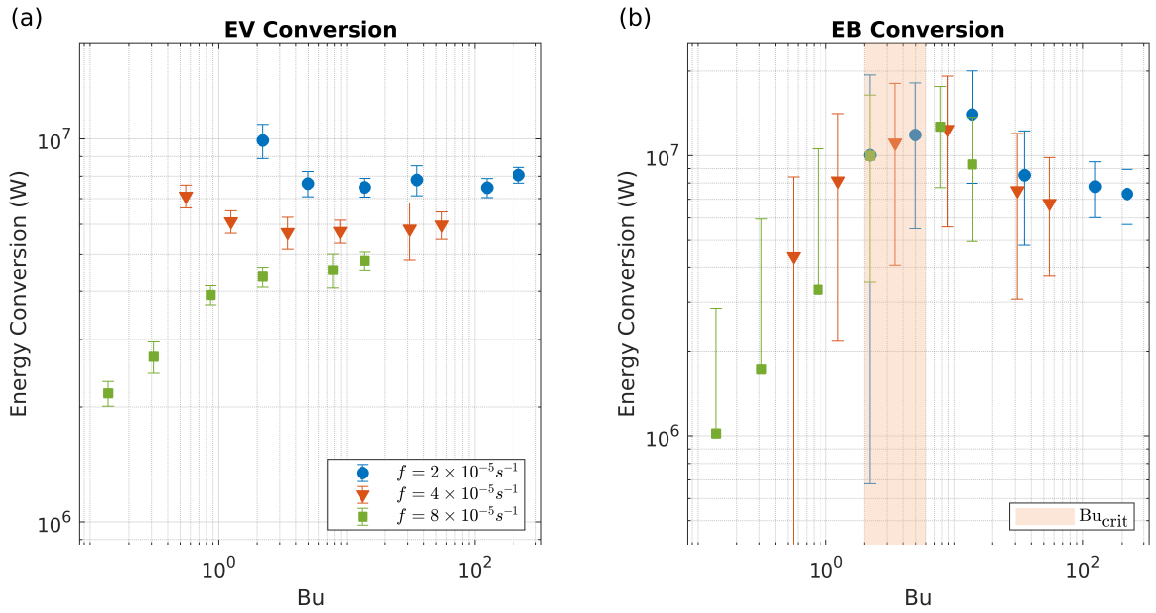

Figure 4.11: Scaling for a) the eddy to viscosity conversion, and b) the eddy to potential energy conversion.

When properly nondimensionalized, the QG equations depend only on the Burger number as the sole nondimensional parameter. Pedlosky (1987, Eq. 6.8.11) notes that for a geostrophic streamfunction ψ (and implied nondimensional coordinates), the quasigeostrophic equations can be written as,

$$\left[\frac{\partial}{\partial t} + \frac{\partial \psi}{\partial x}\frac{\partial}{\partial y} - \frac{\partial \psi}{\partial y}\frac{\partial}{\partial x}\right]\left[\frac{\partial^2 \psi}{\partial x^2} + \frac{\partial^2 \psi}{\partial y^2} + \frac{\partial}{\partial z}\left(\left(\frac{fD}{NH}\right)^2 \frac{\partial \psi}{\partial z}\right) + \beta y\right] = 0. \tag{4.18}$$

When the buoyancy frequency is vertically uniform and the beta plane effect is discarded, the equation reduces to,

$$\left[\frac{\partial}{\partial t} + \frac{\partial \psi}{\partial x}\frac{\partial}{\partial y} - \frac{\partial \psi}{\partial y}\frac{\partial}{\partial x}\right]\left[\frac{\partial^2 \psi}{\partial x^2} + \frac{\partial^2 \psi}{\partial y^2} + \mathrm{Bu}^{-1}\frac{\partial^2 \psi}{\partial z^2}\right] = 0, \tag{4.19}$$

and thus the quasigeostrophic equations are entirely determined by the Burger number. This relationship is often obscured through the use of dimensional variables, or by the use of alternate names or representations for the Burger number. The Burger number has variously

been expressed as the square of a nondimensional height (Srinivasan et al., 2019), the stratification parameter (Pedlosky, 1987), the ratio $\left(\frac{R_D}{D}\right)^2$ (e.g. Pedlosky, 1987; Perfect et al., 2018), and as other ad-hoc symbols.

The question of whether flow past a seamount can be considered to be quasigeostrophic is then important for justifying a Burger number-based parameterization of the seamount energetics. To assess whether the present simulations are near a QG regime, velocities can be decomposed into balanced (geostrophic) and unbalanced (ageostrophic) motion. The density field in the simulation is used to compute a geostrophic velocity and, when this is subtracted from the simulation velocity, the residual in considered to be the ageostropohic component. In doing this, we find that ageostrophic motions comprise between 5 and 20% of the motion within the wake region, which is approximately consistent with QG flow. Moreover, QG flow has been found to describe many flow scenarios that exist outside of the traditional requirements for the QG regime (Williams et al., 2010), so even moderate ageostrophic motion does not necessarily exclude the possibility for a useful Burger number-based representation.

We conclude that the energetic quantities that are determined by the Burger number are primarily affected by quasigeostrophic processes. Conversely, the quantities that have alternate dependencies represent processes governed by the ageostrophic component of the flow, such as bottom boundary layer effects, the MT conversion term, and the ET conversion term. Some quantities, such as the EV conversion term, may represent a blend of QG and non-QG processes; fluid instabilities that are not relevant to QG theory can also play a role that may only become apparent in certain simulations.

4.5.2 Farfield Influences

When the eddies advect out of the analysis domain, they still contain considerable energy. Typically 50-80% of the EKE is unconverted into other forms of energy, and still leaves the domain as unsteady eddy motion, as indicated in Fig. 4.12a. In Fig. 4.12a, the streamwise distribution of EKE for each simulation is normalized by its respective total EKE (see 4.5a).

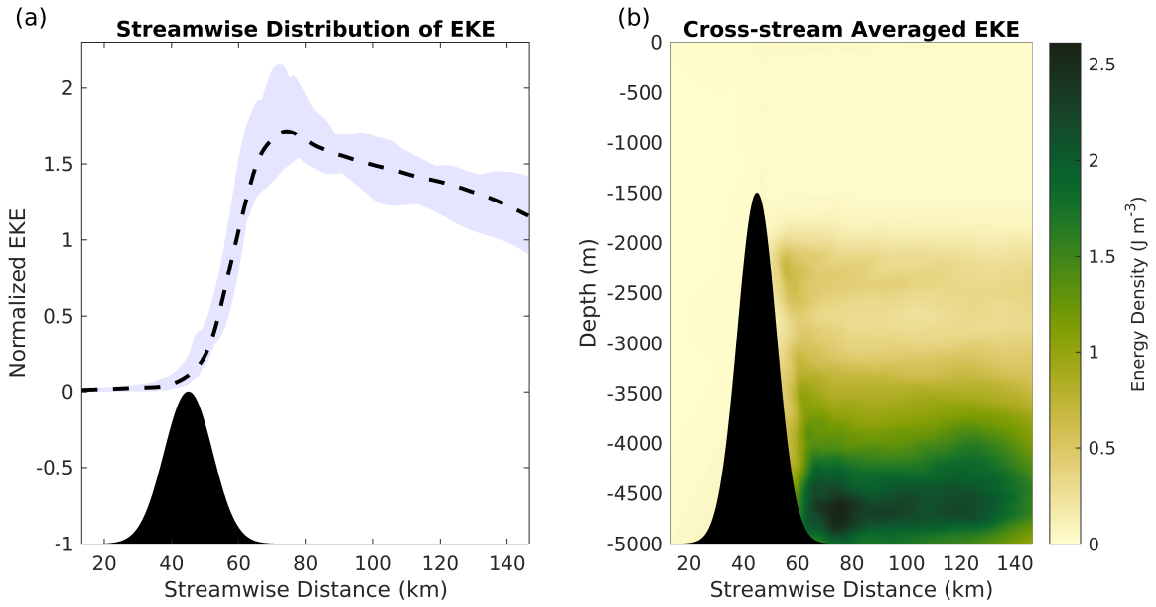

Figure 4.12: a) EKE distribution, normalized by total EKE, for all simulations. The envelope indicates the minimum and maximum normalized values, and the dashed line is the mean for all simulations. The outline of the seamount is shown below. b) A typical map of the EKE in a high-Bu simulation, which has been averaged in the cross-stream direction.

The dashed line is the mean across all simulations, while the shaded region around it indicates the range of normalized EKE values across all simulations. The streamwise distribution of EKE exhibits a strong degree of similarity among all simulations. A typical distribution for the EKE, averaged in the cross-stream direction, is given in Fig. 4.12b. The eddy energy is primarily located towards the bottom of the domain, and tends to decay both vertically and in the streamwise direction. Cases with very low Burger number (and a depth ratio approaching unity) may exhibit some EKE well above the seamount summit, though Perfect et al. (2018) did not detect any substantial vorticity above the summit.

The EKE boundary flux term (the first RHS term of Eq. 4.10) represents a significant amount of energy whose fate is likely to be converted into internal waves, turbulence, and diapycnal mixing. In the treatment of the energetics of flow past a seamount, the eddy motions that advect out of the domain cannot be neglected. In a realistic ocean, the EKE leaving the domain can later generate turbulence, internal waves or dissipation, and can also interact with other topography or coherent structures.

4.5.3 Diapycnal Diffusivity

It is often useful to quantify the effect of energetic events in the ocean in terms of the associated diapycnal diffusivity (e.g., Munk, 1966; Waterhouse et al., 2014). The diapycnal diffusivity refers to a diffusion coefficient associated with turbulent mixing of density (Osborn, 1980):

$$K_p = \frac{g\overline{w'\rho'}}{\rho_0 N^2}, \tag{4.20}$$

In Fig. 4.13a, we calculate the volume-averaged diapycnal diffusivity for the present simulations. Except for the strongest two stratifications tested, the diapycnal diffusivity scales with Fr Ro, peaking at $3\times10^{-3}\mathrm{m}^2/\mathrm{s}$. The largest calculated diapycnal diffusivities are consistent with findings in the vicinity of a Firberling Guyot, a large midlatitude seamount (Kunze and Toole, 1997). This significantly exceeds open-ocean estimates of around $10^{-5}\mathrm{m}^2/\mathrm{s}$, and would constitute one of the extreme mixing events that are believed to keep the basic-

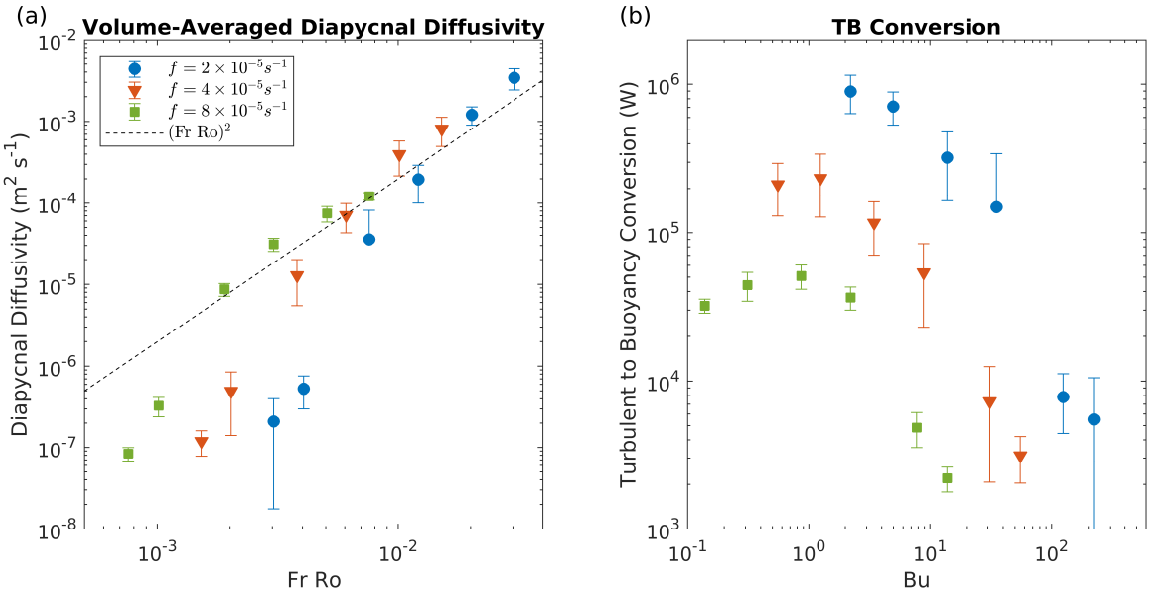

Figure 4.13: a) Volume-averaged diapycnal diffusivity is plotted versus the product of the Froude and Rossby numbers; b) The volume-integrated diapycnal flux is plotted versus the Burger number.

averaged diapycnal diffusivity around 10^{-4}m^2/s (Munk and Wunsch, 1998). The lowest calculated diffusivities, however, are well below even open-ocean estimates; this is because the background diffusivity for the simulations was reduced to 10^{-9}m^2/s, and so a typical background ocean mixing state was omitted. Because only the mixing in the simulation was either associated with the seamount wake or effectively molecular, we interpret the cases with very low K_p as contributing effectively no additional mixing over whatever background value would ordinarily be appropriate.

Because the volume over which the diffusivity is averaged is somewhat arbitrary, perhaps a better measure of the impact of the seamount is the total turbulent buoyancy flux, presented in Fig. 4.13b. This quantity is identical to the TB term in Eq.4.10; when expressed in terms of ROMS output: $\text{TB} = g\int_V -K_p\frac{\partial\bar{\rho}}{\partial z}dV = g\int_V \overline{w'\rho'}dV$. The TB term does not have a simple scaling relationship with any combination of the Froude and Rossby numbers. In general, however, increasing rotation decreases TB. For a constant Rossby number and varying Froude

number, TB has a peak at the Froude number for which $\mathrm{Bu} = \mathrm{Bu}_{\mathrm{crit}}$. The two limiting cases of very strong and very weak stratification both correspond to cases with weak diapycnal mixing. In the case of strong stratification, turbulence is suppressed and we find that the vertical velocity drops to nearly zero, and so little mixing beyond molecular diffusivity may take place. In the opposite case of stratification approaching zero, vertical motion exists, but the potential energy of that motion tends towards zero. This effect is especially evident in the curve for $f = 10^{-5}\mathrm{s}^{-1}$ in Fig. 4.13b, where both weak and strong stratification both yield substantially lower diapycnal diffusivity.

4.6 Conclusions

Through the use of a set of high-resolution simulations, we have explored the energetic aspects of flow past a seamount for a variety of rotation and stratification conditions. We find that energetic quantities related to quasigeostrophic motions (i.e., production of eddies, EKE, and unsteady buoyancy production) scale with the Burger number, consistent with theory (Majda, 2003; Pedlosky, 1987). Furthermore, the nature of this dependency suggests that there are important changes near $\mathrm{Bu}_{\mathrm{crit}}$, which is associated with the vertical decoupling of the eddies (Perfect et al., 2018). In contrast, quantities that are more closely related to turbulence and are not considered relevant to the quasigeostrophic regime exhibit a dependence on Fr Ro. These quantities increase with Fr Ro, which is consistent with the idea that turbulence is suppressed by the presence of rotation and stratification.

The above results motivate the need to further investigate seamount wakes. Because seamounts are mostly unresolved in global models, it may be important to include the effect of wakes in topographic parameterizations. The present results cannot establish that such parameterizations are strictly necessary from an energy perspective, but rather suggest that the wakes of seamounts merit further study. In addition, our results indicate that a Burger number-based parameterization of the effect of seamount wakes would be a reasonable starting point. Several major open questions remain. The first, which is the subject of Perfect et al. (2019b), pertains to how the energy flux into the seamount wake compares to

the energy flux of internal waves for an isolated seamount. This is a necessary comparison in order to justify the inclusion of wake effects in addition to internal wave radiation. The remaining questions are how the energetics of seamount wakes are affected by tides, nonuniform currents, nonuniform stratification profiles, and more realistic bathymetry. We note that the current study could likely be extended to include tides with a reasonable number of simulations, and that the energy partition in Equations 4.9-4.11 would be well-suited for a tidal analysis. Instead of using a time average and an ensemble average, tidal phase average along with an ensemble average would be required.

Chapter 5

INTERNAL WAVE FLUXES

This chapter specifically addresses the internal gravity waves that are produced in the simulations described in Chapter 2. Together, with the results from Chapter 4, we directly compare the internal wave energy flux to the production of eddy kinetic energy. Results indicate that eddy processes energetically dominate the internal wave energy flux in this parameter space, which suggests that the classical internal wave-focused view may need to be expanded to include wake effects. The internal wave field is specifically examined, and partitioned into steady lee waves and unsteady wake wakes. It is found that the lee wave energy flux cannot be explained by existing analytical theories. A lee wave model by Smith (1980) is extended into the low-Froude number regime and the effect of rotation is included. While strongly stratified experiments have previously indicated that only the top $\frac{U}{N}$ of an obstacle generates internal waves, the effect of rotation appears to modify the wavemaking height. Once the revised wavemaking height is taken into account, the lee wave energy flux can be accurately reproduced by the extended Smith (1980) model.

This chapter is organized as follows. We compare the relative importance of the lee waves, wake waves, and hydrodynamic wake in Sec. 5.2. The remainder of the chapter is focused on obtaining an accurate model for the lee waves. Section 5.3 summarizes several analytical models for lee wave flux (e.g., Bell, 1975; Smith, 1980; Voisin, 2007) and extends them to the low-Froude number (and when possible, rotating) regime. The performance of these models is compared against the lee wave energy flux in the simulations, and the model performance is discussed in Section 5.4. In Section 5.5, we assess the validity of the cap model with respect to the simulations, and then relax some of the assumptions of the cap model. We demonstrate that with some information about the isopycnal displacements from

a simulation, lee wave energy flux estimates are significantly improved. Finally, concluding remarks are in Section 5.6. The work discussed in this chapter is also available as Perfect et al. (2019b).

5.1 Background

It is well-established that global circulation models should contain parameterizations for bathymetrically-generated internal waves (Polzin et al., 1997). Traditionally, these parameterizations have either focused on computing the overall flux for stochastic arrays of seamounts (e.g. Klymak et al., 2010), or by the application of 2D internal wave theory to mid-ocean ridges (e.g., St. Laurent and Garrett, 2002; Llewellyn Smith and Young, 2003; St. Laurent et al., 2003; Klymak et al., 2010). Neither of these approaches directly address the underlying physics of a 3D seamount generating internal waves, which are not well-understood, especially in the low-Froude number, low-Rossby number regime. The simplicity of 2D wave theory had led to its adoption in a variety of 3D applications (e.g., Melet et al., 2013b) which, as Zhang et al. (2017) reports, introduces substantial inaccuracies.

In addition to the shortcomings of applying 2D wave theory to a 3D problem, recent research has suggested that seamount wakes may also play an important role in the process of extracting energy from a barotropic current (e.g., Dong et al., 2007; Perfect et al., 2018; Srinivasan et al., 2019; Perfect et al., 2019a). A motivating issue, then, is the relative importance of the internal wave field generated by the seamount compared to the hydrodynamic wake in extracting energy from the ambient flow and ultimately causing diapycnal mixing. It is expected that the answer may vary dramatically based on a number of factors, such as the Froude and the Rossby numbers (see Section 1.1). The results of the previous chapter, in conjunction with the results obtained here, permit a direct comparison between the energies in the wake and internal waves generated by a seamount.

In order to properly assess the internal waves produced by the simulations, we expand upon classical internal wave theory and apply it to the flow regimes found in the simulations. When stratified fluid flows past an obstacle, the flow over that obstacle creates perturbations

that generate internal gravity waves. The 2D case has been addressed for a wide variety of flows and obstacle shapes (e.g., Bell, 1975; Vallis, 2006). The present case deals with 3D bathymetry, which invites the flow to move predominantly around, rather than over the obstacle; this effect is especially apparent at low Froude numbers (Brighton, 1978). If the fluid is sufficiently stably stratified, fluid near the base of the obstacle in the oncoming flow can lack the kinetic energy necessary to overcome the potential energy barrier associated with ascending towards the top of the seamount, which is at a lower density (Sheppard, 1956; Drazin, 1961). The flow at lower levels then *must* go around the seamount. The transition from a bulk characterization of the flow going over versus around the seamount has been experimentally determined to occur at a critical Froude number around 0.4 (Hunt and Snyder, 1980). However, experimental values for the critical Froude number can vary considerably with topographic shape (Boyer et al., 1987; Vosper et al., 1999). It should be noted as well that a potential energy argument (also known as Sheppard's Criterion) suggests a critical Froude number of around 1. Subsequent studies have found problems with Sheppard's methodology, which neglects the effect of pressure and predicts stalled flow at the summit, though by chance the results are found to be relatively robust (Smith, 1980; Castro et al., 1990; Vosper et al., 1999). For Froude numbers significantly below the critical Froude number, experiments suggest a bifurcation in the flow behavior (Riley et al., 1976; Brighton, 1978).

When flow bifurcation occurs (see Figure 5.1), the first order solution predicts that the top $h_c = U/N$ of the topography forms a region where the flow goes over the seamount, hereafter referred to as the "cap". The height of the cap, h_c, corresponds to the vertical length scale for which $\mathrm{Fr} = 1$. There is evidence that the plane of separation that delineates the bifurcation between flow over and flow going around is tilted slightly down towards the lee side (Brighton, 1978; Dalziel et al., 2011), but this is a higher-order effect with respect to the cap height. The flow over the cap is associated with the generation of internal lee waves (Voisin, 2007). Below the cap, the flow is directed around, in the form of a stratified turbulent wake, generally with vortex shedding (Lin and Pao, 1979; Hunt and Snyder, 1980;

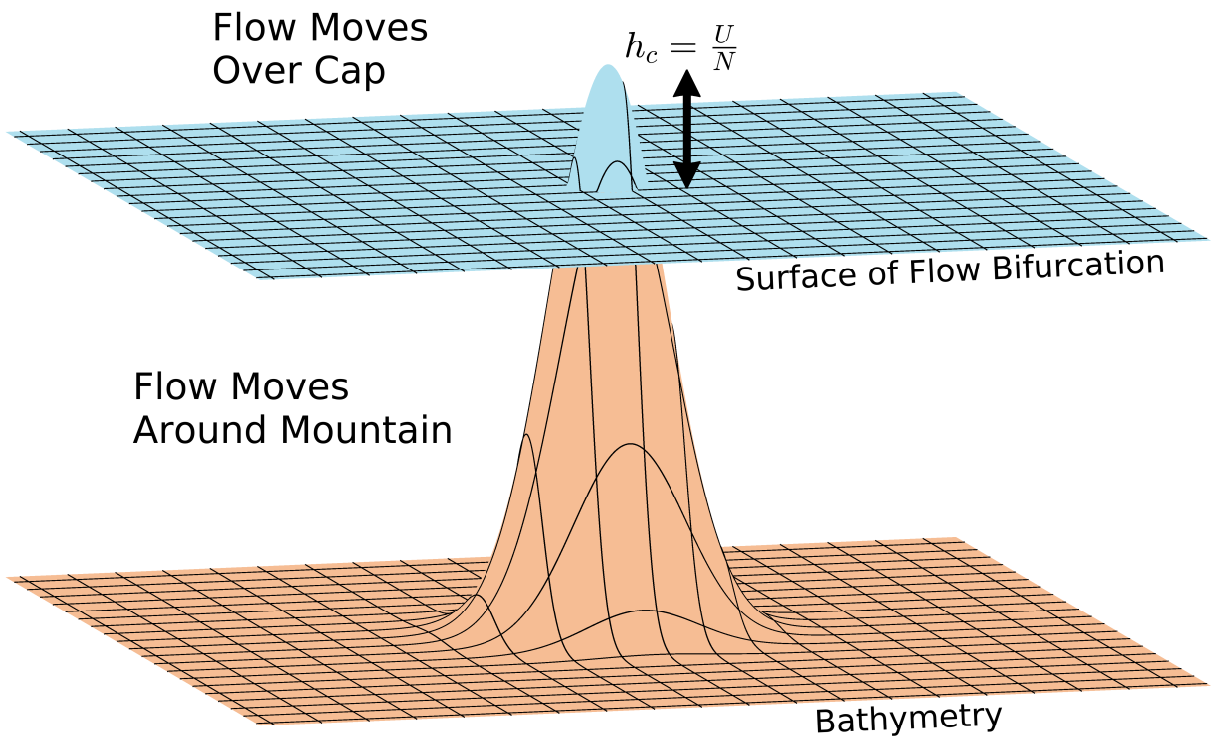

Figure 5.1: In the cap model for flow past an obstacle, a bifurcation occurs in the flow. Fluid elements more than $\frac{U}{N}$ below the summit are directed around the obstacle, and fluid elements above that plane will lift up to contour the bathymetry.

Vosper et al., 1999). Following Drazin (1961), the flow around is horizontal to first order, though it is understood that small perturbations persist (Vosper et al., 1999). Together, the assumptions that the lee waves are generated entirely by the top h_c of the seamount, and the flow more than h_c below the summit flows horizontally and forms a stratified wake, are referred to as the cap model, or the cap assumption[1]. The cap model is presented visually in Figure 5.1. Much in line with the previous analysis in this section, the surface of flow bifurcation is understood to only be a plane as a first order treatment. When the wake contains significant vertical perturbations, it can generate "random" internal gravity waves (e.g., Brandt and Rottier, 2015; Meunier et al., 2018). While the overall internal wave field can contain signals from both lee and wake waves, they are considered to be dynamically separate (Gilreath and Brandt, 1985; Riley and Lelong, 2000). In the context of a steady flow past a seamount, the different types of internal gravity waves may be distinguished by the steady (lee) and unsteady (wake) components.

The results developed here are obtained from a subset of the simulations described in Chapter 2. This subset, shown in Figure 5.2, spans a Froude-Rossby space of $0.014 < \mathrm{Fr} < 0.14$ and $0.053 < \mathrm{Ro} < 0.21$. Therefore, $0.14 < \mathrm{Bu} < 221$. A critical Burger number separates a regime with rotationally-dominated, vertically-aligned vortices (circles with a blue background in Fig. 5.2) from the regime with stratification-dominated, vertically decoupled vortices (triangles with a red background in Fig. 5.2). While this transition corresponds to significant changes in the eddy structure and wake energetics, it is not clear whether it is significant for the internal wave generation.

5.2 Wave Energy Flux Evaluation

A key result of this study is that the rate of energy flux due to internal waves can be directly compared to the generation rate of eddy kinetic energy. This comparison evaluates the extent to which the simulated seamount can described as a "stirring rod" versus a source of internal

[1]Particularly in the 2D case, the plane of flow bifurcation is also referred to as the "dividing streamline"

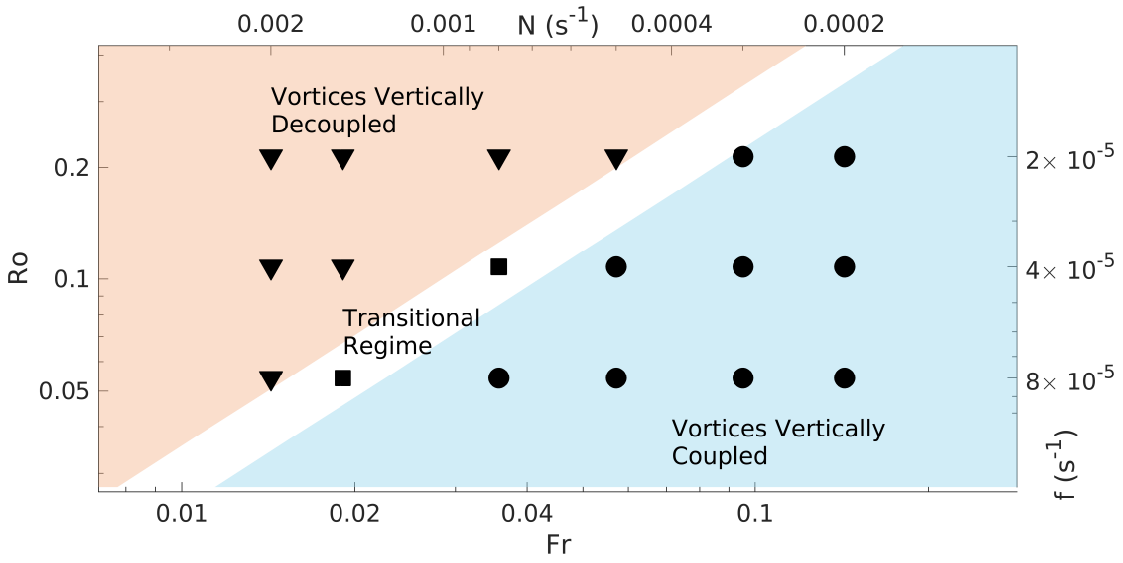

Figure 5.2: The 18 simulations used for this study are plotted by Froude and Rossby number (lower and left axis), as well as by buoyancy frequency and Coriolis parameter (top and right). The different shedding regimes are noted on the figure, with the symbols indicating regime associated with each simulation.

waves for this idealized case of an isolated seamount in a steady, barotropic flow with uniform stratification. Note that the flow conditions in the present study were chosen specifically to emphasize the wake development, and are probably not representative of the comparison for the case of a 2D ridge in tidal flow (e.g., St. Laurent and Garrett, 2002; Llewellyn Smith and Young, 2003; St. Laurent et al., 2003; Klymak et al., 2010). Large, isolated seamounts are common enough in Earth's oceans that the Gaussian seamount of the present study is a reasonable bathymetry for comparing the energetics of the wake and internal waves (Wessel et al., 2010).

We find, in line with Gilreath and Brandt (1985), that the internal wave field consists of a steady (in the frame of the seamount) lee wave pattern and an unsteady, random wave field arising from adjustment processes. The lee waves, particularly at large Rossby number (see Fig. 5.3a), resemble a Kelvin wake (also reported in Smith, 1980). This pattern is visualized in Fig. 5.3 using horizontal slices of the time-averaged vertical velocity. As the

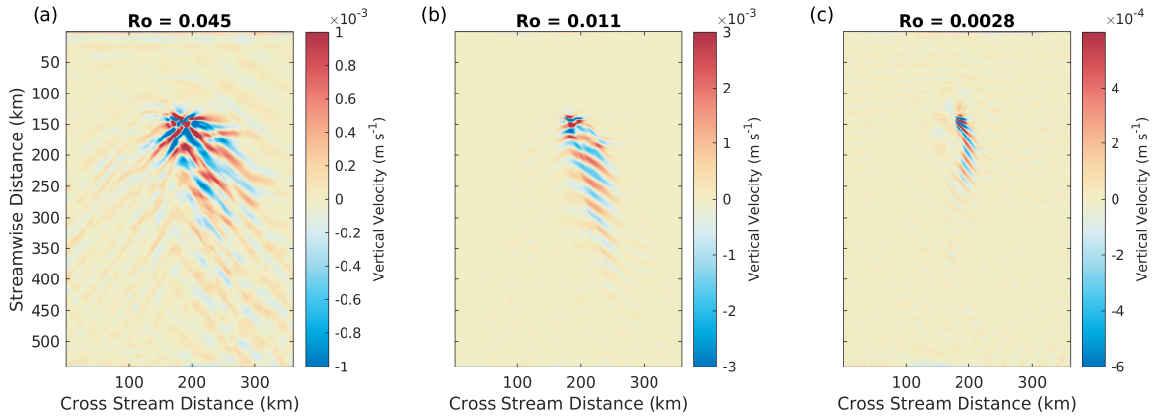

Figure 5.3: The lee wave Kelvin wake pattern is demonstrated using the steady vertical velocity field, $\bar{w}$. Each subfigure plots a horizontal slice of $\bar{w}$ taken $2h_c$ above the summit of the seamount. In (a), the wake pattern is largely unaffected by rotation and it propagates for several hundred kilometers downstream. (b) and (c) show how at progressively lower Rossby numbers, the wake becomes asymmetric and is confined near the seamount.

effect of rotation increases (Fig 5.3b-c), the lee wave wake pattern becomes increasingly asymmetrical and the lee waves are trapped closer to the seamount. The low-frequency waves that would normally propagate at low angle and form the farfield component of the Kelvin wake are predominantly subinertial, forming evanescent modes that are confined near the topography.

To separately compute the lee waves and unsteady (wake) waves, we decompose the vertical velocity (w) field using a time average ($\bar{\cdot}$), as done in Equation 4.1:

$$w = \bar{w} + \hat{w}. \tag{5.1}$$

We also consider a decomposition of the density field that consists of a uniform background density (ρ_0) and an ambient stratification profile in the vertical ($\rho_s(z)$), plus a perturbation density that includes time-averaged ($\bar{\rho}$) and unsteady ($\hat{\rho}$) components. Then,

$$\rho = \rho_0 + \rho_s(z) + \bar{\rho}(x, y, z) + \hat{\rho}(x, y, z, t). \tag{5.2}$$

We will drop the arguments from the perturbation terms for the sake of brevity, but it

is understood that they vary spatially and that the unsteady component also has a time dependence.

The vertical energy fluxes (per unit area) associated with lee waves and wake waves are computed as:

$$F''_{\text{lee}} = \bar{w} \int_{-h}^{0} \bar{\rho} g dz \qquad F''_{\text{wake}} = \overline{\hat{w} \int_{-h}^{0} \hat{\rho} g dz}, \tag{5.3}$$

where the upper limit of integration is the ocean surface. In the latter equation, the unsteady wave flux is time averaged. A bulk value for the wave flux is obtained by integrating the local vertical flux over a horizontal plane $\mathcal{A}$ spanning the simulation domain:

$$F_{\text{lee}} = \int_{\mathcal{A}} \bar{w} \int_{-h}^{0} \bar{\rho} g dz d\mathcal{A} \qquad F_{\text{wake}} = \int_{\mathcal{A}} \overline{\hat{w} \int_{-h}^{0} \hat{\rho} g dz} d\mathcal{A}. \tag{5.4}$$

In order to compensate for wave reflections propagating downward through the domain, only the positive components of the wave flux are summed. Also, note that these terms are related to the second terms on the RHS of Equations 4.9 and 4.10. Whereas Equations 4.9 and 4.10 include the pressure work on all boundaries, the wave flux explicitly refers to the top of the analysis domain. ϕ, as used in Chapter 4, is related to the density in Eq. 5.4 via the hydrostatic assumption. Specifically, $\frac{1}{\rho_0} \int_{-h}^{0} \rho g dz = \phi(z = -h)$.

F_{lee} and F_{wake} are compared to the rate of eddy energy generation in Figure 5.4. The mean to eddy conversion (details for this calculation are provided in Section 4.2.3, as well as by Perfect et al. (2019a)) represents the rate at which eddy kinetic energy is extracted from the mean flow, and is found to dominate both the lee wave and wake wave energy fluxes in all cases. Perfect et al. (2019a) reports that the mean to eddy conversion initially increases with the Burger number, before reaching a saturation value above a critical Burger number. Because the mean to eddy conversion is several decades larger than the wave energy fluxes, the Burger number dependence is readily discernible only in the right hand side of Fig. 5.4c, which corresponds to low Burger number. The wake and lee wave energy fluxes do not share the same scaling as the mean to eddy conversion, but they appear to scale in a mutually similar manner. The nature of this dependence will be discussed in greater detail in Section

5.5.

For Fr < 1, the Froude number describes approximately the proportion of the seamount that can generate lee waves. The remaining lower portion primarily produces eddies, which may in turn radiate wake waves. Despite the great majority of the seamount producing unsteady motion, the wake wave energy flux is lower than the lee wave energy flux in all cases. This finding is consistent with Brandt and Rottier (2015), which finds that, as Fr < 1, the energy flux of the wake waves is dominated by the energy flux of lee waves. Physically, the stratification inhibits vertical motion, which is necessary for the generation of gravity waves. Vertical and ageostrophic motions generated in the wake are quickly damped out downstream of the seamount. In a nonrotating regime, Bonneton et al. (1996) and Kadri et al. (1996) describe wake waves that substantially decay within 10 buoyancy periods. For comparison, the advection time for the flow to move past the seamount in the present simulations corresponds to $50 < Nt < 500$. The wake, then, ages very rapidly in its ability to generate waves, especially relative to the timescale of the eddy shedding (i.e., the buoyancy timescale is approximately an hour, whereas the eddy shedding period is several days). Consistent with this, we find that most of the unsteady wave flux is concentrated near the seamount where the eddies are forming, and very little is generated in the farther wake. While the wake vortices weaken as they advect downstream, as found by Perfect et al. (2019a), that weakening is not associated with significant internal wave generation. This runs contrary to the findings of Bonneton et al. (1993, 1996), who demonstrate a strong coupling between coherent wake structures and wake wave radiation. A possible explanation for the discrepancy is that the rotation in the present simulations, which was not considered in other wake wave studies, acts to stabilize the vortices. Additionally, by the time coherent vortices may be distinguished in the wake, the wake is already quite old, and scaling by Voisin (1991) suggests that nonrotating wake waves would have almost entirely decayed by that point. In our simulations, any possible vortex-wave coupling is obscured by the uncertainties in the pressure and vertical velocity fields.

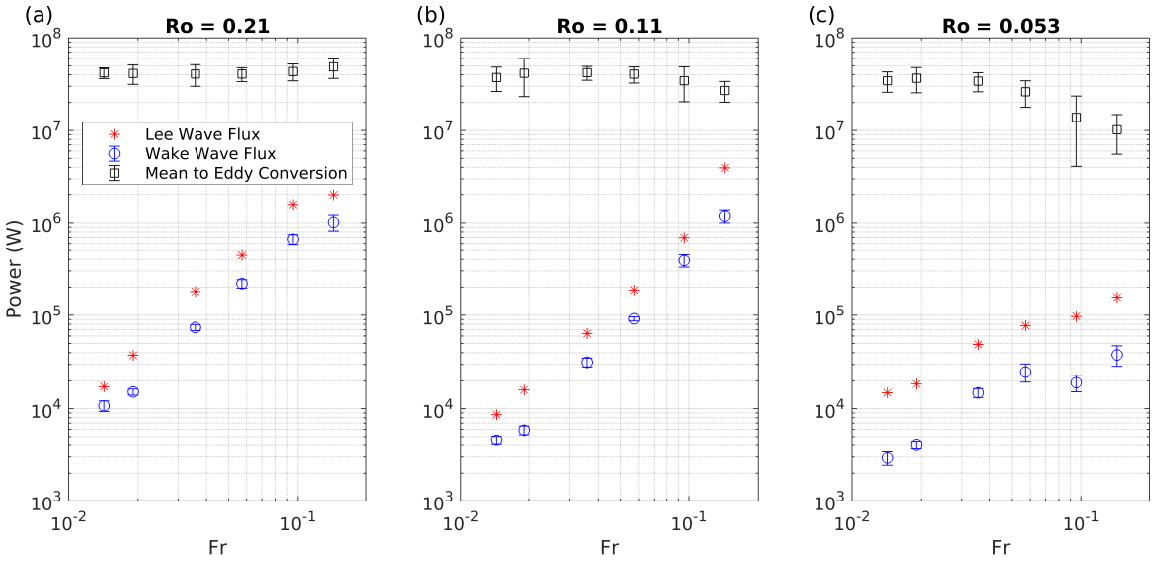

Figure 5.4: Comparison of the power associated with the production of eddies, the lee wave energy flux, and the eddy-generated internal wave energy flux. The comparison is presented for (a) f= 2×10^{-5}, (b) f= 4×10^{-5}, and (c) f= 8×10^{-5}.

5.3 Predicting Lee Wave Flux

It is desirable to relate the energy flux due to lee waves in Figure 5.4 to that predicted by models using internal wave theory. We present several pre-existing lee wave energy flux models, and then adapt them to the present simulations. When practical, we extend these models to include additional relevant physics, such as the cap model (i.e., flow bifurcation occuring at h_c) and the effect of rotation.

5.3.1 Voisin

Voisin (2007) defines a drag coefficient C_D associated with the wavemaking drag of several obstacles, including the Gaussian employed in the current study. Voisin explicitly treats the low-Fr case, making use of the cap model to isolate the wavemaking component of the drag. Rotation, however, is not considered in this model. The drag force, F_D, is given by $F_D = \frac{1}{2} C_D \rho_0 A U^2$, where A is the frontal area of the obstacle. Voisin finds that, for a wide

class of obstacles, $C_D \propto \mathrm{Fr}^{3/2}$. The constant of proportionality is determined by geometric factors, and the wave energy flux is obtained by multiplying the drag by a uniform flow velocity (U). For the case of a Gaussian, the lee wave energy flux is given by:

$$F_{\text{Voisin}} = \frac{8}{15}\mathrm{Fr}^{\frac{3}{2}} Ha\rho_0 U^3, \tag{5.5}$$

where a is the characteristic horizontal scale of the Gaussian seamount. The wavemaking drag is independent of the drag associated with flow separation, and this relation is only valid for low-Froude number flows where the cap model applies.

5.3.2 Bell

Bell (1975) develops a classical theory for the wave flux for 2D flow over a small obstacle; again, rotation is not included. This simple model has been extensively used for many estimates of internal wave radiation in oceanographic applications (Melet et al., 2013a). Because this model is often applied to complex 3D bathymetry, it is useful to compare Bell's 2D model against other 3D models, as well as the simulation results. In the case of a Witch of Agnesi[2] in steady flow, as studied in Bell's paper, the radiated wave energy flux is found to be,

$$F = \frac{\rho_0 \pi}{2} U^2 H^2 N l, \tag{5.6}$$

where we have added an implied length scale l in the cross-stream direction. In order to extend this expression to a low-Froude number regime, the topographic height H should be replaced by the cap height $\frac{U}{N}$. Bell's argument that the wave flux for a Witch of Agnesi is approximately equivalent to that of a Gaussian is extended to the Gaussian cap, without additional justification (though we later find that this assumption is reasonable). It is of interest whether Bell's model can accurately compute wave energy fluxes for different topography than the Witch of Agnesi that was used in the original derivation. Eq. 5.6, with the

[2]The Witch of Agnesi is a shape defined by $y = \frac{H}{(x^2/a^2+1)^{3/2}}$. Bell notes that the expected behavior of an obstacle such as a Gaussian is essentially the same, though much more complex to solve for analytically.

cap height substitution, yields

$$F = \frac{\rho_0 \pi}{2} \frac{U^4}{N} l. \tag{5.7}$$

If we take l to be proportional to the cross-stream extent of the cap, further simplification is possible. For a Gaussian defined by $h = He^{-y^2/a^2}$, the horizontal extent of the cap is determined by the y-coordinate at which $h = H - h_c$. Solving, $y = a\sqrt{-\log(1 - \frac{h_c}{H})}$. Then, invoking the proportionality and noting that $\frac{h_c}{H} = \mathrm{Fr}$,

$$l \propto a\sqrt{-\log\left(1 - \mathrm{Fr}\right)}. \tag{5.8}$$

A first order Taylor expansion about $\mathrm{Fr} = 0$ yields $l \propto \sqrt{\mathrm{Fr}}$. Combining this with the wave flux equation and using the definition of the Froude number, we find that,

$$F_{\mathrm{Bell}} = \frac{\pi}{2} \mathrm{Fr}^{\frac{3}{2}} H a \rho_0 U^3. \tag{5.9}$$

This differs from the Voisin estimate, Eq. 5.5, by a constant, but the Froude dependency and dynamical representation are identical. The same first order expansion also yields the same result for a Witch of Agnesi (a common topographical form in analytical studies (e.g., Smith, 1980)), though the higher order representations are different.

5.3.3 Smith

Smith (1980) models the isopycnal displacement field of a 3D Witch of Agnesi in nonrotating, high-Froude number flow, and analytically explores the behavior of this field in asymptotic conditions. However, the underlying method is generally valid for all bathymetry if $\mathrm{Fr} \geq 1$. We may extend this model to a low-Froude regime by using the cap model. Rather than using the actual bathymetry of the idealized seamount, we treat the surface of the flow bifurcation (as in Fig. 5.1) as a virtual bottom. Under the assumptions of the cap model, no waves may be generated from flow below the bifurcation, so that component of the flow may be neglected. Treating the virtual bottom as a revised bathymetry, the seamount effectively becomes an obstacle with $\mathrm{Fr} = 1$, which is within the range of applicability of Smith's 1980 theory.

Smith (1980) expresses the isopycnal displacement field, η using the horizontal Fourier transform:

$$\eta(x,y,z) = \int_{-\infty}^{\infty}\int_{-\infty}^{\infty} \hat{\eta}(k,l,z)e^{i(kx+ly)}dkdl. \tag{5.10}$$

The steady, rotating Boussinesq equations linearized about a mean flow U in geostrophic balance are:

$$Uu_x - fv = -\frac{1}{\rho_0}p_x \tag{5.11}$$

$$Uv_x + fu = -\frac{1}{\rho_0}p_y \tag{5.12}$$

$$\rho_0 U w_x = -p_z - \bar{\rho}g \tag{5.13}$$

$$U\bar{\rho}_x = -w\frac{d\rho_s}{dz} \tag{5.14}$$

$$u_x + v_y + w_z = 0 \tag{5.15}$$

Here the subscripts are taken to be derivatives, lower case variables represent steady perturbations, and the density terms are as defined in Eq. 5.2. Defining the isopycnal displacement η in terms of the steady density perturbation $\bar{\rho}$ as

$$\bar{\rho} = \frac{\rho_0 N^2}{g}\eta, \tag{5.16}$$

then Eq. 5.14 can be written as,

$$w = U\eta_x. \tag{5.17}$$

To complete the problem, the kinematic condition can be written as,

$$w(x,y,0) = U\frac{\partial}{\partial x}h(x,y), \tag{5.18}$$

where $z = h(x,y)$ defines the bottom boundary of the cap, which is the upper surface in Figure 5.1. The equation for the isopycnal displacement is found to be (e.g., Kundu et al., 2004),

$$\frac{\partial}{\partial x^2}(\nabla^2\eta) + \frac{f^2}{U^2}\frac{\partial^2}{\partial z^2}\eta + \frac{N^2}{U^2}\nabla_H^2\eta = 0. \tag{5.19}$$

We then take the Fourier transform (denoted as $\mathcal{F}\{\cdot\} = \hat{(\cdot)}$) of this relation:

$$k^2(k^2+l^2)\hat{\eta} - k^2\hat{\eta}_{zz} + \frac{f^2}{U^2}\hat{\eta}_{zz} - \frac{N^2}{U^2}(k^2+l^2)\hat{\eta} = 0. \tag{5.20}$$

Note that $\hat{(\cdot)}$ now denotes the Fourier transform, rather than the eddy scale, which was used earlier. This differential equation permits solutions of the form,

$$\hat{\eta}(k,l,z) = \hat{\eta}(k,l,0)e^{imz}, \tag{5.21}$$

where

$$m^2 = \frac{(k^2+l^2)(N^2-U^2k^2)}{U^2k^2-f^2}. \tag{5.22}$$

Under the hydrostatic approximation (i.e., $Uk \ll N$) this reduces to,

$$m^2 = \frac{(k^2+l^2)N^2}{U^2k^2-f^2}, \tag{5.23}$$

which is the dispersion relationship for hydrostatic inertial internal gravity waves.

The hydrostatic approximation is invoked for two reasons. Firstly, the simulations to which this wave flux estimate will be compared are also hydrostatic. Secondly, we find that relaxing the hydrostatic approximation does not significantly affect the forthcoming results, yet results in a less computationally expensive model when compared to the nonhydrostatic version. For a nonhydrostatic simulation, it may be desirable to use the nonhydrostatic dispersion relation.

Using the kinematic boundary condition (Eq. 5.18), the flow at $z = 0$ should contour the bathymetry. In the low-Fr extension, the surface of flow bifurcation (n.b., Fig 5.1) is the contour of interest that the flow follows, and this should be used in place of the bathymetry. For a flow contour described by $h(x,y)$, we can say that, $\hat{\eta}(k,l,0) = \hat{h}(k,l)$. The isopycnal displacement can then be written as the inverse transform of the product of the wavenumber transform of $h(x,y)$ and the vertical wave propagation:

$$\eta(x,y,z) = \int_{-\infty}^{\infty}\int_{-\infty}^{\infty} \hat{h}(k,l)e^{imz}e^{-i(kx+ly)}dkdl \tag{5.24}$$

Equation 5.24 may be evaluated numerically. From η, the internal wave flux may be evaluated using linear theory. For a hydrostatic flow, Equations 5.13 and 5.18 become, respectively,

$$p(x,y,z) = \int_z^\infty \rho_0 N^2 \eta(x,y,z')dz' \tag{5.25}$$

$$w(x,y,z) = U\eta_x(x,y,z). \tag{5.26}$$

In Eq. 5.25, the integral computes the effect of all isopycnal displacements above the fluid element of interest for an infinitely deep ocean. In practice, the displacements decay with height and the pressure field is sufficiently converged by a height of $50h_c$. The internal wave flux is computed as

$$F_{\text{Smith}} = \iint_{\mathcal{A}} pwd\mathcal{A} = \iint_{\mathcal{A}} \mathcal{F}^{-1}\{ik\hat{h}(k,l)e^{imz}\} \int_z^\infty \rho_0 N^2 \mathcal{F}^{-1}\{\hat{h}(k,l,0)e^{imz}\}dz'd\mathcal{A}, \tag{5.27}$$

where $\mathcal{A}$ is taken to be a surface that encloses the causality envelope of the topography (i.e., all wave radiation from the mountain must cross $\mathcal{A}$.)

5.4 Model Performance

We evaluate the performance of three nonrotating lee wave flux models, based on Bell (1975) (see Eq. 5.9, referred to as Bell hereafter), Voisin (2007) (see Eq. 5.5, referred to as Voisin hereafter), and Smith (1980) (see Eq. 5.27, referred to as nonrotating Smith hereafter). In the nonrotating Smith model, the Coriolis parameter is set to zero in Eq. 5.23. A fourth model is also based on Smith's model, but includes a nonzero Coriolis parameter, and is referred to as the rotating Smith model. The lee wave energy fluxes predicted by these models are plotted alongside the simulation data in Figure 5.5.

The nonrotating models (the straight red lines in Fig. 5.5) do not depend on the Rossby number, and so they appear identical in each frame. The Bell and Voisin estimates share the same $\text{Fr}^{\frac{3}{2}}$ scaling and differ only by a constant multiplicative factor, as explained in Sections 5.3.1 and 5.3.2. The Voisin model more closely matches the data, which is to be expected because Voisin explicitly addresses a Gaussian in strongly stratified flow, whereas the Bell model contains significant assumptions in extending the model to a 3D, low-Froude number

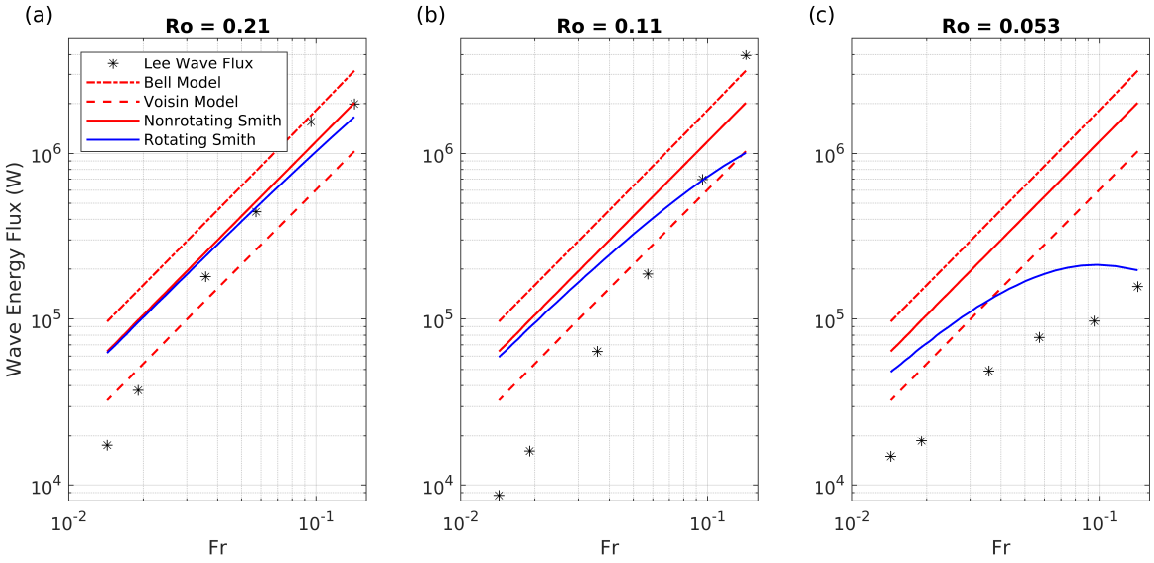

Figure 5.5: Comparison of several lee wave models (plotted as lines) against lee wave flux data (plotted as black asterisks). The three panels indicate the three Coriolis parameters used, as in Fig. 5.4. The straight red lines represent the nonrotating models: Voisin (dashed), Bell (dot-dash), and Smith (solid). The curved solid blue line is the rotating Smith model.

regime. We observe that the nonrotating Smith model also obeys a $\mathrm{Fr}^{\frac{3}{2}}$ scaling, though this cannot be readily derived from Smith's formulation. Together, the nonrotating models capture the broad trends of the internal wave energy flux at low and moderate rotation (Fig. 5.5a and b), but it is clear that the $\mathrm{Fr}^{\frac{3}{2}}$ scaling is incorrect. The simulation data suggest that, in agreement with Brandt and Rottier (2015), the wave flux scales approximately with Fr^2. As rotation becomes strong (Fig. 5.5c), the Froude dependence of the simulation data changes dramatically, which is not captured by the nonrotating models.

The rotating Smith model (the solid blue lines in the panels of Fig. 5.5) is nearly identical to the nonrotating Smith model when the Rossby number is relatively large (Fig. 5.5a and b). At low Rossby number, the rotating Smith model diverges significantly from its nonrotating counterpart and much more closely follows the simulation data. In Fig. 5.5b, the addition of rotation to the Smith model causes the model to adjust away from the simulation data at the high-Fr range. The rightmost simulation datapoint may be an outlier, for reasons

discussed in Section 5.5.

The small values for the wave flux in Fig. 5.5c can be justified as a consequence of the dispersion relation for linear internal gravity waves. A substantial proportion of the waves excited by the topography become evanescent modes at low-Rossby number. These modes, which were free to propagate at higher Ro, are now confined to the seamount, as shown in Fig. 5.3. For a nonhydrostatic application, the range of propagating frequencies is $f < \omega < N$ (while we do not invoke the upper bound restriction in our analysis, we do not find significant energy at frequencies above N, and so this range effectively encapsulates the range of frequencies seen). As f and N approach each other, as in the right side of Fig. 5.5c, the allowable band of frequencies becomes quite narrow. In the most extreme case of the present study, the internal wave band is restricted to $8 \times 10^{-5}\mathrm{s}^{-1} < \omega < 2 \times 10^{-4}\mathrm{s}^{-1}$.

5.5 Cap Height Model Relaxation

In the previous sections we have assumed, uncritically, that the interaction of the wavemaking flow and the seamount can be perfectly described as flow over the cap, the top $h_c = \frac{U}{N}$ of the seamount. While this framework is generally supported by potential energy arguments and experimental observations, our data suggest that the cap model is inadequate, especially under the effect of rotation. As suggested by Fig. 5.3, as the Rossby number decreases, the simulated lee waves become increasingly asymmetric. The Smith models, which are the only models that compute the structure of the lee waves, cannot reproduce the observed asymmetry with a cap model. Additionally, we find that the cap heights in the simulations can be described to first order by h_c, but contain significant deviations that require a correction to the cap height.

In this section, we investigate the inadequacies of the cap model through the use of isopycnal surfaces and the cap heights computed from the simulations. We then relax the assumption that $h_c = \frac{U}{N}$ and modify the rotating Smith model to use a cap height correction factor. This modification to the Smith model takes two forms: the cap height correction factor can be taken directly from the simulation or, more generally, an empirical fit to the

simulation data can prescribe a correction factor based on the rotation and stratification. The assumption that the waves are generated by a kinematic boundary condition on the theoretical seamount cap is also relaxed. In this case, the Fourier transform of the cap ($\hat{h}(k,l)$) in the rotating Smith model is replaced with the Fourier transform of an isopycnal surface. This correction, referred to as the isopycnal Smith model, permits the asymmetries observed in the simulation to be reproduced in the model.

5.5.1 Isopycnal Displacements

A key assumption of the cap model is that at vertical levels more than h_c below the summit, the flow is confined to horizontal planes. We test this assumption by calculating, for every simulation, the vertical perturbation of an isopycnal that is well below the cap. We use the isopycnal corresponding to $\rho_s(-3000m)$, which is 1500m below the seamount summit in the incoming flow. These isopycnal displacement maps are normalized by h_c, and then plotted in Figure 5.6. For strong stratification and weak rotation, the isopycnal displacement is negligible. The bottom right corner of Figure 5.6, however, indicates isopycnal displacements exceeding h_c, in clear violation of the cap model. The large isopycnal displacements are caused by adjustment processes associated with the turning flow. The length scale associated with these displacements suggests that they are large relative to $\frac{U}{f}$, and therefore correspond to subinertial motion. While these structures violate the cap model by producing significant isopycnal displacements below the cap, it is not clear whether this violation impacts the lee wave field to a significant degree. A fluid particle flowing over the deflected isopycnals would likely not produce propagating waves because the associated motion would tend to be subinertial. The simulations results support this interpretation; there is no evidence that propagating waves are generated at the seamount flanks.

Figure 5.7 also plots normalized isopycnal displacements, but at a vertical level that is approximately at the seamount summit. Unlike in Fig. 5.6, significant displacements on the order of h_c exist for all of the simulations. The cap model predicts that isopycnal displacements of h_c should be observed at the seamount summit, and Fig. 5.7 supports this

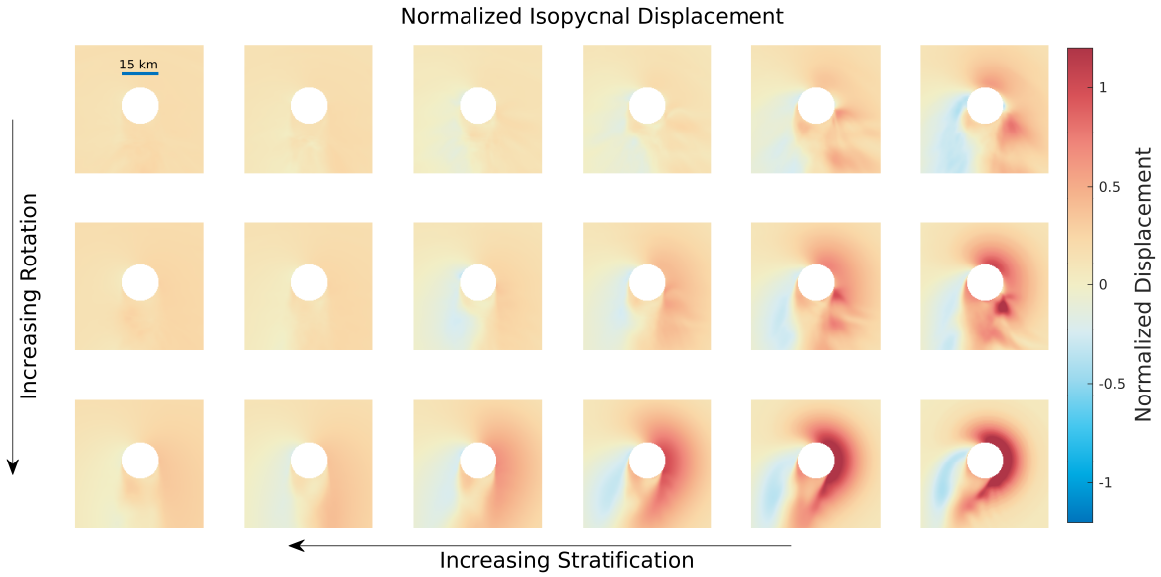

Figure 5.6: Normalized isopycnal deflection maps 1500m below the seamount summit. The direction of flow in each image is from top to bottom. Images are arranged in the same pattern as the datapoints in Fig. 4.1

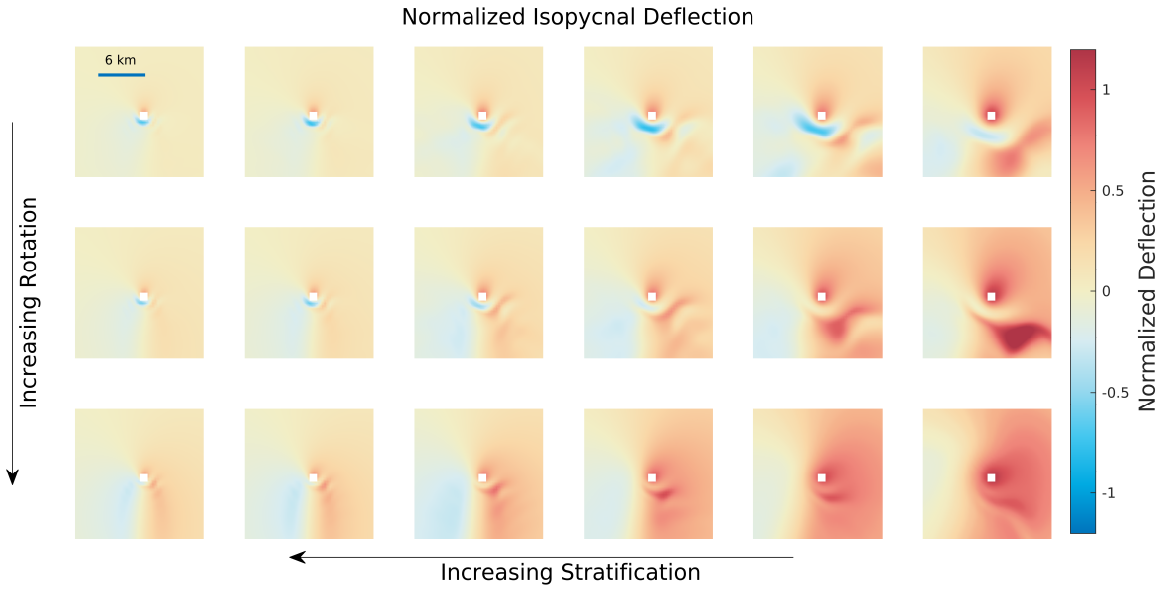

Figure 5.7: Same as Figure 5.7, except isopycnal deflections are taken at the seamount summit

prediction, qualitatively. In each plot in Fig. 5.7, the upstream side of the seamount summit (just above the center mark in each image) contains an isopycnal elevation where the flow moves over the summit. Other structures commonly appear in some simulations, such as an isopycnal trough in the lee of the summit, a meriodional tilt, and wavelike oscillations. These structures have significantly smaller length scales than those in Fig. 5.6, and may contribute to the lee waves. This possibility is addressed in Sec. 5.5.2.

We can refine the observation in Fig. 5.7 that the summit isopycnal displacement is on the order of h_c by directly calculating the actual cap height from the simulation. The actual cap height is defined as the vertical excursion from the ambient density profile, $\rho_0 + \rho_s(z)$, that is required for the densest parcel of water that is found at the summit of the seamount. For a given maximum density at the seamount summit, $\rho_{\max}$, the actual cap height is,

$$h_{\text{actual}} = \frac{(\rho_0 + \rho_s(z) - \rho_{\max}))\, g}{\rho_0 N^2}. \tag{5.28}$$

We find, in Figure 5.8a, that the peak isopycnal displacement scales only roughly as N^{-1}, as predicted by $h_c \equiv \frac{U}{N}$. When the computed isopycnal displacement is normalized by h_c, deviations from the theoretical cap height become even more apparent (see Fig. 5.8b). The actual cap height differs from the $\frac{U}{N}$ scaling by as much as $\pm 40\%$. The abscissa in Fig. 5.8b is

$$\lambda \equiv \frac{\text{Ro}}{\text{Bu}}, \tag{5.29}$$

which is defined by Perret et al. (2006) to be a scaling parameter for interface deviation in a rotating, two-layer flow past an obstacle. This quantity also appears as the ratio of the horizontal to vertical contributions to the Ertel potential vorticity (Pedlosky, 2003), and was found to play a role in eddy processes for flow past an island (Dong et al., 2007). λ is a natural choice to represent the normalized isopycnal displacement, and in Fig. 5.8b we suggest a λ-based scaling that explains the deviation from the cap model. The modified cap height, h_c^*, is defined to be,

$$h_c^* = h_c * 1.42 * \lambda^{0.15} \tag{5.30}$$

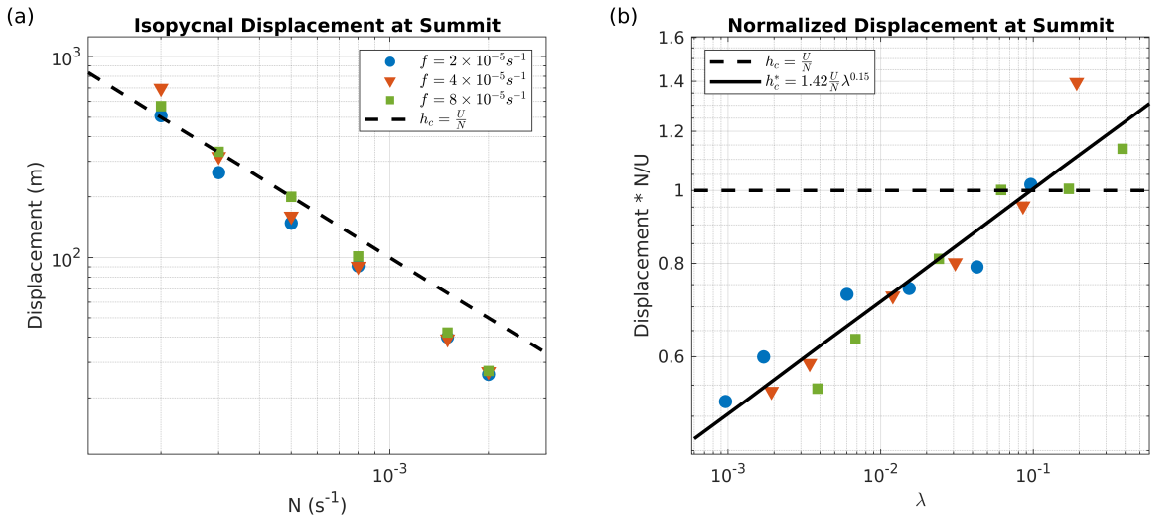

Figure 5.8: (a) The maximum isopycnal deflection at the summit is plotted against the buoyancy frequency. (b) Once normalized by the predicted cap height, the summit isopycnal deflection is plotted versus λ, a dimensionless parameter associated with isopycnal displacement.

That is, we can represent the actual cap height as the theoretical cap height, multiplied by a correction factor that is a function of λ. h_c^* can also be considered as a least squares fit to represent the h_{actual} data.

5.5.2 Revised Wave Energy Flux Estimates

The violations of the cap model, detailed above, can be accounted for by modifying the rotating Smith model. It is not immediately clear, however, whether the inaccuracies of the lee wave energy flux models in Figure 5.5 are caused by the inadequacies of the cap model. To address this, we implement three modifications to the rotating Smith model and assess their ability to improve the lee wave energy flux estimates. The modifications, in order of increasing complexity and required simulation data, are:

1. The surface of flow bifurcation is modified by using the empirical cap height from Eq. 5.30 in place of h_c. The revised $h(x, y)$ is then used in the rotating Smith model. This

method is referred to as the cap height fit Smith.

2. The cap height is computed directly from the simulation data using Eq. 5.28). This is then used to create a revised $h(x, y)$ to be input into the rotating Smith model. This method is referred to as the cap height corrected Smith.

3. The isopycnal surface that just barely reaches the seamount summit may be treated as the surface of flow bifurcation. This surface is treated as $h(x, y)$ for the rotating Smith model. The surface may therefore be asymmetric, as expected from Fig. 5.3. This method is referred to as the isopycnal Smith.

In Figure 5.9, the Smith model modifications are plotted alongside the lee wave energy flux data. The simulation data are plotted as black stars. The cap height fit Smith and the cap height corrected Smith models are plotted as blue lines and blue circles, respectively. Finally, the wave fluxes obtained from the summit isopycnals are plotted as red squares. The cap height fit tracks the simulation data quite well, and represents a relatively robust fit with respect to the cap height corrected model. The most striking aspect of this comparison is that the slope of the modeled wave flux with respect to Fr now matches the simulation data in Fig. 5.9a and b. Note that the uncorrected models all exhibited a $\mathrm{Fr}^{\frac{3}{2}}$ dependence, which underpredicted the slope of the simulation data. The cap height fit model permits the lee wave energy flux to be predicted continuously in the Froude-Rossby space, as shown in Figure 5.10. The isopycnal Smith model overestimates the energy flux in Fig. 5.9a and b, although the Froude dependence is still correctly captured. The rightmost data point in Fig. 5.9b seems to diverge from the trend set by the rest of the points, as noted in Sec. 5.4. This behavior is captured by the isopycnal Smith model, but none of the other models. This suggests that the large measured flux is due to the isopycnal structure, rather than actual cap height. In Fig. 5.9c, the isopycnal Smith model nearly perfectly captures the lee wave flux.

An additional benefit of using the measured isopycnal with the rotating Smith model is

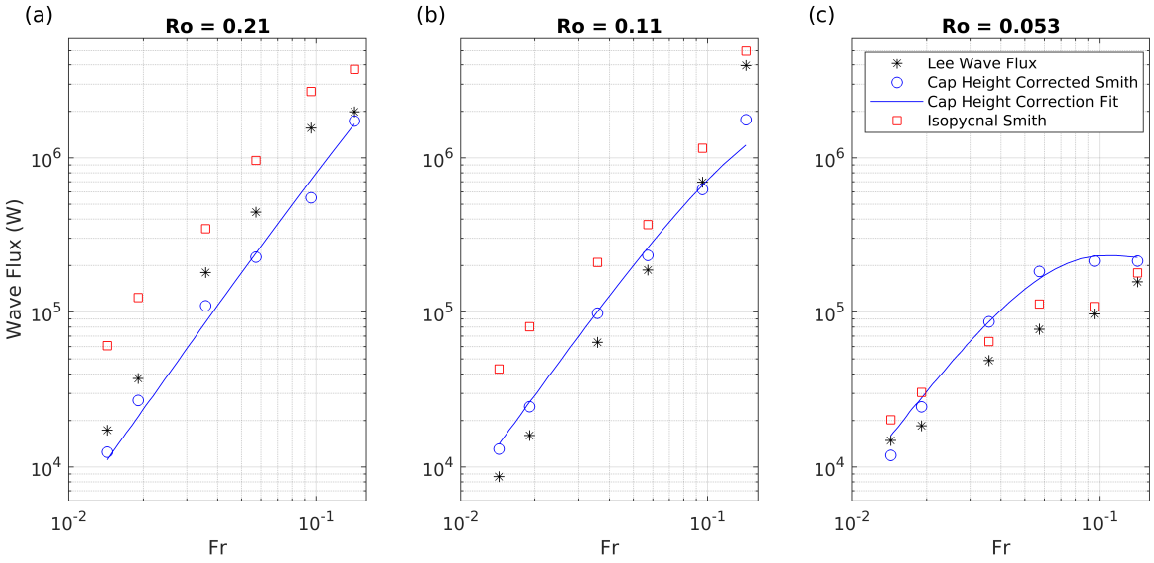

Figure 5.9: The lee wave energy flux is the same as in Figure 5.5, but now the modified Smith models are plotted alongside the simulation data. The cap height corrected Smith and cap height fit Smith models are indicated by blue circles and a solid blue line, respectively. The isopycnal Smith model is plotted using red squares.

that it permits the observed asymmetries in the isopycnal to be included in the calculated structure of the lee wave. Figure 5.11 plots three typical examples of the lee wave flux at $3h_c$ above the seamount. The simulation output, the rotating Smith with a basic cap model, and the rotating Smith with the isopycnal displacement input are all shown. While both models approximately reproduce the observed lee wave pattern when the wake is symmetric, the isopycnal input must be used to capture the full structure of the wake when strong rotation causes asymmetries.

5.6 Conclusions

Through a series of numerical simulations, we have shown that, for an isolated seamount in uniform flow, the rate that eddy energy is extracted from the mean flow significantly exceeds the rate of internal wave energy flux. These results are robust across a broad range in stratification and rotation values within the low-Froude number regime. Caution should be taken,

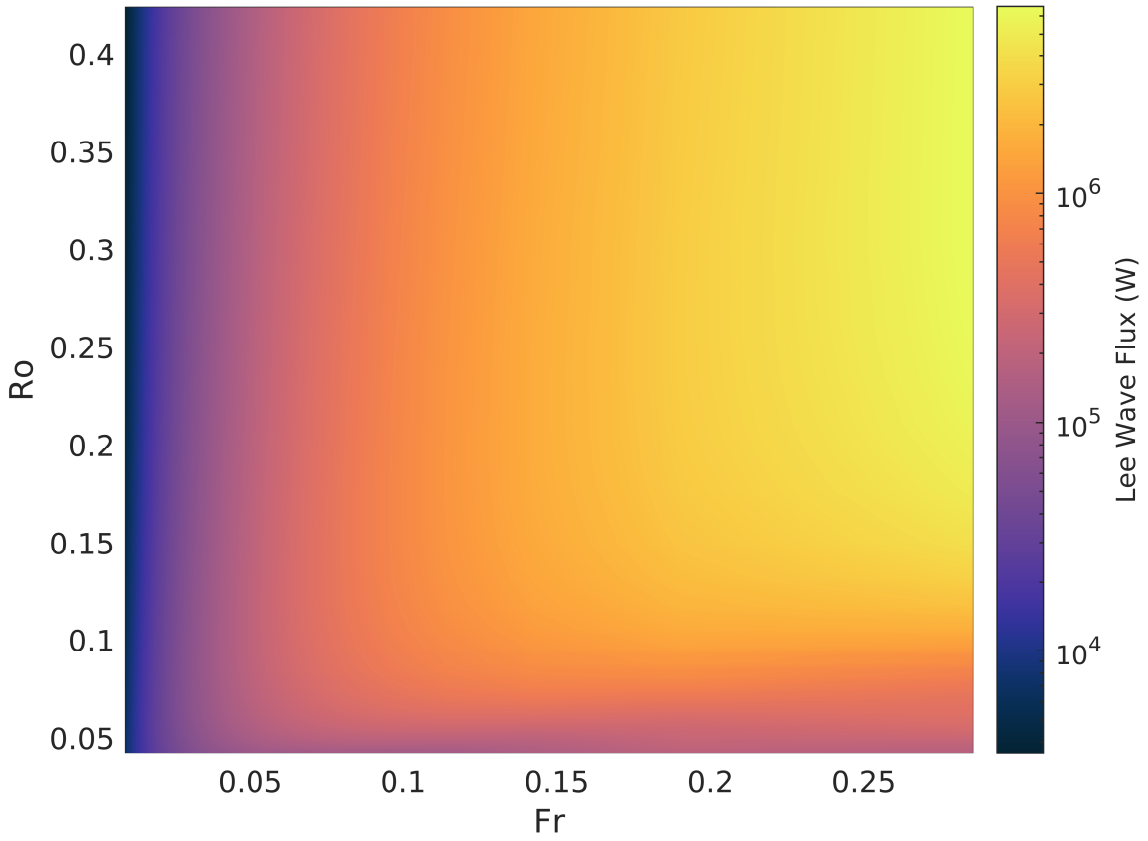

Figure 5.10: Predicted lee wave energy flux, as a function of the Froude and Rossby number, based on the cap height correction in Equation 5.30.

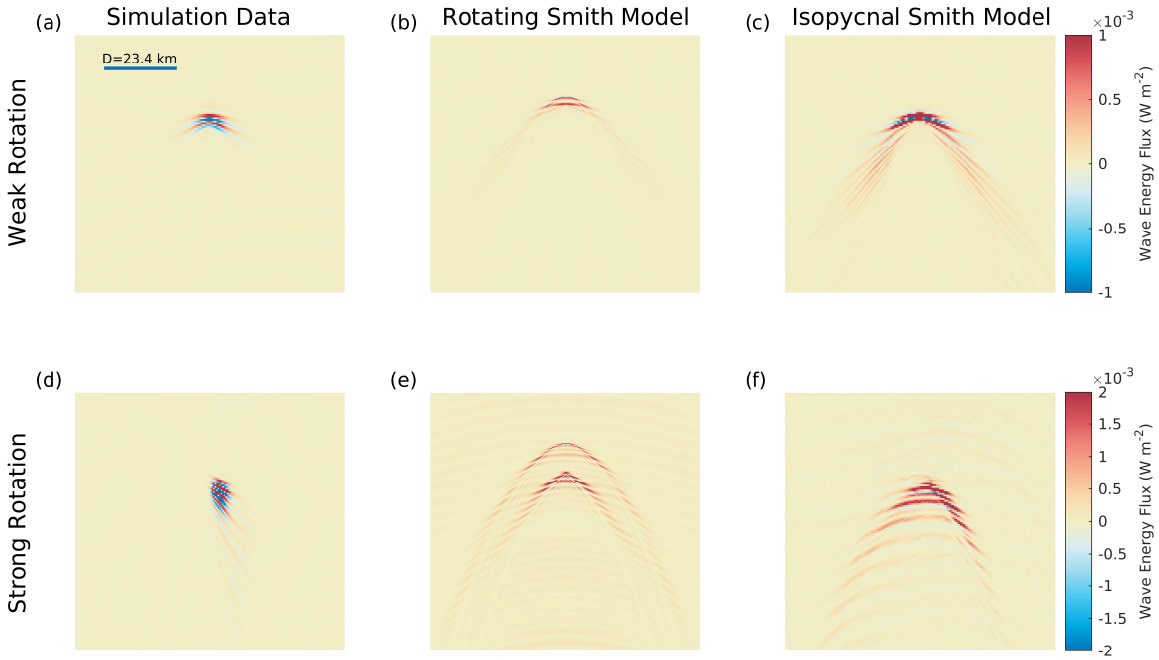

Figure 5.11: (a-c) A typical case with weak rotation. The wave flux is plotted 3 h_c above the seamount summit for the simulation data, the rotating Smith model, and the isopycnal Smith model. (d-f) Same as (a-c), except for a case with strong rotation, and an asymmetric wake.

however, in extrapolating the present study to a realistic seamount. Tidal forcing was not considered, which could enhance internal wave generation relative to eddy energy generation (Buijsman et al., 2014). Additionally, it is difficult to determine a single Froude number to describe any given seamount, because stratification and currents may have complex spatial and temporal variation, as well as considerable uncertainty in the abyssal ocean (King et al., 2012; Timko et al., 2013). But in general, slow abyssal currents and the prevalence of large seamounts (e.g., Wessel et al., 2010) suggest that a significant number of seamounts could be classified as relatively low-Froude number. We therefore highlight the possibility that some seamounts may exhibit the wake-dominated energetics seen in this study, particularly large seamounts in regions with minimal tidal forcing and strong stratification.

We show that lee wave energy flux models such as Bell (1975) and Smith (1980) can be extended to the low-Froude number regime by considering the tendency for the flow to bifurcate and only flow over the top h_c of the seamount. Both of these models, once modified, predict the same functional form in the low-Froude number limit as the explicitly low-Froude number lee wave flux model by Voisin (2007). However, these models are inadequate to describe the lee wave fluxes seen in our simulations because they do not account for rotation. Once the Smith model is extended to include rotation, the model predictions are able to capture the reduced lee wave energy flux that occurs at low-Ro. Further model improvements are obtained by correcting the cap height based on simulation data, and by replacing the surface of flow bifurcation with the simulation isopycnal that just reaches the seamount summit.

The classical view that the flow is confined to horizontal planes below the cap appears to be violated by the observed isopycnal displacement, particularly when the Rossby number is below O(0.1) (Brighton, 1978; Dalziel et al., 2011). The isopycnal deflections raise interesting questions about flow patterns around 3D topography in a rotating, stratified regime. In conjunction with work such as Dalziel et al. (2011), which looked at isopycnal deflections in the purely stratified case, there appear to be potentially important deviations from the cap height model that merit further study.

Chapter 6
SUMMARY AND FUTURE WORK

This dissertation represents an important step towards a comprehensive understanding of seamount wakes and their role in ocean mixing. The roles of stratification and rotation with respect to a seamount interacting with a uniform current have been investigated through a series of idealized numerical simulations. These simulations have yielded a description of novel vortex structures, as well as scaling laws for key energetic quantities, such as the generation of eddy energy, the internal wave flux, and the diapycnal diffusivity. Additionally, results suggest that seamount-influenced eddy processes could be a potentially overlooked mechanism for the generation of mesoscale motion, turbulence, and mixing. Several possible continuations are suggested in Section 6.2, which would extend this work to more realistic ocean conditions and include additional relevant parameters.

6.1 Summary of Work

6.1.1 Idealized Simulations

This work is primarily derived from a series of simulations conducted within the ROMS framework. The simulations each contain an isolated Gaussian seamount within a prismatic domain, subject to a uniform flow. The spatially-uniform Coriolis parameter and buoyancy frequency are altered for each simulation, resulting in a parameter sweep over an oceanographically-relevant range of Froude and Rossby numbers. Because this dissertation relies so heavily on the accuracy of the simulations, appropriate sensitivity studies and benchmarking were carried out. Sensitivity studies were conducted for grid resolution, the bottom drag formulation and drag coefficient, and turbulence model. The data obtained by Dong et al. (2007), which used a similarly idealized ROMS model, was replicated and their key

conclusions were reproduced and confirmed, adding confidence that the model was producing accurate results. A follow-up study, Dong and McWilliams (2007), substituted bathymetry and current data from the Southern California Bight in place of the idealized model inputs, and accurately reproduced observations, which further affirms that high-resolution ROMS models can provide useful information about flow conditions. Because there was not an opportunity to compare model runs to observational or experimental data, it is necessary to appeal the effectiveness of the very similar model used in Dong et al. (2007) to obtain model validation.

Overall, 35 simulations were conducted, 18 of which were used in Chapters 4 and 5. Each simulation contains approximately 80 days of simulation time, corresponding to 4 residence times for background flow within the domain. The datasets were interpolated to a Cartesian grid for further analysis.

6.1.2 Vortex Structures

A qualitative question associated with stratified flow past a 3D obstacle is what form the wake will take. We find that, despite the large Reynolds number of the flow, the effect of rotation causes the wake to manifest as a Von Kármán vortex street. We find that the vertical structure of the vortex street is determined by the Burger number. For small Burger number, which can be thought of as a rotationally-dominated flow, or one for which the baroclinic deformation radius is smaller than the length scale of the obstacle, vertically-uniform vortices are shed. Conversely, for large Burger number, the flow becomes dominated by the stratification, and the deformation radius exceeds the horizontal size of the obstacle. In this case, the vortices are vertically-independent, and shed according to the expected Strouhal number for 2D flow at that vertical level. This effect is a consequence of the relative size of the obstacle and the deformation radius. Eddies will naturally assume the length scale of the object that creates them, but the deformation radius can further restrict the eddy size. When this happens, the vertical structure of the eddy is stabilized and the eddy is vertically-uniform. These two distinct eddy regimes have consequences for the overall

energetics of seamount wakes, but are also a novel phenomenon.

6.1.3 Energetics

In order to facilitate an analysis of the energy exchange within seamount wakes, the kinetic energy within the domain was decomposed into the mean kinetic energy, unsteady eddy energy, and turbulent kinetic energy. Evolution equations were derived for each scale of motion, yielding energy exchange terms which relate the various forms of kinetic energy, the potential energy, and the viscous dissipation. Key exchange terms, such as the rate at which the mean flow is converted into eddy energy, were compared across the Froude-Rossby parameter space. It was shown that the conversion terms associated with mesoscale motions are a function of the Burger number, which is consistent with a quasigeostrophic flow regime. Conversely, conversion terms associated with turbulent processes scale with the product of the Froude and Rossby number. The amount of energy extracted from the mean flow suggests that wake effects may be significant for the parameter range and model assumptions studied.

6.1.4 Lee Wave Modeling

The relative importance seamount wakes and the internal waves that they generate were examined for an idealized, isolated seamount. Results indicate that eddy processes energetically dominate the internal wave energy flux in the case of strongly stratified, strongly rotating flow. The internal wave field was specifically examined, and partitioned into steady lee waves and unsteady wake waves. It was found that the lee wave energy flux cannot be explained by existing analytical theories. Typically, internal wave flux parameterizations are based on weakly-stratified, nonrotating, 2D linear theory, which does not apply in the regime of interest. Therefore, a lee wave model by Smith (1980) was extended into the low-Froude number regime and the effect of rotation was included. While strongly stratified experiments have previously indicated that only the top $\frac{U}{N}$ of an obstacle generates internal waves, the effect of rotation appears to modify this wavemaking height. Once the $\frac{U}{N}$ height is revised

to account for rotation, the lee wave energy flux can be reasonably accurately reproduced by the extended Smith (1980) model.

6.2 Recommendations for Future Work

This study was restricted to a single geometry and explored variations in the Rossby and Froude numbers. Other nondimensional parameters, as previously described, may play an important role in seamount wakes. Specifically, the ratio of the seamount height to the water depth (e.g., Boyer and Chen, 1987), the seamount aspect ratio (e.g., Dong et al., 2007; Srinivasan et al., 2019), and the Ekman number may all impact the seamount wake. As the seamount height approaches the water depth and the Burger number becomes small, shed eddies may extend all the way to the surface, which may have the effect of reversing the trend of the EKE decreasing as the Burger number is reduced (see Fig. 4.5a). The mechanism of vorticity generation is sensitive to the seamount aspect ratio and the Ekman number. Whereas Dong et al. (2007) studied vertical cylinders which produced vorticity primarily through viscous boundary layer separation, Srinivasan et al. (2019) simulated a seamount with a very shallow slope and invoked Ekman layer effects in their vortex formation. The present study used a similar formulation to that of Srinivasan et al. (2019); both studies, however, rely on relatively simple bottom drag parameterizations. Future work may benefit from a more refined treatment of the bottom processes. In the limiting cases of very shallow and very steep topographic slopes, the physics of eddy shedding may differ significantly, and therefore impact the overall energetics of the flow. A complete description of seamount wakes in steady flow, then, would require additional simulations with varying aspect ratios and depth ratios, as well as varying absolute seamount heights. For a very tall seamount, the bottom boundary layer is small relative to the seamount, and while the BBL physics are still an important driver in eddy formation, the effective geometry of the seamount is not significantly altered by the BBL. For a shorter seamount, the relatively large BBL may interfere with the characteristic dimensions of the seamount and it is therefore expected to greatly impact the wake. In the limiting case of abyssal hills whose height scale is of the

same order as the BBL thickness, no eddies are expected to form at all.

The flow conditions used in this study are characteristic of a large seamount in a relatively energetic and uniform current, as is found in the Antarctic Circumpolar Current. For more typical midlatitude seamounts, ocean currents will include internal tidal modes, and may even be completely dominated by them, forming purely oscillatory flow. It is arguable that a small uniform current with a larger M2 tidal ellipse included is much more characteristic of a realistic seamount. In addition, the internal waves excited by internal tides are thought to be a much more important source of wave radiation than the lee and wake waves studied in Chapter 5 (Nikurashin and Ferrari, 2009). The inclusion of tidal modes would be a much more "fair" comparison of internal wave radiation to eddy generation. Parametrically, the inclusion of tides introduces two additional dimensionless groups: the Keulegan-Carpenter number, which relates the distance a fluid element travels during a tidal period to the length scale of the seamount, and the ratio of the magnitudes of the time-averaged current and the tidal velocity. As suggested in Section 4.2, the velocity decomposition could easily be adapted to analyze motions occuring at the time-averaged, phase-averaged, and unsteady timescales. It should be noted, however, that the data storage requirements for a simulation including tides would be quite severe. Obtaining reliable data that resolves intra-tidal variations would require the field variables to be saved approximately hourly, whereas the eddy structures may evolve on timescales as slow as 30 days. As such, achieving good statistics may require saving in excess of 4000 timesteps, which at our resolution would require well over 5 TB per simulation. Such restrictions could be overcome with significant computational resources, but care should be taken in doing so.

This work raises many questions about the properties of rotating, stratified turbulence. Because ROMS relies on a two-equation model for turbulence closure, there is limited insight that can be gained from analysis of the turbulence in these simulations. It is important to note that the data in these simulations include the shortcomings that are present in the RANS model. It may be of benefit to conduct Large Eddy Simulations for a seamount that is modeled with an immersed boundary method. Such simulations, though more computationally-

intensive, would be much more authoritative for turbulence analysis.

Ultimately, the hope for this work is that it might inform mixing parameterizations for global models. In order to meaningfully contribute to these parameterizations, it is necessary to perform simulations of realistic ocean conditions and to determine how best to describe complex flow conditions such as nonuniform stratification and current profiles, realistic bathymetry, and the influence of nearby topography. Previous parameterization attempts for topographic internal waves have related the wave flux to the bathymetry spectrum with some degree of success (Klymak et al., 2010). In this case, it is likely that many factors would contribute to the wake production and wake-induced mixing. We recommend sensitivity studies as the idealized simulations are gradually adjusted towards realistic flow parameters. In addition, with a large number of stochastic seamount simulations, this type of problem could benefit from machine learning, due to the large number of input variables. As an initial step, however, the Burger number, seamount height, and inflow velocity would be a reasonable set of parameters with which to suggest a wake parameterization.

BIBLIOGRAPHY

Achenbach, E.

1972. Experiments on the flow past spheres at very high Reynolds numbers. *Journal of Fluid Mechanics*, 54(03):565.

Ahlborn, B., M. L. Seto, and B. R. Noack

2002. On drag, Strouhal number and vortex-street structure. *Fluid Dynamics Research*, 30(6):379–399.

Alford, M. H., T. Peacock, J. A. MacKinnon, J. D. Nash, M. C. Buijsman, L. R. Centuroni, S.-Y. Chao, M.-H. Chang, D. M. Farmer, O. B. Fringer, K.-H. Fu, P. C. Gallacher, H. C. Graber, K. R. Helfrich, S. M. Jachec, C. R. Jackson, J. M. Klymak, D. S. Ko, S. Jan, T. M. S. Johnston, S. Legg, I.-H. Lee, R.-C. Lien, M. J. Mercier, J. Moum, R. Musgrave, J.-H. Park, A. Pickering, R. Pinkel, L. Rainville, S. R. Ramp, D. L. Rudnick, S. Sarkar, A. Scotti, H. L. Simmons, L. C. St. Laurent, S. K. Venayagamoorthy, Y.-H. Wang, J. Wang, Y. J. Yang, T. Paluszkiewicz, and T.-Y. D. Tang

2015. The formation and fate of internal waves in the South China Sea. *Nature*, 521(7550):65–9.

Arbic, B. K. and R. B. Scott

2008. On Quadratic Bottom Drag, Geostrophic Turbulence, and Oceanic Mesoscale Eddies. *Journal of Physical Oceanography*, 38(1):84–103.

Balmforth, N. J., G. R. Ierley, and W. R. Young

2002. Tidal Conversion by Subcritical Topography. *Journal of Physical Oceanography*, 32(10):2900–2914.

Barkley, D. and R. Henderson

1996. Three-dimensional Floquet stability analysis of the wake of a circular cylinder. *J. Fluid Mech.*

Bauer, M. H., G. J. Mayr, I. Vergeiner, and H. Pichler

2000. Strongly Nonlinear Flow over and around a Three-Dimensional Mountain as a Function of the Horizontal Aspect Ratio. *Journal of the Atmospheric Sciences*, 57(24):3971–3991.

Beckmann, A. and D. B. Haidvogel

1993. Numerical Simulation of Flow around a Tall Isolated Seamount. Part I: Problem Formulation and Model Accuracy. *Journal of Physical Oceanography*, 23(8):1736–1753.

Beckmann, A. and D. B. Haidvogel

1997. A numerical simulation of flow at Fieberling Guyot. *Journal of Geophysical Research: Oceans*, 102(C3):5595–5613.

Bell, T. H.

1975. Lee waves in stratified flows with simple harmonic time dependence. *Journal of Fluid Mechanics*, 67(4):705–722.

Billant, P. and J.-M. Chomaz

2001. Self-similarity of strongly stratified inviscid flows. *Physics of Fluids*, 13(6):1645–1651.

Bonneton, P., J.-M. Chomaz, E. Hopfiliger, and M. Perrier

1996. The structure of the turbulent wake and the random internal wave field generated by a moving sphere in a stratified fluid. *Dynamics of Atmospheres and Oceans*, 23(1-4):299–308.

Bonneton, P., J.-M. Chomaz, and E. J. Hopfinger

1993. Internal waves produced by the turbulent wake of a sphere moving horizontally in a stratified fluid. *Journal of Fluid Mechanics*, 254(-1):23.

Boutov, D., A. Santos, E. Luís, and J. Videman

2010. Numerical Modeling of Vorticity Dynamics in Oceanic Wakes. In *V European Conference on Computational Fluid Dynamics*, Pp. 14–17.

Boyer, D. L. and R.-R. Chen

1987. Laboratory Simulation of Mountain Effects on Large-Scale Atmospheric Motion Systems. The Rocky Mountains. *Journal of the Atmospheric Sciences*, 44(1):100–123.

Boyer, D. L., P. A. Davies, W. R. Holland, F. Biolley, and H. Honji

1987. Stratified Rotating Flow over and around Isolated Three-Dimensional Topography. *Philosophical Transactions of the Royal Society A: Mathematical, Physical and Engineering Sciences*, 322(1564):213–241.

Brandt, A. and J. R. Rottier

2015. The internal wavefield generated by a towed sphere at low Froude number. *Journal of Fluid Mechanics*, 769:103–129.

Brighton, P. W. M.

1978. Strongly stratified flow past three dimensional obstacles. *Quarterly Journal of the Royal Meteorological Society*, 104(440):289–307.

Brink, K. H.

1990. On the generation of seamount-trapped waves. *Deep Sea Research Part A, Oceanographic Research Papers*, 37(10):1569–1582.

Brink, K. H.

1995. Tidal and lower frequency currents above Fieberling Guyot. *Journal of Geophysical Research*, 100(C6):10817.

Buijsman, M. C., J. M. Klymak, S. Legg, M. H. Alford, D. M. Farmer, J. A. MacKinnon, J. D. Nash, J.-H. Park, A. Pickering, and H. L. Simmons

2014. Three-Dimensional Double-Ridge Internal Tide Resonance in Luzon Strait. *Journal of Physical Oceanography*, 44(3):850–869.

Caldeira, M. and P. Sangrà

2012. Complex geophysical wake flows Madeira Archipelago case study. *Ocean Dynamics*, 62(62).

Callendar, W., J. M. Klymak, and M. G. G. Foreman

2011. Tidal generation of large sub-mesoscale eddy dipoles. *Ocean Science*, 7(4):487–502.

Canals, M., G. Pawlak, and P. MacCready

2009. Tilted Baroclinic Tidal Vortices. *Journal of Physical Oceanography*, 39(2):333–350.

Carter, G. S., M. C. Gregg, and M. A. Merrifield

2006. Flow and Mixing around a Small Seamount on Kaena Ridge, Hawaii. *Journal of Physical Oceanography*, 36(6):1036–1052.

Carter, G. S., M. A. Merrifield, J. M. Becker, K. Katsumata, M. C. Gregg, D. S. Luther, M. D. Levine, T. J. Boyd, and Y. L. Firing

2008. Energetics of M 2 Barotropic-to-Baroclinic Tidal Conversion at the Hawaiian Islands. *J Phys Oceanogr*, 38:2205–2223.

Castro, I. P., W. H. Snyder, and P. G. Baines

1990. Obstacle Drag in Stratified Flow. *Proc. Royal Soc. Lond.*

Chen, G., D. Wang, C. Dong, T. Zu, H. Xue, Y. Shu, X. Chu, Y. Qi, and H. Chen

2015. Observed deep energetic eddies by seamount wake. *Scientific Reports*, 5:17416.

Chen, J.-H., S.-J. Lin, J.-H. Chen, and S.-J. Lin

2013. Seasonal Predictions of Tropical Cyclones Using a 25-km-Resolution General Circulation Model. *Journal of Climate*, 26(2):380–398.

Codiga, D. L.

1993. Laboratory Realizations of Stratified Seamount-trapped Waves. *Journal of Physical Oceanography*, 23(9):2053–2071.

Coutis, P. F. and J. H. Middleton

2002. The physical and biological impact of a small island wake in the deep ocean. *Deep-Sea Research I*, 49:1341–1361.

Dalziel, S. B., M. D. Patterson, C. P. Caulfield, and S. Le Brun

2011. The structure of low-Froude-number lee waves over an isolated obstacle. *Journal of Fluid Mechanics*, 689:3–31.

Delworth, T. L., F. Zeng, G. A. Vecchi, X. Yang, L. Zhang, and R. Zhang

2016. The North Atlantic Oscillation as a driver of rapid climate change in the Northern Hemisphere. *Nature Geoscience*, 9(7):509–512.

Dong, C., Y. Cao, and J. C. McWilliams

2018. Island Wakes in Shallow Water. *Atmosphere - Ocean*, 56(2):96–103.

Dong, C. and J. C. McWilliams

2007. A numerical study of island wakes in the Southern California Bight. *Continental Shelf Research*, 27(9):1233–1248.

Dong, C., J. C. McWilliams, and A. F. Shchepetkin

2007. Island Wakes in Deep Water. *Journal of Physical Oceanography*, 37(4):962–981.

Drazin, P.

1961. On the Steady Flow of a fluid of variable density past an object. *Tellus*, 13(2).

Dritschel, D. G. and M. De La Torre Juárez

1996. The instability and breakdown of tall columnar vortices in a quasi-geostrophic fluid. *Journal of Fluid Mechanics*, 328:129–160.

Dritschel, D. G., M. De La Torre Juárez, and M. H. Ambaum

1999. The three-dimensional vortical nature of atmospheric and oceanic turbulent flows. *Physics of Fluids*, 11(6):1512–1520.

Epifanio, C. C.

2003. Lee Vortices. In *Encyclopedia of Atmospheric Sciences*, Pp. 1150–1160.

Epifanio, C. C. and R. Rotunno

2005. The Dynamics of Orographic Wake Formation in Flows with Upstream Blocking. *Journal of the Atmospheric Sciences*, 62(9):3127–3150.

Fage, A.

1936. *Experiments on a Sphere at Critical Reynolds Numbers*. H.M. Stationary Office.

Freeland, H.

1994. Ocean Circulation at and Near Cobb Seamount. *Deep-Sea Research I*, 41(11/12):1715–1732.

Gill, A. E.

1982. *Atmosphere-ocean dynamics*. Academic Press.

Gilreath, H. and A. Brandt

1985. Experiments on the generation of internal waves in a stratified fluid. *AIAA Journal*, 23(5):693–700.

Gregg, M. C., E. A. D'Asaro, J. Riley, and E. Kunze

2018. Mixing Efficiency in the Ocean. *Annual Review of Marine Science*, 10(1).

Grisouard, N. and C. Staquet

2010. Numerical simulations of the local generation of internal solitary waves in the Bay of Biscay. *Nonlinear Processes in Geophysics*, 17(5):575–584.

Gula, J., M. J. Molemaker, and J. C. McWilliams

2016. Topographic generation of submesoscale centrifugal instability and energy dissipation. *Nature Communications*, 7:12811.

Hedstrom, K.

2016. Technical Manual for a Coupled Sea-Ice/Ocean Circulation Model. Technical report, Arctic Region Supercomputing Center, Fairbanks, AK.

Hunt, J. C. R. and W. H. Snyder

1980. Experiments on stably and neutrally stratified flow over a model three-dimensional hill. *Journal of Fluid Mechanics*, 96(04):671.

Hussain, A. K. M. F. and W. C. Reynolds

1970. The mechanics of an organized wave in turbulent shear flow. *Journal of Fluid Mechanics*, 41(02):241.

Jordan, T. H., H. W. Menard, and D. K. Smith

1983. Density and size distribution of seamounts in the eastern Pacific inferred from wide-beam sounding data. *Journal of Geophysical Research: Solid Earth*, 88(B12):10508–10518.

Kadri, Y., P. Bonneton, J.-M. Chomaz, and M. Perrier

1996. Stratified flow over three-dimensional topography. *Dynamics of Atmospheres and Oceans*, 23(1-4):321–334.

Kang, D. and E. N. Curchitser

2015. Energetics of Eddy-Mean Flow Interactions in the Gulf Stream Region. *Journal of Physical Oceanography*, 45(4):1103–1120.

Kang, D., E. N. Curchitser, and A. Rosati

2016. Seasonal Variability of the Gulf Stream Kinetic Energy. *Journal of Physical Oceanography*, 46(4):1189–1207.

King, B., M. Stone, H. P. Zhang, T. Gerkema, M. Marder, R. B. Scott, and H. L. Swinney
2012. Buoyancy frequency profiles and internal semidiurnal tide turning depths in the oceans. *Journal of Geophysical Research: Oceans*, 117(C4).

Klymak, J. M., S. Legg, and R. Pinkel
2010. A Simple Parameterization of Turbulent Tidal Mixing near Supercritical Topography. *Journal of Physical Oceanography*, 40(9):2059–2074.

Kundu, P. J., I. M. Cohen, and D. R. Dowling
2004. *Fluid Mechanics*, 3rd edition. San Diego, USA: Elsevier.

Kunze, E.
2003. Yes, we have no abyssal mixing. *Near-Boundary Processes and Their Parameterizations: Proc. 'Aha Huliko'a Hawaiian Winter Workshop*, Honolulu,(1):85–93.

Kunze, E., C. MacKay, E. E. McPhee-Shaw, K. Morrice, J. B. Girton, and S. R. Terker
2012. Turbulent Mixing and Exchange with Interior Waters on Sloping Boundaries. *Journal of Physical Oceanography*, 42(6):910–927.

Kunze, E. and J. M. Toole
1997. Tidally Driven Vorticity, Diurnal Shear, and Turbulence atop Fieberling Seamount. *Journal of Physical Oceanography*, 27(12):2663–2693.

Lamb, K. G.
2014. Internal Wave Breaking and Dissipation Mechanisms on the Continental Slope/Shelf. *Annual Review of Fluid Mechanics*, 46(1):231–254.

Large, W. G., J. C. McWilliams, and S. C. Doney
1994. Oceanic vertical mixing: A review and a model with a nonlocal boundary layer parameterization. *Reviews of Geophysics*, 32(4):363.

Legg, S., B. Briegleb, Y. Chang, E. P. Chassignet, G. Danabasoglu, T. Ezer, A. L. Gordon, S. M. Griffies, R. W. Hallberg, L. Jackson, W. G. Large, T. M. Özgükmen, H. Peters,

J. Price, U. Riemenschneider, W. Wu, X. Xu, and J. Yang

2009. Improving oceanic overflow representation in climate models: The Gravity Current Entrainment Climate Process Team. *Bulletin of the American Meteorological Society*, 90(5):657–670.

Lilly, D. K.

1983. Stratified Turbulence and the Mesoscale Variability of the Atmosphere. *Journal of the Atmospheric Sciences*, 40(3):749–761.

Lin, J. T. and Y. H. Pao

1979. Wakes in Stratified Fluids. *Annual Review of Fluid Mechanics*, 11(1):317–338.

Llewellyn Smith, S. G. and W. R. Young

2003. Tidal conversion at a very steep ridge. *Journal of Fluid Mechanics*, 495(495):175–191.

Lueck, R. G.

1997. Topographically Induced Mixing Around a Shallow Seamount. *Science*, 276(5320):1831–1833.

MacCready, P., N. S. Banas, B. M. Hickey, E. P. Dever, and Y. Liu

2009. A model study of tide- and wind-induced mixing in the Columbia River Estuary and plume. *Continental Shelf Research*, 29(1):278–291.

MacCready, P. and S. N. Giddings

2016. The Mechanical Energy Budget of a Regional Ocean Model. *Journal of Physical Oceanography*, 46(9):2719–2733.

Majda, A.

2003. *Introduction to PDEs and Waves for the Atmosphere and Ocean*, volume 9. New York University, Courant Institute of Mathematical Sciences and American Mathematical Society.

Marshall, J., C. Hill, L. Perelman, and A. Adcroft

1997. Hydrostatic, quasi-hydrostatic, and nonhydrostatic ocean modeling. *Journal of Geophysical Research: Oceans*, 102(C3):5733–5752.

McCabe, R. M., P. MacCready, G. Pawlak, R. M. McCabe, P. MacCready, and G. Pawlak

2006. Form Drag due to Flow Separation at a Headland. *Journal of Physical Oceanography*, 36(11):2136–2152.

Melet, A. V., R. W. Hallberg, S. Legg, and K. L. Polzin

2013a. Sensitivity of the Ocean State to the Vertical Distribution of Internal-Tide-Driven Mixing. *Journal of Physical Oceanography*, 43(3):602–615.

Melet, A. V., M. Nikurashin, C. Muller, S. Falahat, J. Nycander, P. G. Timko, B. K. Arbic, and J. A. Goff

2013b. Internal tide generation by abyssal hills using analytical theory. *Journal of Geophysical Research: Oceans*, 118(11):6303–6318.

Meunier, P.

2012. Stratified wake of a tilted cylinder. Part 2. Lee internal waves. *Journal of Fluid Mechanics*, 699(April):198–215.

Meunier, P., S. Le Dizès, L. Redekopp, and G. R. Spedding

2018. Internal waves generated by a stratified wake: experiment and theory. *Journal of Fluid Mechanics*, 846:752–788.

Munk, W.

1966. Abyssal Recipes. *Deep-Sea Research*, 13:707–730.

Munk, W. and C. Wunsch

1998. Abyssal recipes II. *Deep-Sea Research I*, 45:1977–2010.

Naveira Garabato, A. C., R. Ferrari, and K. L. Polzin

2011. Eddy stirring in the Southern Ocean. *Journal of Geophysical Research: Oceans*, 116(9):C09019.

Nikurashin, M. and R. Ferrari

2009. Radiation and Dissipation of Internal Waves Generated by Geostrophic Motions Impinging on Small-Scale Topography: Application to the Southern Ocean. *Journal of Physical Oceanography*, 40(5):2025–2042.

Nikurashin, M. and R. Ferrari

2011. Global energy conversion rate from geostrophic flows into internal lee waves in the deep ocean. *Geophysical Research Letters*, 38(8):1–6.

Nikurashin, M. and R. Ferrari

2013. Overturning circulation driven by breaking internal waves in the deep ocean. *Geophysical Research Letters*, 40(12):3133–3137.

Osborn, T. R.

1980. Estimates of the Local Rate of Vertical Diffusion from Dissipation Measurements. *Journal of Physical Oceanography*, 10(1):83–89.

Otheguy, P., P. Billant, and J. M. Chomaz

2006. The effect of planetary rotation on the zigzag instability of co-rotating vortices in a stratified fluid. *Journal of Fluid Mechanics*, 553:273–281.

Pedlosky, J.

1987. *Geophysical Fluid Dynamics*. New York, NY: Springer New York.

Pedlosky, J.

2003. WKB Theory for Internal Gravity Waves. In *Waves in the Ocean and Atmosphere*, Pp. 75–89. Berlin, Heidelberg: Springer Berlin Heidelberg.

Perfect, B., N. Kumar, and J. Riley

2018. Vortex Structures in the Wake of an Idealized Seamount in Rotating, Stratified Flow. *Geophysical Research Letters*, 45(17):9098–9105.

Perfect, B., N. Kumar, and J. Riley

2019a. Energetic of Seamount Wakes, Part 1 : Energy Exchange. *Journal of Physical Oceanography*, submitted.

Perfect, B., N. Kumar, and J. Riley

2019b. Energetics of Seamount Wakes , Part 2 : Wave Fluxes. *Journal of Physical Oceanography*, submitted.

Perret, G., A. Stegner, M. Farge, and T. Pichon

2006. Cyclone-anticyclone asymmetry of large-scale wakes in the laboratory. *Physics of Fluids*, 18(3):036603.

Phillips, O. M.

1966. *The Dynamics of the Upper Ocean*. Cambridge, U.K.: Cambridge University Press.

Polzin, K. L., J. M. Toole, J. R. Ledwell, and R. W. Schmitt

1997. Spatial Variability of Turbulent Mixing in the Abyssal Ocean. *Science*, 276(5309).

Praud, O., J. Sommeria, and A. M. Fincham

2006. Decaying grid turbulence in a rotating stratified fluid. *Journal of Fluid Mechanics*, 547(-1):389.

Raja, K.

2018. *Internal waves and mean flow in the presence of topography*. PhD thesis, Université Grenoble Alpes.

Richards, K. J., E. J. Hopfinger, and G. C. Dhières

1992. Boundary-layer separation of rotating flows past surface-mounted obstacles. *Journal of Fluid Mechanics*, 237:343–371.

Riley, J. and M. P. Lelong

2000. Fluid Motions in the Presence of Strong Stable Stratification. *Annual Review of Fluid Mechanics*, 32(1):613–657.

Riley, J., H. Liu, and F. Geller

1976. A Numerical and Experimental Study of Stably Stratified Flow Around Complex Terrain. Technical report, Environmental Protection Agency, Washington, DC.

Robertson, R.

2006. Modeling internal tides over Fieberling Guyot: Resolution, parameterization, performance. *Ocean Dynamics*, 56(5-6):430–444.

Roden, G. I.

1991. Mesoscale flow and thermohaline structure around Fieberling seamount. *Journal of Geophysical Research*, 96(C9):16653.

Rogers, A.

1994. The Biology of Seamounts. *Advances in Marine Biology*, 30:305–350.

Schär, C. and D. R. Durran

1997. Vortex Formation and Vortex Shedding in Continuously Stratified Flows past Isolated Topography. *Journal of the Atmospheric Sciences*, 54:534–554.

Schär, C. and R. B. Smith

1993a. Shallow-Water Flow past Isolated Topography. Part I: Vorticity Production and Wake Formation. *Journal of the Atmospheric Sciences*, 50(10):1373–1400.

Schär, C. and R. B. Smith

1993b. Shallow-Water Flow past Isolated Topography. Part II: Transition to Vortex Shedding. *Journal of the Atmospheric Sciences*, 50(10):1401–1412.

Schiermeier, Q.

2007. Oceanography: Churn, churn, churn. *Nature*, 447(7144):522–524.

Shchepetkin, A. F.

2003. A method for computing horizontal pressure-gradient force in an oceanic model with a nonaligned vertical coordinate. *Journal of Geophysical Research*, 108(C3):3090.

Shchepetkin, A. F. and J. C. McWilliams

2005. The Regional Ocean Modeling System: A split-explicit, free-surface, topography following coordinates ocean model. *Ocean Modelling*, 9:347–404.

Sheppard, P.

1956. Airflow over mountains. *Quarterly Journal of the Royal Meteorological Society*, 82(354):528–529.

Smith, R. B.

1980. Linear theory of stratified hydrostatic flow past an isolated mountain. *Tellus*, 32(4):348–364.

Smolarkiewicz, P. K. and R. Rotunno

1989. Low Froude Number Flow Past Three-Dimensional Obstacles. Part I: Baroclinically Generated Lee Vortices. *Journal of the Atmospheric Sciences*, 46(8):3611–3613.

Smyth, W. D. and J. Moum

2008. Three-Dimensional (3D) Turbulence. In *Encyclopedia of Ocean Sciences: Second Edition*, Pp. 18–25.

Spedding, G. R.

1997. The evolution of initially turbulent bluff-body wakes at high internal Froude number. *Journal of Fluid Mechanics*, 337:283–301.

Srinivasan, K., J. C. McWilliams, M. J. Molemaker, and R. Barkan

2019. Submesoscale Vortical Wakes in the Lee of Topography. *Journal of Physical Oceanography*.

St. Laurent, L. C. and C. Garrett

2002. The Role of Internal Tides in Mixing the Deep Ocean. *Journal of Physical Oceanography*, 32(10):2882–2899.

St. Laurent, L. C., S. Stringer, C. Garrett, and D. Perrault-Joncas

2003. The generation of internal tides at abrupt topography. *Deep-Sea Research Part I: Oceanographic Research Papers*, 50(8):987–1003.

Stegner, A. and D. G. Dritschel

2000. A Numerical Investigation of the Stability of Isolated Shallow Water Vortices. *Journal of Physical Oceanography*, 30(10):2562–2573.

Timko, P. G., B. K. Arbic, J. G. Richman, R. B. Scott, E. J. Metzger, and A. J. Wallcraft

2013. Skill testing a three-dimensional global tide model to historical current meter records. *Journal of Geophysical Research: Oceans*, 118(12):6914–6933.

Toole, J. M., R. W. Schmitt, K. L. Polzin, and E. Kunze

1997. Near-boundary mixing above the flanks of a midlatitude seamount. *Journal of Geophysical Research: Oceans*, 102(C1):947–959.

Umlauf, L. and H. Burchard

2003. A generic length-scale equation for geophysical turbulence models. *Journal of Marine Research*, 61(2):235–265.

Vallis, G. K.

2006. *Atmospheric and Oceanic Fluid Dynamics*. Cambridge, U.K.: Cambridge University Press.

Voisin, B.

1991. Internal wave generation in uniformly stratified fluids. Part 1. Green's function and point sources. *Journal of Fluid Mechanics*, 231(-1):439.

Voisin, B.

2007. Lee waves from a sphere in a stratified flow. *Journal of Fluid Mechanics*, 574:273–315.

Vosper, S. B., I. P. Castro, W. H. Snyder, and S. D. Mobbs

1999. Experimental studies of strongly stratified flow past three-dimensional orography. *J. Fluid Mech*, 390:223–249.

Warner, J. C., C. R. Sherwood, H. G. Arango, and R. P. Signell

2005. Performance of four turbulence closure models implemented using a generic length scale method. *Ocean Modelling*, 8:81–113.

Warner, S. J. and P. MacCready

2014. The dynamics of pressure and form drag on a sloping headland: Internal waves versus eddies. *Journal of Geophysical Research: Oceans*, 119(3):1554–1571.

Waterhouse, A. F., J. A. MacKinnon, J. D. Nash, M. H. Alford, E. Kunze, H. L. Simmons, K. L. Polzin, L. C. St. Laurent, O. M. Sun, R. Pinkel, L. D. Talley, C. B. Whalen, T. N. Huussen, G. S. Carter, I. Fer, S. Waterman, A. C. Naveira Garabato, T. B. Sanford, C. M. Lee, and A. N. Garabato

2014. Global Patterns of Diapycnal Mixing from Measurements of the Turbulent Dissipation Rate. *Journal of Physical Oceanography*, 44(7):1854–1872.

Wessel, P., D. Sandwell, and S.-S. Kim

2010. The Global Seamount Census. *Oceanography*.

Whalen, C. B., L. D. Talley, and J. A. MacKinnon

2012. Spatial and temporal variability of global ocean mixing inferred from Argo profiles. *Geophysical Research Letters*, 39(17):1–6.

Williams, P. D., P. L. Read, and T. W. Haine

2010. Testing the limits of quasi-geostrophic theory: Application to observed laboratory flows outside the quasi-geostrophic regime. *Journal of Fluid Mechanics*, 649:187–203.

Winters, K. B., P. N. Lombard, J. Riley, and E. A. D'Asaro

1995. Available potential energy and mixing in density-stratified fluids. *Journal of Fluid Mechanics*, 289(C5):115–128.

Wright, C. J., R. B. Scott, P. Ailliot, and D. Furnival

2014. Lee wave generation rates in the deep ocean. *Geophysical Research Letters*, 41(7):2434–2440.

Zdravkovich, M. M.

1997. *Flow Around Circular Cylinders: A Comprehensive Guide Through Flow Phenomena, Experiments, Applications, Mathematical Models, and Computer Simulations*, volume 1.

Zhang, L., M. C. Buijsman, E. Comino, and H. L. Swinney

2017. Internal wave generation by tidal flow over periodically and randomly distributed seamounts. *Journal of Geophysical Research: Oceans*, 122(6):5063–5074.

Appendix A

ENERGY EQUATIONS DERIVATION

We present a more detailed derivation of equations 4.9-4.11.

The definitions and shorthand described in equations 4.1-4.3 are used here as well.

A.1 Derivation of the Momentum Equations

The Navier-Stokes equations for a rotating, Boussinesq fluid may be written, and then averaged according using $\langle(\cdot)\rangle$, the traditional ensemble or probability average used in turbulence modeling, which in this case can be considered to be a time average over a time on the order of the numerical time-step, and $\bar{(\cdot)}$, a time average over a time much greater than that of the large-scale unsteady motions. The momentum equations for the time-averaged, eddy unsteady, and turbulent timescales can be assembled according to Equation 4.1. The overall momentum equation is,

$$\frac{\partial u_i}{\partial t} + u_j \frac{\partial u_i}{\partial x_j} = -\frac{\partial \phi}{\partial x_i} + 2\nu \frac{\partial s_{ij}}{\partial x_j} - 2\epsilon_{ijk}\Omega_j u_k + b\delta_{i3} \tag{A.1}$$

Only the nonlinear advective term, $u_j \frac{\partial u_i}{\partial x_j}$, produces unintuitive results when subjected to an averaging operator. For that reason, it is addressed directly.

$$\begin{aligned}
\overline{u_j \frac{\partial u_i}{\partial x_j}} &= \overline{\bar{U}_j \frac{\partial \bar{U}_i}{\partial x_j} + \underbrace{\bar{u}_j \frac{\partial (\hat{u}+u')_i}{\partial x_j} + (\hat{u}+u')_j \frac{\partial \bar{u}_i}{\partial x_j}}_{=0} + (\hat{u}+u')_j \frac{\partial (\hat{u}+u')_i}{\partial x_j}} \\
&= \bar{U}_j \frac{\partial \bar{U}_i}{\partial x_j} + \frac{\partial}{\partial x_j} \overline{(\hat{u}+u')_i (\hat{u}+u')_j} \\
&= \bar{U}_j \frac{\partial \bar{U}_i}{\partial x_j} + \frac{\partial}{\partial x_j} \left(\bar{R}_{ij} + \bar{T}_{ij} \right)
\end{aligned} \tag{A.2}$$

Similarly,

$$\begin{aligned}\left\langle u_j \frac{\partial u_i}{\partial x_j} \right\rangle &= \left\langle u'_j \frac{\partial u'_i}{\partial x_j} + \underbrace{u'_j \frac{\partial (\hat{u}+\bar{U})_i}{\partial x_j} + (\hat{u}+\bar{U})_j \frac{\partial u'_i}{\partial x_j}}_{=0} + (\hat{u}+\bar{U})_j \frac{\partial (\hat{u}+\bar{U}_j)}{\partial x_j} \right\rangle \\ &= (\hat{u}+\bar{U})_j \frac{\partial (\hat{u}+\bar{U})_i}{\partial x_j} + \frac{\partial}{\partial x_j} \left\langle u'_i u'_j \right\rangle \\ &= U_j \frac{\partial U_i}{\partial x_j} + \frac{\partial}{\partial x_j} R_{ij}\end{aligned} \tag{A.3}$$

Using Eq. A.1, Eq. 4.1, and the advective terms calculated in Equations A.2 and A.3, the three momentum equations are:

$$\underbrace{\frac{\partial \bar{U}_i}{\partial t}}_{=0} + \underbrace{\bar{U}_j \frac{\partial \bar{U}_i}{\partial x_j}}_{1} = -\frac{\partial}{\partial x_j}\left(\bar{\Phi}\delta_{ij} - 2\nu \frac{\partial \bar{S}_{ij}}{\partial x_j} + \bar{R}_{ij} + \bar{T}_{ij}\right) - 2\epsilon_{ijk}\Omega_j \bar{U}_k + \bar{B}\delta_{i3} \tag{A.4}$$

$$\frac{\partial \hat{u}_i}{\partial t} + \underbrace{\bar{U}_j \frac{\partial \hat{u}_i}{\partial x_j}}_{2} = -\frac{\partial}{\partial x_j}\left(\underbrace{\hat{u}_i \hat{u}_j}_{3} + \hat{\phi}\delta_{ij} - 2\nu \hat{s}_{ij} + \hat{R}_{ij} - \bar{T}_{ij}\right) - \underbrace{\hat{u}_j \frac{\partial \bar{U}_i}{\partial x_j}}_{4} - 2\epsilon_{ijk}\Omega_j \hat{u}_k + \hat{b}\delta_{i3} \tag{A.5}$$

$$\frac{\partial u'_i}{\partial t} + \underbrace{U_j \frac{\partial u'_i}{\partial x_j}}_{5,6} = -\frac{\partial}{\partial x_j}\left(\phi'\delta_{ij} + \underbrace{u'_i u'_j}_{7} - 2\nu s'_{ij} - R_{ij}\right) - \underbrace{u'_j \frac{\partial U_i}{\partial x_j}}_{8,9} - 2\epsilon_{ijk}\Omega_j u'_k + b'\delta_{i3} \tag{A.6}$$

Note that the original Eq A.1 can be recovered by summing the above three equations. The decompositions in b, ϕ, s_{ij}, and the time and rotation terms are recovered trivially. The nine advective acceleration terms originating from the triple decomposition have been indicated, and when summed together, they are equal to the original advection term $u_j \frac{\partial u_i}{\partial x_j}$. The Reynolds stress terms cancel, using Eq 4.7. Therefore, this trio of equations represents the momentum equation, decomposed into equations for the three scales of motion that we are considering.

A.2 Derivation of the Energy Equations

To obtain the energy form of these equations, we dot the equation in $\bar{U}_i$ with $\bar{U}_i$, the equation in $\hat{u}_i$ with $\hat{u}_i$, and the equation in u'_i with u'_i. For the mean flow, the time derivative, while still equal to zero, is included for the purposes of illustrating the kinetic energy term.

A.2.1 Special Cases for Terms

The rotation terms will vanish when the index summation is carried out. Because the rotation vector is only in the vertical ($\hat{k}$) direction, the Levi Civita yields only two nonzero terms. The x-contribution evaluates as $-fuv\epsilon_{yxz}\hat{\mathbf{z}} = fuv$. The y-contribution is $-fvu\epsilon_{xyz}\hat{\mathbf{z}} = -fuv$. These two contributions trivially cancel.

The viscous term is treated as follows:

$$2\nu u_i \frac{\partial s_{ij}}{\partial x_j} = \frac{\partial}{\partial x_j}\left(2\nu u_i s_{ij}\right) - 2\nu s_{ij}\frac{\partial u_i}{\partial x_j} \tag{A.7}$$

$$= \frac{\partial}{\partial x_j}\left(2\nu u_i s_{ij}\right) - 2\nu s_{ij} s_{ij} \tag{A.8}$$

The pressure term is rewritten so that it may be grouped with the spatial redistribution terms below:

$$-\frac{\bar{u_j}}{\rho_0}\frac{\partial \bar{P}}{\partial x_j} = -\frac{\bar{u_j}}{\rho_0}\frac{\partial \bar{P}\delta_{ij}}{\partial x_i} = \frac{\partial}{\partial x_i}\left(-\frac{\bar{u_j}}{\rho_0}\bar{P}\delta_{ij}\right) \tag{A.9}$$

A.2.2 Mean Flow Kinetic Energy

After the dot product operation, the mean flow kinetic energy equation is,

$$\bar{U}_i\frac{\partial \bar{U}_i}{\partial t} + \bar{U}_i\bar{U}_j\frac{\partial \bar{U}_i}{\partial x_j} = -\bar{U}_i\frac{\partial}{\partial x_j}\left(\bar{\Phi}\delta_{ij} - 2\nu\frac{\partial \bar{S}_{ij}}{\partial x_j} + \bar{R}_{ij} + \bar{T}_{ij}\right) - 2\bar{U}_i\epsilon_{ijk}\Omega_j\bar{U}_k + \bar{U}_i\bar{B}\delta_{i3}. \tag{A.10}$$

The special cases outlined above are applied, and the second term is moved inside the divergence operator, yielding

$$\underbrace{\frac{\partial}{\partial t}\frac{1}{2}U_i^2}_{=0} = -\frac{\partial}{\partial x_j}\left(\bar{U}_i\bar{\Phi} + 2\nu\bar{U}_i\bar{S}_{ij} + \bar{U}_i\bar{R}_{ij} + \bar{U}_i\bar{T}_{ij} - \frac{1}{2}\bar{U}_j\bar{U}_i^2\right)$$

$$- 2\nu\bar{S}_{ij}\bar{S}_{ij} + \bar{R}_{ij}\frac{\partial \bar{U}_i}{\partial x_j} + \bar{T}_{ij}\frac{\partial \bar{U}_i}{\partial x_j} + \bar{U}_3\bar{B}. \tag{A.11}$$

A.2.3 Eddy Kinetic Energy

By the same procedure, the (time-averaged) eddy kinetic energy equation is,

$$\frac{\partial}{\partial t}\frac{1}{2}\hat{u}_i^2 = -\frac{\partial}{\partial x_j}\left(\hat{\phi}\hat{u}_j - 2\nu\hat{u}_i\hat{s}_{ij} + \frac{1}{2}\hat{u}_j(\hat{u}_i^2) + \frac{1}{2}\bar{U}_j\hat{u}_i^2\right) - \hat{u}_i\hat{u}_j\frac{\partial\bar{U}_i}{\partial x_j} - \hat{u}_i\frac{\partial\hat{R}_{ij}}{\partial x_j} + \hat{u}_i frac\partial\bar{T}_{ij}\partial x_j - 2\nu\hat{s}_{ij}\hat{s}_{ij} + \hat{b}\hat{u}_3 \tag{A.12}$$

$$\frac{\partial}{\partial t}\frac{1}{2}\hat{u}_i^2 = -\frac{\partial}{\partial x_j}\left(\hat{\phi}\hat{u}_j - 2\nu\hat{u}_i\hat{s}_{ij} + \frac{1}{2}\hat{u}_j(\hat{u}_i^2) + \frac{1}{2}\bar{U}_j\hat{u}_i^2 + \hat{u}_i\hat{R}_{ij}\right) - \hat{u}_i\hat{u}_j\frac{\partial\bar{U}_i}{\partial x_j} - \hat{R}_{ij}\frac{\partial\hat{u}_i}{\partial x_j} + \hat{u}_i\frac{\partial\bar{T}_{ij}}{\partial x_j} - 2\nu\hat{s}_{ij}\hat{s}_{ij} + \hat{b}\hat{u}_3 \tag{A.13}$$

This equation is time-averaged in order to be compared on a one-to-one basis with the mean flow kinetic energy equation:

$$\underbrace{\frac{\partial}{\partial t}\frac{1}{2}\overline{\hat{u}_i^2}}_{=0} = -\frac{\partial}{\partial x_j}\left(\overline{\hat{\phi}\hat{u}_j} - 2\nu\overline{\hat{u}_i\hat{s}_{ij}} + \frac{1}{2}\overline{U_j\hat{u}_i^2} + \overline{\hat{u}_i\hat{R}_{ij}}\right) - \bar{T}_{ij}\frac{\partial\bar{U}_i}{\partial x_j} + \overline{\hat{R}_{ij}\frac{\partial\hat{u}_i}{\partial x_j}} - 2\nu\overline{\hat{s}_{ij}\hat{s}_{ij}} + \overline{\hat{b}\hat{u}_3} \tag{A.14}$$

A.2.4 Turbulent Kinetic Energy

Finally, the time-averaged TKE equation is, The TKE equation is derived by multiplying the momentum equation in u_i by u_i and ensemble averaging the result, noting that $k = \frac{1}{2}\langle u_i' u_i'\rangle$. The final result is then time averaged.

$$\frac{\partial k}{\partial t} + U_j\frac{\partial k}{\partial x_j} = -\frac{\partial}{\partial x_j}\left(\langle\phi' u_j'\rangle + \frac{1}{2}\langle u_j'(u_i'u_i')\rangle - 2\nu\langle u_i' s_{ij}'\rangle\right) - R_{ij}\frac{\partial U_i}{\partial x_j} - 2\nu\langle s_{ij}' s_{ij}'\rangle + \langle b' u_3'\rangle \tag{A.15}$$

Once again, to compare this equation on a one-to-one basis with the other energy equations, we time average, yielding,

$$\underbrace{\frac{\partial\bar{k}}{\partial t}}_{=0} = -\frac{\partial}{\partial x_j}\left(\overline{\langle\phi' u_j'\rangle} + \frac{1}{2}\overline{\langle u_j' u_i'^2\rangle} - 2\nu\overline{\langle u_i' s_{ij}'\rangle} + \bar{U}_j\bar{k} + \overline{\hat{u}_j\hat{k}}\right) - \bar{R}_{ij}\frac{\partial\bar{U}_i}{\partial x_j} - \overline{\hat{R}_{ij}\frac{\partial\hat{u}_i}{\partial x_j}} - 2\nu\langle s_{ij}' s_{ij}'\rangle + \overline{\langle b' u_3'\rangle} \tag{A.16}$$

Note that the term that becomes E_3 and E_4 could be under a single average, but it is broken apart to show the exchange terms.

A.3 Integral Form of the Energy Equations

Consider the integral over the computational volume $\mathcal{V}$ of Eq A.11, Eq A.14, and Eq A.16.

$$\int_{\mathcal{V}} \left\{ \frac{\partial}{\partial x_j} \left(\bar{U}_j \frac{1}{2} \bar{U}_i^2 + \bar{\Phi} \bar{U}_j - 2\nu \bar{U}_i \bar{S}_{ij} + \bar{U}_i \bar{R}_{ij} + \bar{U}_i \bar{T}_{ij} \right) \right\} d\mathcal{V} = \int_{\mathcal{V}} \left\{ \underbrace{\bar{R}_{ij} \frac{\partial \bar{U}_i}{\partial x_j}}_{MT} + \underbrace{\bar{T}_{ij} \frac{\partial \bar{U}_i}{\partial x_j}}_{ME} - \underbrace{2\nu \bar{S}_{ij} \bar{S}_{ij}}_{MV} + \underbrace{\bar{B} \bar{U}_3}_{MB} \right\} d\mathcal{V}, \quad \text{(A.17)}$$

or, using the divergence theorem,

$$\int_{\mathcal{S}} \left(\frac{1}{2} \bar{U}_j \bar{U}_i^2 + \bar{\Phi} \bar{U}_j - 2\nu \bar{U}_i \bar{S}_{ij} + \bar{U}_i \bar{R}_{ij} + \bar{U}_i \bar{T}_{ij} \right) n_j d\mathcal{S} = \int_{\mathcal{V}} \left\{ \underbrace{\bar{R}_{ij} \frac{\partial \bar{U}_i}{\partial x_j}}_{MT} + \underbrace{\bar{T}_{ij} \frac{\partial \bar{U}_i}{\partial x_j}}_{ME} - \underbrace{2\nu \bar{S}_{ij} \bar{S}_{ij}}_{MV} + \underbrace{\bar{B} \bar{U}_3}_{MB} \right\} d\mathcal{V}. \quad \text{(A.18)}$$

The same procedure is used for the time averaged eddy kinetic energy and turbulent kinetic energy equations. The integral form of Eq A.14 is:

$$\int_{\mathcal{S}} \left(\frac{1}{2} \overline{U_j \hat{u}_i^2} + \overline{\hat{\phi} \hat{u}_j} - 2\nu \overline{\hat{u}_i \hat{s}_{ij}} + \overline{\hat{u}_i \hat{R}_{ij}} \right) n_j d\mathcal{S} = \int_{\mathcal{V}} \left\{ \underbrace{- \bar{T}_{ij} \frac{\partial \bar{U}_i}{\partial x_j}}_{ME} + \underbrace{\overline{\hat{R}_{ij} \frac{\partial \hat{u}_i}{\partial x_j}}}_{ET} - \underbrace{2\nu \overline{\hat{s}_{ij} \hat{s}_{ij}}}_{EV} + \underbrace{\overline{\hat{b} \hat{u}_3}}_{EB} \right\} d\mathcal{V} \,. \quad \text{(A.19)}$$

Finally, the integral form of Eq A.16 is:

$$\int_{\mathcal{S}} \left(\overline{U_j k} + \overline{\langle \phi' u_j' \rangle} - 2\nu \overline{\langle u_i' s_{ij}' \rangle} + \frac{1}{2} \overline{\langle u_j' u_i'^2 \rangle} \right) n_j d\mathcal{S} = \int_{\mathcal{V}} \left\{ \underbrace{- \bar{R}_{ij} \frac{\partial \bar{U}_i}{\partial x_j}}_{MT} - \underbrace{\overline{\hat{R}_{ij} \frac{\partial \hat{u}_i}{\partial x_j}}}_{ET} - \underbrace{2\nu \overline{\langle s_{ij}' s_{ij}' \rangle}}_{TV} + \underbrace{\overline{\langle b' u_3' \rangle}}_{TB} \right\} d\mathcal{V} \,. \quad \text{(A.20)}$$

Appendix B

LEE WAVE ISOPYCNAL DISPLACEMENT EQUATIONS

Consider a perturbation expansion about steady, geostrophic wind. The basic state is a geostrophically-balanced uniform flow of U in the $\hat{x}$ direction, and there exists a small perturbation about this basic state, caused by a small topographic perturbation. The steady equations, written in a stationary frame as the flow moves past a fixed bathymetric perturbation are,

$$Uu_x - fv = -\frac{1}{\rho_0}p_x \tag{B.1}$$

$$Uv_x + fu = -\frac{1}{\rho_0}p_y \tag{B.2}$$

$$\rho_0 U w_x = -p_z - \bar{\rho}g \tag{B.3}$$

$$u_x + v_y + w_z = 0 \tag{B.4}$$

$$U\bar{\rho}_x = -w\frac{d\rho_s}{dz} \tag{B.5}$$

$$\tag{B.6}$$

where subscripts are taken to be derivatives and the lower case variables represent the fluctuating quantities. We also introduce an isopycnal displacement variable, η. The isopycnal displacement has a governing equation,

$$\bar{\rho} = \frac{\rho_0 N^2}{g}\eta. \tag{B.7}$$

Eq. B.7, in conjunction with Eq. B.5, yields,

$$w = U\eta_x. \tag{B.8}$$

The horizontal Laplacian of the velocity equation, $\frac{\partial}{\partial x}(B.1) + \frac{\partial}{\partial y}(B.2)$ yields,

$$U\left(u_x + v_y\right)_x - f\left(v_x - u_y\right) = -\frac{1}{\rho_0}\nabla_H p. \tag{B.9}$$

Using the incompressibility, Eq. B.4, and defining a vertical vorticity, $\xi = v_x - u_y$, this equation becomes:

$$\xi = \frac{1}{\rho_0 f}\nabla_H p - \frac{U}{f} w_{xz}. \tag{B.10}$$

Next, taking $\frac{\partial}{\partial y}(B.1) - \frac{\partial}{\partial x}(B.2)$, we obtain,

$$U\left(u_y - v_x\right)_x - f\left(v_y + u_x\right) = 0 \tag{B.11}$$

$$-U\xi_x + f w_z = 0. \tag{B.12}$$

We may eliminate ξ by combining Equations B.10 and B.12:

$$-U\frac{1}{\rho_0}\left(\nabla_H^2\right)_x + U^2 w_{xxz} + f^2 w_z = 0. \tag{B.13}$$

Next, we can eliminate $\bar{\rho}$ from Equations B.3 and B.8, yielding:

$$\rho_0 U w_z = -p_z - \rho_0 N^2 \eta. \tag{B.14}$$

By differentiating Eq. B.13 with respect to z and eliminating p_z using B.14, we obtain

$$-U^2\left(\nabla_H^2 w\right)_{xx} - UN^2\left(\nabla_H^2\eta\right)_x - U^2 w_{xxzz} - f^2 w_{zz} = 0. \tag{B.15}$$

Finally, we utilize Equation B.8 to express Eq. B.15 solely in terms of η:

$$-U^3\left(\nabla_H^2\eta\right)_{xxx} - UN^2\left(\nabla_H^2\eta\right)_x - U^3\eta_{xxxzz} - f^2 U\eta_{xzz} = 0. \tag{B.16}$$

$$U^2\left(\nabla_H^2\eta\right)_{xx} + N^2\left(\nabla_H^2\eta\right) + U^2\eta_{xxzz} + f^2\eta_{zz} = 0. \tag{B.17}$$

Equation B.17 is a partial differential equation that describes the behavior of the isopycnal displacement.